Subsurface investigation and interaction by self-burying bio-inspired probes

Self-burial strategy and performance in Erodium cicutarium - SeeDriller

Final Report

Authors: Stefano Mancuso[1], Barbara Mazzolai[2], Diego Comparini[1], Liyana Popova[2], Elisa Azzarello[1], Elisa Masi[1], Nadia Bazihizina[1], Edoardo Sinibaldi[2], Camilla Pandolfi[3]
Affiliation: [1]University of Florence, Department of Agrifood Production and Environmental Sciences (DISPAA), LINV; [2]Italian Institute of Technology, Center for Micro-BioRobotics, Pontedera, Italy; [3]ESA Research Fellow.iversity, [2]University, [3]ESA ACT

Date: 12-02-2014

Contacts:

Prof. Stefano Mancuso
Tel: +39 055 4574063
Fax: +39 055 4574017
e-mail: stefano.mancuso@unifi.it

Leopold Summerer (Technical Officer)
Tel: +31(0)715654192
Fax: +31(0)715658018
e-mail: act@esa.int

Ariadna ID: **12-6401**
Ariadna study type: **Standard**
Contract Number: **4000106764/12/NL/KML**

Available on the ACT website
http://www.esa.int/act

SEEDRILLER

Self-burial mechanism of *Erodium cicutarium* and its potential application for subsurface exploration

– FINAL REPORT FOR ARIADNA STUDY 12-6401 -

University of Florence, Department of Agrifood Production and Environmental Science (DISPAA), LINV laboratory

Italian Institute of Technology, Center for Micro-BioRobotics, Pontedera, Italy.

Table of Contents

1 ABSTRACT

Erodium cicutarium plant is a worldwide distributed flowering species with a unique mechanism of seeds dispersion. Seeds can move thanks to its hygroscopically-active tail that allows the seed 'to drill itself' into a crevice. The aim of the experiment described below was to investigate the self-burial performances of the *Erodium cicutarium* seeds in order to evaluate the possibility of a biomimetic transfer of its strategies, focusing on space exploration. In particular, the seeds of this plant are able to improve their chance of penetration in the soil, by exploiting the characteristics of the material of which they are made out. Their particular structure enables the seed to use environmental natural energies as changes in humidity during night-day cycles. This is a good source of inspiration to build device able to minimize power consumption and capable of exploiting *in-situ* resources.

In order to validate the potential arising for future technical applications in unmanned planetary exploration, a first step toward understanding the self-burial performance in *Erodium cicutarium* was undertaken. Self-burial experiments were performed on different types of soils, which were selected for their mechanical properties to be similar to extra-terrestrial soils (Moon and Mars regolith and a very coarse soil to represent an asteroid). Time-lapse images of the seeds were recorded for 24 day/night humidity cycles and additionally landing phases were analysed using high-speed video equipment.

Keywords: *Erodium cicutarium*, self-burial performance, soil exploration, digging strategies, seeds dispersal, plants behaviour, biomimetic.

Objectives

1. Evaluation of the self-burial performances of *Erodium cicutarium* seeds in different types of soil and identification of the contribution of its accessory structures to penetration.
2. Analysis of the dynamic of landing phase to understand its influence in the mechanism of penetration.
3. Modelling of the self-burial strategies and mechanisms.

2. INTRODUCTION

2.1 Biomimetic applications in space-research

Due to their sessile nature, plants have evolved to adapt their development to the surrounding environment in order to optimize their life cycle through sophisticated cost-benefit analyses (Eadie et al. 2011). Organisms that live in challenging, variable and competitive conditions require forms of behaviour that rise to that challenge and must be equally flexible to improve fitness (Baluška et al. 2006).

In the recent years there has been an increased interest towards the study of nature for the construction of bio-inspired structures, and this new area of research is now defined as

“Biomimetic” (Vincent et al. 2006). Plants are a good source of inspiration due to their ability to survive and thrive in hostile or inaccessible environments; they have evolved efficient solutions, through the use of sophisticated physiological and biochemical mechanisms, to deal with challenging and variable surroundings. Furthermore, all these strategies to cope with an ever-changing environment have evolved without a conventional locomotion system and usually with limited resources (e.g. light, nutrients) for plant metabolism. For example, the leaves of the *Lotus* flower are excellent model surfaces that have “self-cleaning” properties. In addition plants can show a broad spectrum of deformation principles that are reversible and depend on the elasticity or viscosity of their structure materials. Indeed, the kinetics behaviour of *Strelitzia Reginae* flowers have been used to create Flectofin®, a flexible material which mimics the valvular pollination mechanism in the bird-of-paradise flower; in this flower, the weight of a pollinating bird or lizard is enough to cause a deformation of the attached lamina that in turn will induce a simultaneous sideways bending by 90° and expose the previously hidden anthers (Lienhard et al. 2011).

Under the constant pressure of variable abiotic and biotic stresses, during the evolution, nature has modified its structures and strategies, in a specific and diversified manner, thus providing us with an inexhaustible source of inspiration. Many inventions drawing their inspiration from plants’ behaviour have presented a scientific high-impact revolution and have helped the creation of a new generation of devices with innovative potential applications, even in the field of space research (Menon et al. 2007). One of the most famous invention which is well suited to these features is that of the hook and loop fastener, i.e., Velcro. This material is generally used by aerospace industry for its technical safety advantages, e.g. to hold objects in place while the space shuttles are in zero-gravity zones. Another example of how plants have been used as model systems is the construction of a robot modelled on the Russian thistle, also called “tumbleweed”; this robot is capable of generating power by using *in situ* resources (e.g. wind), enabling the robot to explore planet surfaces and avoid obstacles (roughness, presence of stones, cracks or soft sand) (Southard 2007). Space exploration requests a very innovative and advanced technology to perform all operation with more accuracy and at lower cost. For this reason this field helps in turn new research activities and supports the creation of new technologies to be used on Earth.

In the future, spacecraft and probes will go farther into space for longer duration of time so a larger autonomy is an attractive feature while searching for deeper mysteries of the universe or evidences of existence of extra-terrestrial life forms (Lee 2000). Therefore the accurate characterization and description of the geophysical properties of extra-terrestrial bodies as planets or asteroids is a priority for future space mission: in this context, the ability to widely distribute several probes at different locations on the planet surface for an extensive ground survey represents one of the major challenge (Sheeres 2003, Blitz et al. 2006, Bombardelli et al. 2007). Space missions possess many constrictions relate to mass and volume mainly associated with the launch phase, and therefore, meanwhile it is important to use material with a good relationship between its mass and its weight, an efficient packaging of the whole construction is also required. These requirements, which are essentially opposites (lightweight materials *vs.* extremely resistant materials and packaging), can be found in plants, where the relationship between fruit mass, dispersal structure size and morphology is carefully defined in respect with the limited resources available and their environment (Pandolfi and Izzo *in press*). The perfect example is that of the *Erodium cicutarium* seed dispersal mechanism, which contains several features that exist simultaneously in a very simple structure that can perform several efforts attractive for future robotic space exploration: the seed is able to launch itself from a stationary position up to one meter, subsequently to move and roll on the surface of the soil and, at the end, it can both penetrate and/or extract itself with the coiling and uncoiling movements of its equipped tail, brushing the soil grains with its hairs.

2.2 Self-burial behaviour of *Erodium cicutarium*

The unique self-burial mechanism of *Erodium cicutarium* is a wonderful example of an efficient and brilliant strategy used by plants to disperse their seeds. In *Erodium*, seeds are propelled into the ground by exploiting the natural source of energy derived from the

Fig.1 *Erodium cicutarium* plant. From the left side, stems with leaves, flower and

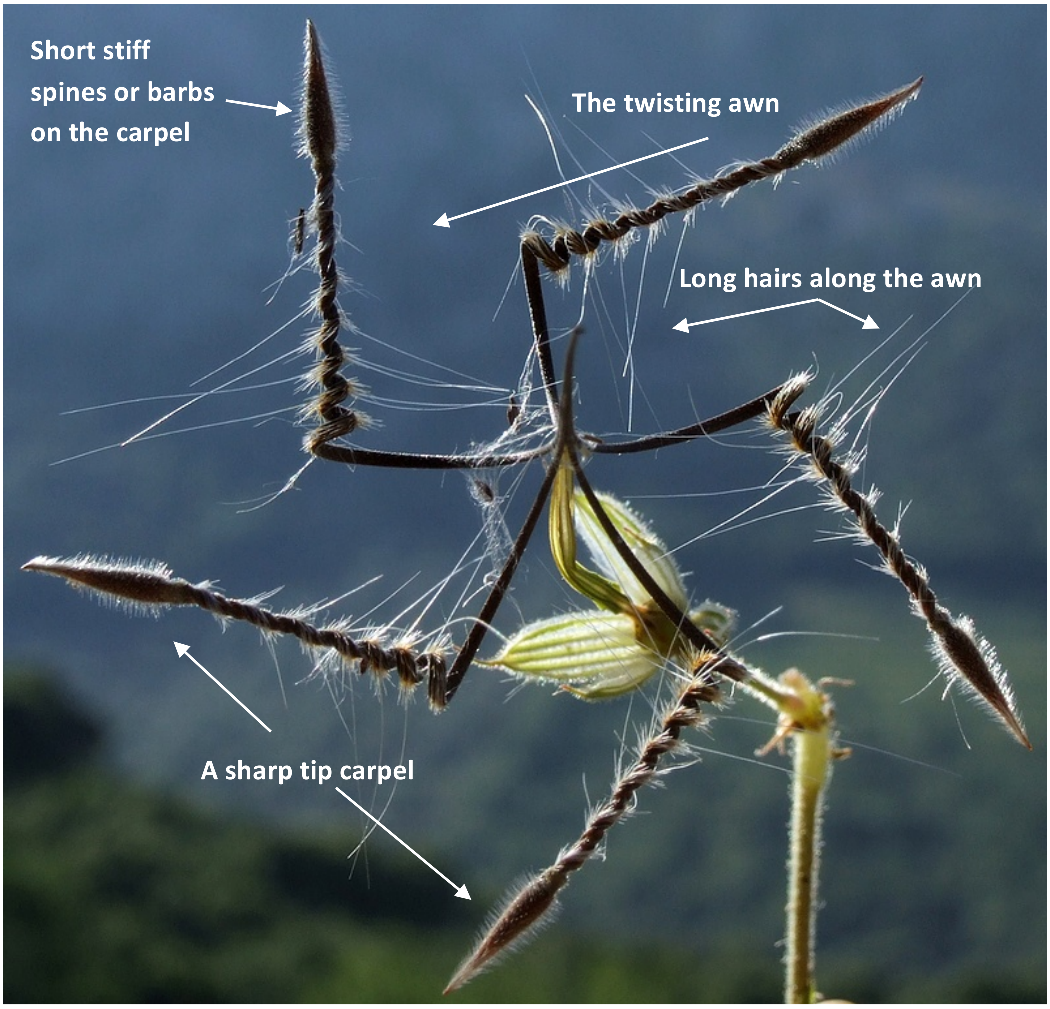

Fig. 2 The five seeds attached at the base of the flower and their structure

day/night humidity-cycles. A similar mechanism based on a humidity-driven movement is seen in the wild wheat plant (*Triticum turgidum ssp. diccocoides*) and its awns; nevertheless the friction forces and the structures used by the two species are different, confirming the well-known statement that the natural selection can find different solutions to solve similar problems. The worldwide and abundant presence of *Erodium* clearly underlines the importance of its simple but effective mechanism to penetrate soil (Mensing 1998). These features can well suit and support the main aim of the study: the development of a novel approach for digging systems to be used for under-ground planetary exploration, focused on the idea of minimal power.

Erodium cicutarium (Fig. 1) is a winter herbaceous plants, annual or biennial, belonging to the family of *Geraniaceae* and is considered as a flowering weed. It is characterized by a high capacity for adapting itself to different conditions, and can therefore be found worldwide (Europe, Asia, Africa, and North and South America). The optimum growth temperature for *Erodium* plant occurs at 15-25 °C but it can be found in arid and semi-arid areas and it grows successfully in calcareous, sandy, loamy and in mechanically decomposed granite soils. The seeds germinate in soil with temperatures between 21°C during the day to 4°C at night (Mensing 1998). *Erodium* plants produce several stems, usually, red in colour, haired and branched. They grow along the ground and can ascend with stalks 10-50 cm long. The structure of the inflorescence is composed of groups of flowers, generally from two to eight, gathered in clusters. Every individual flower consists of five, pink to purple, petals and five sepals. The sepals of the flowers are somewhat pointed and hairy. The fruits of *Erodium* have the form of a bird's beak and sizes that vary from two to five centimetres. The developing fruit splits into five segments, each with an elongated, spirally twisting style with a seed attached at the base. The awn twists hygroscopically and shoots the seed into the soil. *Erodium cicutarium* seeds (Fig. 2) possess a typical wedge-shaped hairy carpel with barbs similar to stiff spines. The awn has white long hairs along the longitudinal axes and ends with a hygroscopically active tail sensitive to humidity and able to twist. A single mother plant can shoot its seeds up to 0,5 m from the fruits through an explosive dispersal system. Furthermore, the seeds are endowed of additional movements derived from their hygroscopically-active tail and can also be dispersed by animals, birds and insects. The tail responds to the natural wet-dry cycle occurring during day and night by reversibly uncoiling when wet and recoiling when dry (Fig. 3); this surprising structure makes the seeds able to move by decreasing and increasing tension and drills itself into the soil. The self-planting system needs soil surface irregularities for self-burial: the seeds roll on the soil and establish themselves in fissures and crevices of the soil whilst the barbs on the carpels act as anchorage allowing the seed ‘to drill itself’ into the ground (Stamp 1984).

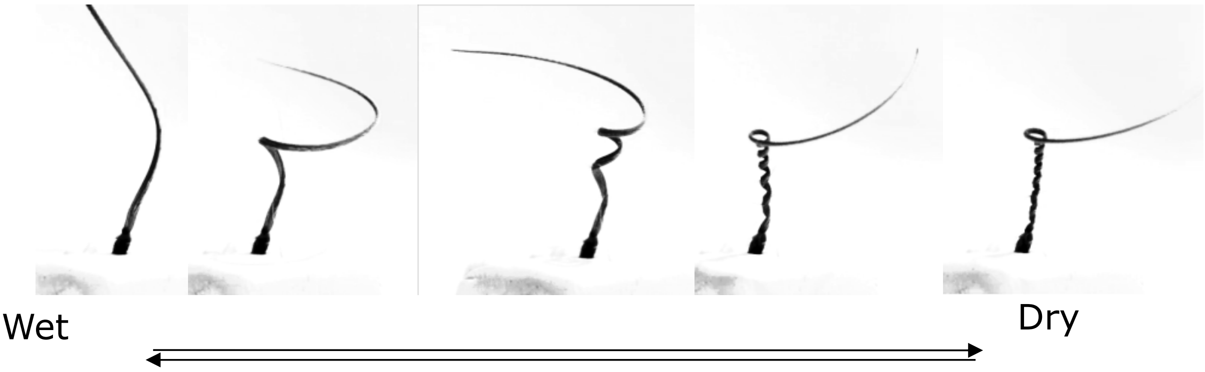

Fig. 3 The seed configuration results in a coiling and uncoiling motor: the awn is linear when wet and it turn into helical when dry.

2.2.1 *Erodium cicutarium* self-burial performance analysis in the past

Most of the recent studies on *Erodium cicutarium* seeds have focused on its structure and the main study on the seed self-burial performances was conducted by Stamp in the '80s (Stamp 1984). He evaluated the functionality of these seeds in several substrates and applied several modifications to their structure. From the work conducted by Stamp it emerges that:

- Seeds cannot bury themselves in a soil without any crevices. It was found that when there were depressions, the shape and the size of the fissure influenced seeds behaviour as seeds tended to move. For this reason the uncoiling-coiling process is referred to as a secondary dispersal mechanism, which can increase the probability of penetration in the soil and increase the depth reached by the carpel.
- The carpel may play a key role in the anchorage phase of the burial. In all soils, carpels without barb (i.e., barbless seeds) presented the worse success rate both during the drill action than in depth, with the exception of very coarse grains where a seed can logically falls and stays in a crevices. These results would support the hypothesis that hairy-carpels are required for a steady anchorage.
- The importance of all the accessory structures would seems to be related to the depth of penetration and the ability to keep the seeds in the crevices, rather than being related to the ability to penetrate.
- The stiff spines are helpful to maintain a certain angle but this angle is also maintained by the tail leverage, so their function is not completely clear.

Although the study conducted by Stamp (1984) address several question regarding the seed burial mechanism in *Erodium* the functionality and the contribution of each single structure still remains unclear. We therefore decided to monitor and observe the movement through a time-lapse project to be able to better understand the seed behaviour and functionality.

2.3 Extra-terrestrial soils

Several planets and asteroids or satellites of our solar system possess a cover of dispersed and granular material called regolith (from Greek rhegos, "blanket", and lithos, "rock"). Despite it is incorrect to refer to extra-terrestrial terrain as "soil" because it is a pedo-genetic term used only for Earth that includes the alterations produced by biological activity, it is very common to mention Martian or Lunar soil and this term is widely used. The study of extra-terrestrial regolith and dust, which cover the surface of planets and asteroids, has been deeply investigated in the past. The requisite to understand soil composition, in order to permit an optimal functionality of landers and probes which usually need to act on the surface (i.e. drilling, sampling or landing), is tightly linked with the very limited possibility of directly using extra-terrestrial soil sampled during past missions. The impossibility to use test materials from planets therefore has forced people to use different components to mimic their key features. In this case soil simulants (i.e. any material, both synthetic and/or natural whose purpose is to imitate the chemical/physical

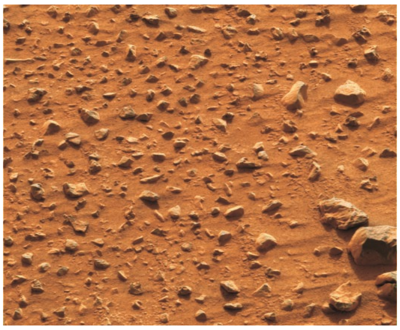

Fig. 4 A Pancam color image of soil in Gusev crater of Mars, showing regularly spaced clasts and

properties of the extra-terrestrial soil such as dusts, rocks, regoliths) can be used.

Mars

Mars exploration can be expected to be the best candidate application for such probe, thanks to its abundant desertic soils, which are quite similar to those where *Erodium cicutarium* seeds are naturally found. Moreover, if compared to the Moon or asteroids, this planet has less extreme constraints (i.e. the temperature, gravity level or atmospheric pressure). Martian regoliths are composed of a complex and heterogeneous mixture. The entire surface is characterized by volcanic rocks of basaltic composition partly pulverized by impacts and by sedimentary rocks of possible marine origin formed by silicate and rich of sulphate (Knauth et al. 2005). Similar gravels to these dusted stones can be found at the confines of the sunny districts in Arabia and Tharsis (Murchie et al. 2000). In this rocky substrate a layer of fine and grainy powder that accumulates or forms a crust covers most part of the surface (Binder et al. 1977, Janice et al. 2002). A great difference in temperature between its two hemispheres induces strong winds, up to 400 km/hour, and therefore soil is transported from one place to another as powders. Thus, the composition of most of solid materials on the rock and in space between rocks is formed by all particles transported in the atmosphere and released on the ground as showed in fig. 5. The surface has been deeply analysed in several mission from different probe (e.g., Viking Lander and Mars Pathfinder) and we know the surface possess 5% of rock of about 1cm. Numerous areas are covered by fragments of a dimension that reach 10 cm, up to 50% compared with the total rock-covered area and powder (Fig. 4 and Fig. 5).

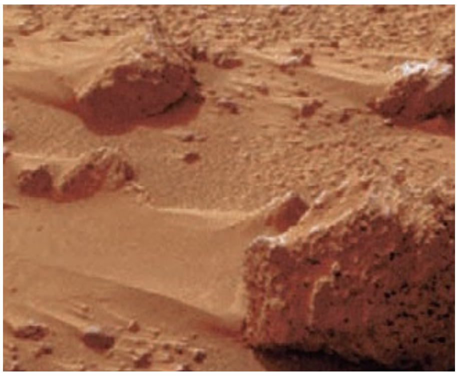

Fig. 5 Images of Mars soil powder cemented near the Pathfinder lander site (Janice

Moon

Moon soil is composed mainly of regoliths (Fig. 6). Space missions focused mainly on craters as they are more favourable and safer landing places, and thus the majority of the samples we currently have come from lunar mare sites. The surface of the planet is covered of a sandy heterogeneous layer that can be from 4 to 15 m-thick. Going below this layer, there is a region formed of "megaregolith" composed of plaques or fractured bedrock created by large impacts. The fact that there are several craters, and thus many interesting places where to perform soil exploration, on the Moon has been known for a long time (e.g. the Shackleton crater which hypothetically is one of the most promising site for the first moon base). Unfortunately, on the Moon the gravity is negligible and this be a problem, in particular on anchorage phase of a drilling

Fig. 6 Example of lunar regolith composed of fractured rock material ok parts with a size <1cm to 2-4 mm size. (photo by Randy Korotev,

probe. In addition, temperature is hostile and rarely exceeds −173 °C. Lunar soil can be used as synonym of Lunar regoliths for their abundance and usually refers to the finer fraction of the soil. This fraction is composed of grains of about 1 cm in diameter or less. Finer grains are indicated as "Lunar dust" and can reach the diameter of less than 100 micrometres that give them an efficient consistency. This fine grain powder has mainly been molded by continuous impacts by meteoritic bombardment.

Asteroids

On asteroids the atmosphere is absent and there are great temperature differences, which vary with the distance from the Sun. However, the surface temperature can vary significantly depending on the side exposed to solar radiation and that in the shadow during the rotation. Finally, asteroids also have regoliths mainly derived from meteoroid impacts. The soil properties are generally unknown, and can vary greatly among different asteroids. The surface is covered by dust and generally its shape is very irregular. Recent studies suggest that the composition of many asteroids can be different: some can have a composition very similar to their analogue meteorites, with high bulk density and limited porosity, meanwhile other asteroids can present a very significant porosity produced by a fractured surface (Britt et al. 2003). This mainly depends on the violent collisional history of each asteroid that strongly influences its surface composition, which can in some instances become a “rubble pile”. Chapman (1978) first describe the “rubble pile” as a weak aggregate of inhomogeneous particles held together by gravitational bounds rather than material strength that is formed as a result of high speed collisions; these collisions cause extensive fracturing and destruction, resulting into a “rubble”.

3. Evaluation of the self-burial performances in different types of soil

The aim of this part was to investigate the self-burial performance focusing on different soil mixes, to understand how the physical properties of the soil can influence the penetration. The work conducted by Stamp (1984) has highlighted the importance of particle size: in particular, the soils tested were characterized by big particles, ranging from sand (grain size < 1 mm^3) to coarse gravel (47 mm^3), and a particle diameter ranging between 1.2 and 5.5 mm. Given potential extra-terrestrial applications of biomimetic self-burial devices, we wanted to expand the knowledge of the seed performance for a wider range of grain sizes, focusing in particular on different soil mixes, with finer particles mixed with bigger rocks (resembling extra-terrestrial soil in term of particle distribution of dimensions).

Several experiments were conducted to mimic different extra-terrestrial soils or to explore similar substrate compositions, in order to understand the possible use of this kind of penetration. Four soil mixtures were tested (Mars, Moon and Asteroids), as they are the best candidates for such inspired probe. Another soil mix called “Test soil” was used to calibrate and test the set-up and to understand the influence of the finer particles in the penetration mechanism.

3.1 Soils material

All material used for this project have been chosen not only for their physical characteristics but also to reflect other advantages on the basis of the techniques used for the analyses. All estimation of penetration was performed by image analysis; for this reason we had to consider the problem of the contrast between the seed and the background colour of the soil. Therefore mainly white materials were used to highlight seed movement; in particular talcum was always employed instead of silt and clay. Talcum is a non-toxic material with very small particles which is able to cover all external part of the other rocks, resulting in a clear background. Second, to better connect the aim of this work with potential applications in the future and to understand how to scale-up this device, very light materials were used to focus more on the dynamic property of the penetration as the seed weight is very limited. This choice was also done because the gravity pull on other planets is lower than on Earth, and this can modulate particles adhesion and forces. As consequence the bulk density of the soil simulants used for this work usually resulted lower than the ones commonly calculated; the soil mix are therefore not going to be a perfect simulation of extra-terrestrial soils but a simplified and flexible version of them based on the experimental requirements. In addition, we knew from the literature that crevices or holes are determinant to start the self-burial process, thus big particles were added to the mix in order to mimic the presence of big rocks on the surface.

The soil mixtures employed in this study, were assembled from the following pure materials: expanded clay, perlite, pumice, sand and talcum. A brief characterization of particle size and shape is given in Tab.1, and the measured physical properties are given in section 3.1.1.

Tab.1 Particle size and shape

Expanded clay

All particles of expanded clay used to mimic the soil, as representatives of bulky boulders had a volume in the range of 0.8 cm to 1.8 cm. The majority of the granules had a rounded shape. The surface presented a roughness with sporadic crevices in the rock.

Pumice

All particles of pumice presented irregular shape with a good variability in size from 0.1 cm to 1.2 cm. A good amount of fine particles was presented in the residual with a dimension sometimes lower than 5 µm as shown below.

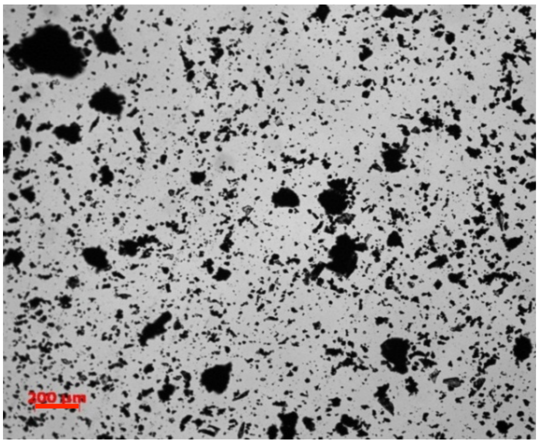

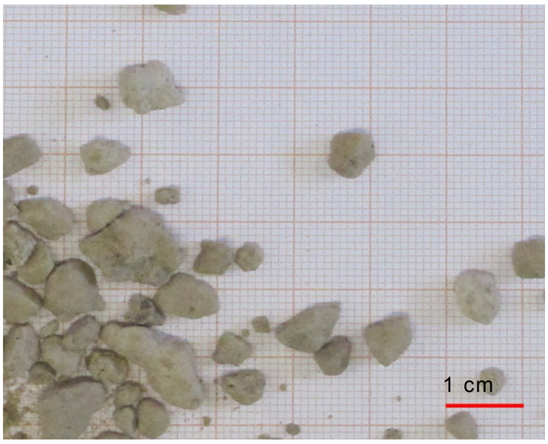

Sand

Sand used in this work presented regular round particles of about 0.5-1 mm of coarse grains and very limited residual.

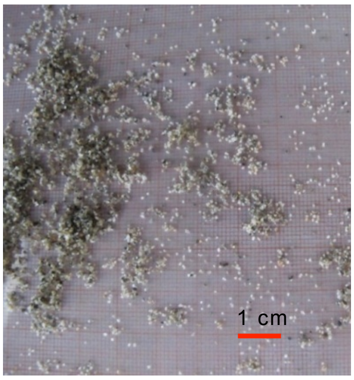

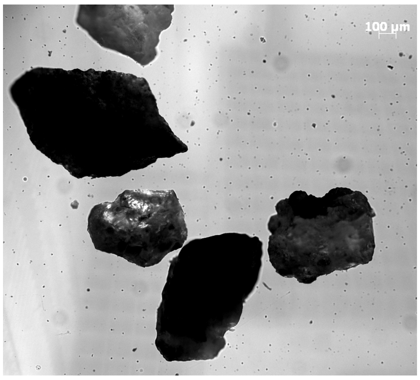

Perlite

All particles of perlite presented a shape similar to the pumice with dimension from 0.2 cm to 0.8 cm. The residual was rich of very small powder of few µm.

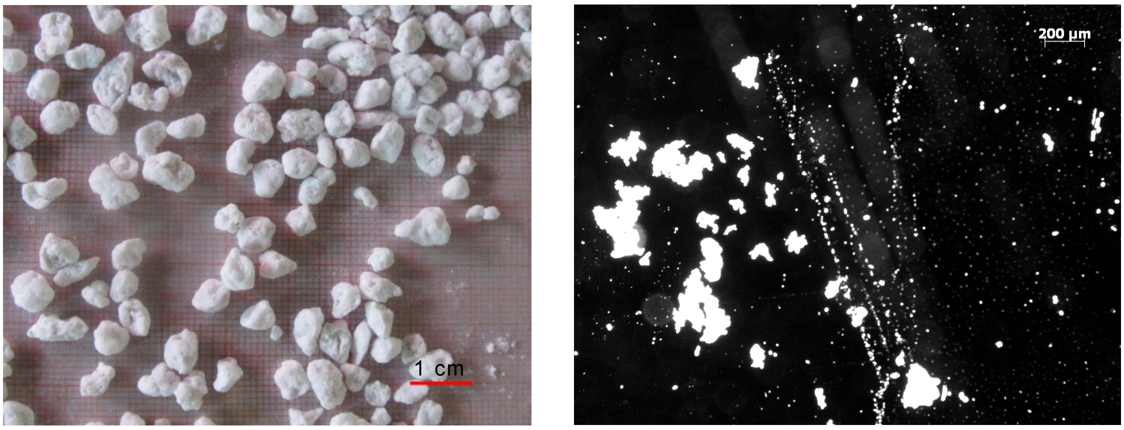

Talcum

All particles of talcum were less than 50 µm.

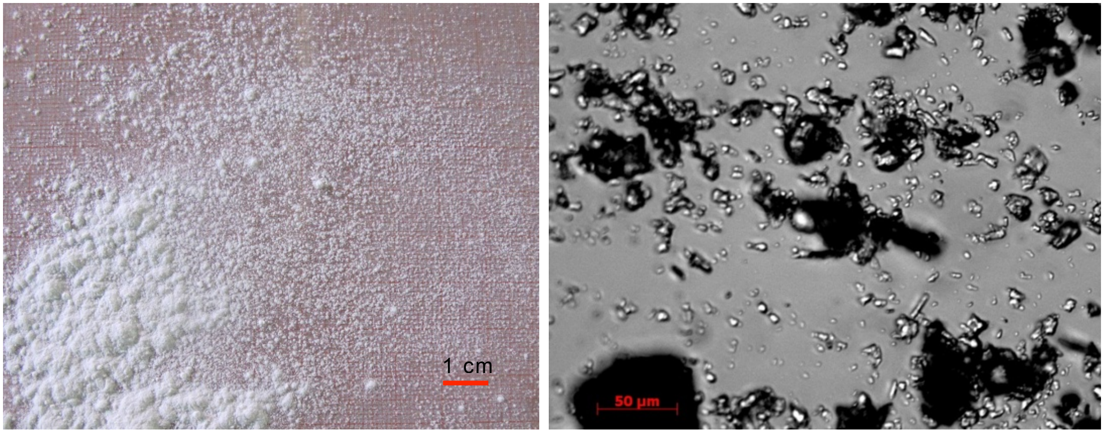

3.1.1 Soil mixtures

The composition of the four soil mixes (Fig. 7) is given in Tab. 2.

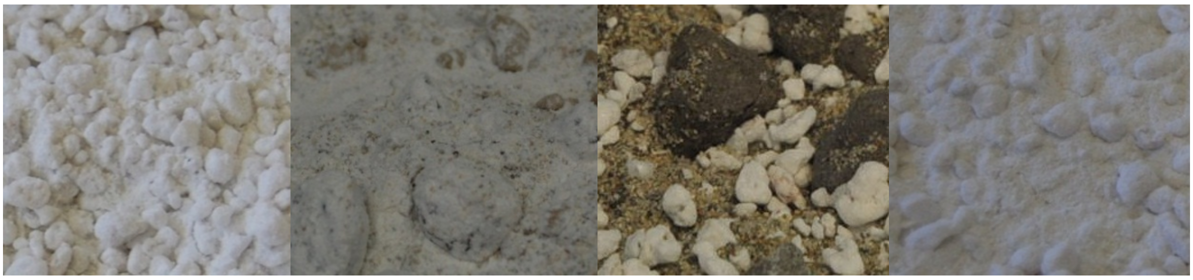

Fig. 7 Overview of all the soils used to test the self-burial performance of *Erodium Cicutarium* seeds. From the left to the right: Moon, Mars, Asteroid and Test soil.

Tab. 2 Composition of the soil mixtures used in the experiments

	Exp. Clay 0.8-1.8 cm	Pumice 0.1-1.2 cm	Perlite 0.8 cm	Sand 0.5-1 mm	Talcum <50 µ
Moon	-	-	66%	-	33%
Mars	20%	20%	20%	20%	40%
Asteroid	33%	-	33%	33%	-
Test soil	-	-	50%	-	50%

Moon

For the composition of the moon we used a dusty soil in order to understand the contribution of very small particles in the performance. As shown in Fig. 8 Lunar soil is composed by powdered particles. We therefore used:

- 2/3 part as the portion of the regolith: size <10 mm (medium size grain 2-4 mm).
- 1/3 part as the portion of lunar dust: a mixture of silt and clay.

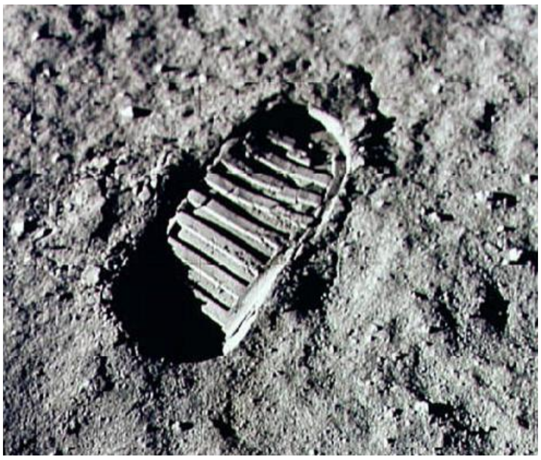

Fig. 8 Footprint of Neil A. Armstrong on July 20, 1969. This image shows the powdery nature of lunar surface (NASA).

Mars

As show in Fig. 9 several simulants have been proposed to recreate the desert soil of Mars. These simulants are artificial desert soil with at least 30% of silt and 20% of fine sand, whilst the rest is medium or larger size sand and coarse. We used:

- 1 part of sand, 2 part of silt, 1 part of clay (to mimic desert soil),
- 1 part rock from 1 to 5 cm (to mimic rocks on surface).

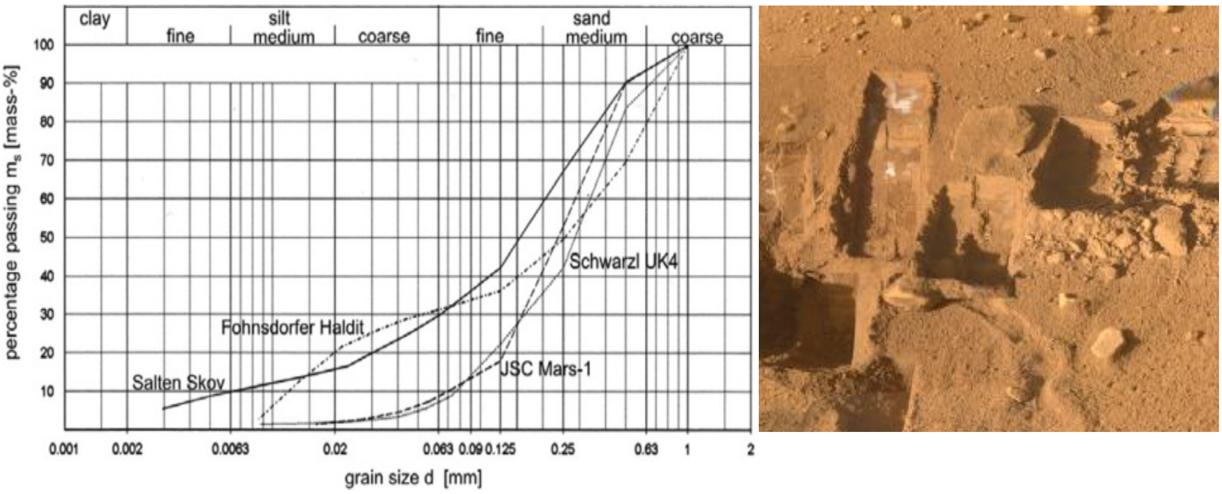

Fig. 9 LEFT: examples of particles size composition of four common analogue of Martian soil (Seiferlin et al. 2008). RIGHT: example of mars soil profile (Certini 2010, picture of NASA/JPL).

Asteroids
To mimic primitive asteroids, which are fundamentally weak and more probable to be loosely agglomerated, with a big fractured part on surface as rubble piles. This choice has been forced to try to explore the behaviour of a seed in a soil with coarse gravel with features opposite to others simulant as show in Fig. 10. We used:

- 1 part sand, 1 part grain size of about 5-10 mm, 1 part big grain size of about 10-30 mm

Test Soil
A test soil was used to perform few preliminary tests on the set-up, i.e. time of cycle of wet and dry condition. A test soil similar to our simulant called Moon was employed to understand if the fraction of small particles could affect the dynamic of penetration. We used:

Composition: 1 part perlite, 1 part talcum.

This simulant was assembled also to study soils with different features and to cover different position in the texture triangle; this enabled us to monitor the seed behaviour in different and contrasting soil composition. The only exception was that the Test soil was deliberately mixed with characteristics similar to those of the Moon simulant. The composition of the gravel and the position of each soil are shown below in Fig. 10.

3.1.2 Physical and mechanical properties of the soils

Granulometric Composition

The granulometric composition of each soil used in this study has been referred to soil texture diagram as shown in Fig. 10. It is important to notice that the triangular diagram takes into account only the portion of the soil with grain size < 2 mm, all the rest is referred as gravel. The terms sand, silt, and clay refer to relative sizes of the soil particles: Sand, particles between 0.07; Silt, 0.07 to 0.005; Clay, being particles below 0.005 mm.

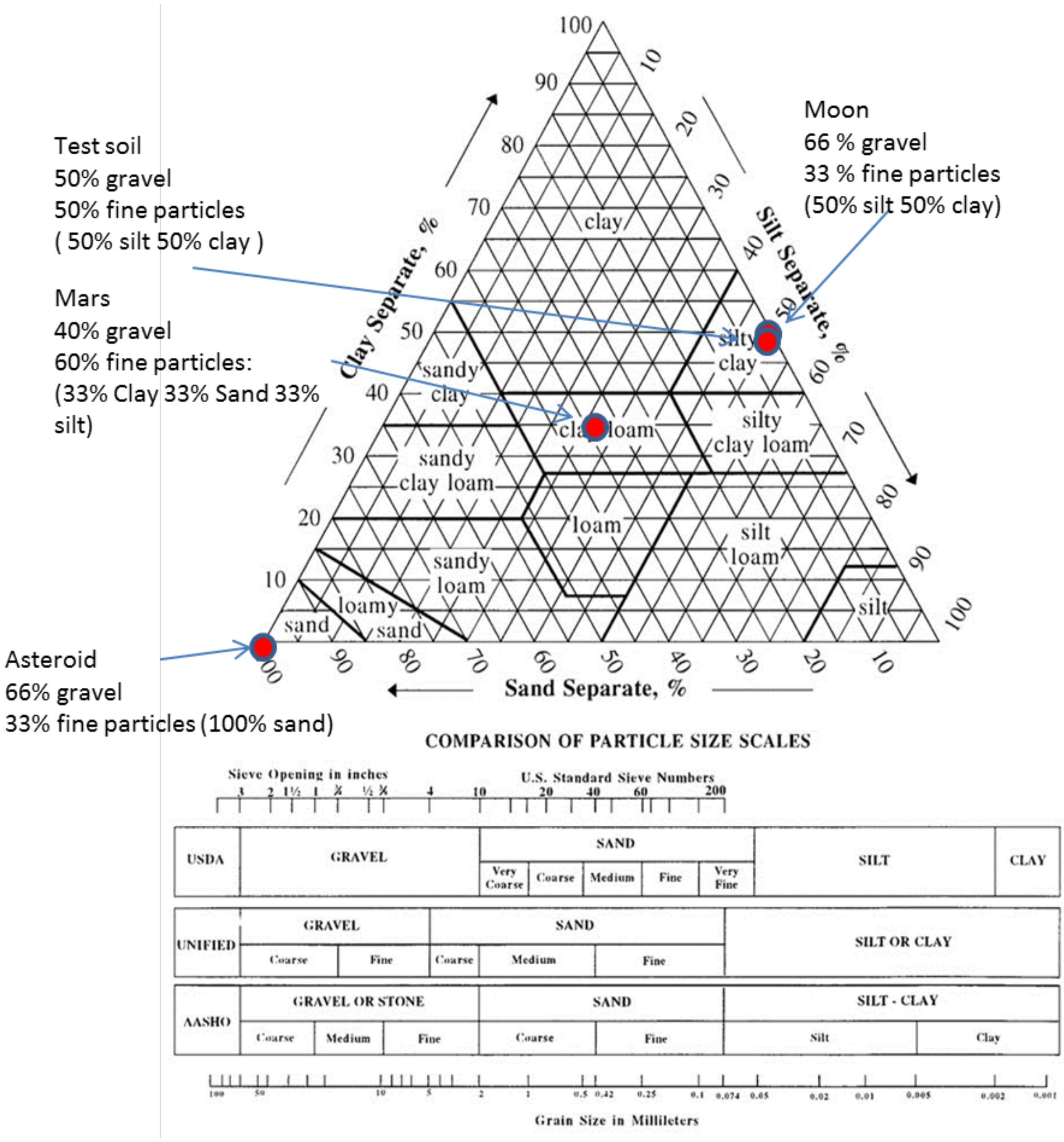

Test soil
50% gravel
50% fine particles
(50% silt 50% clay)

Mars
40% gravel
60% fine particles:
(33% Clay 33% Sand 33% silt)

Moon
66 % gravel
33 % fine particles
(50% silt 50% clay)

Asteroid
66% gravel
33% fine particles (100% sand)

Fig. 10 All simulants compositions are resumed in this scheme.

Bulk density, porosity and particle density

Bulk density is a property of a soil mixture and/or a material which possess a mass as powder or granules. For this reason it depends on soil texture and on its packing organization. Bulk density is an indicator of soil compaction, expressed as the ratio of the dry weight of a material and its volume, comprehensive of the empty space of pores among soil particles. In general a loose and porous soil possesses a lower bulk density. On the other hand, high bulk density usually indicates low soil porosity and is linked with high soil compaction. Soils with a big amount of sand have relatively high bulk density because the inter-particulate empty volume is less compared to silt or clay. Soils rich in silt and clay, with a smaller particles size composition, have higher void volume and a lower value of bulk density.

The bulk density is expressed as:

$$Bulk\ density = \frac{mass\ of\ the\ soil}{Total\ volume\ of\ the\ soil}$$

It is commonly presented as g ml^{-1} but also as kg m^{-3} or g cm^{-3}.

The bulking property of a powder is not an intrinsic property of a material but it depends on particle size and composition. The bulk density is typically described in two methods: freely settled, obtained simply adding a quantity of soil in a specific container; tapped, referred to a powder inserted in a container "tapped" by a mechanical compaction process.

In this study, for all soils, bulk density was measured in 100 mL or 200 mL containers, which were soft tapped, by repetitively beating each vessel for 30 seconds on a bench to generate vibrational forces.

The **porosity** of a soil or sediment is defined as the fraction of the volume that is not occupied by solid material. In particular it defines empty spaces among all particles of a mixture.

$$Porosity = \frac{Volume\ of\ void\ spaces}{Total\ volume\ of\ the\ soil}$$

This property is expressed either as a fraction with values between 0 and 1 or as a percentage. Porosity range is not linked with pore sizes and distribution or connections. For this reason also soils with similar value of porosity may possess different physical characteristics.
In sedimentary soils the porosity depends mainly on grain dimensions, shape and the degree of arrangement and cementation. In stones, the porosity depends upon the amount, configuration and positioning of fissures and crevices. Mixtures of particles of similar size usually have lower porosity than distributed sized organized materials because all void spaces between larger grains are occupied by small elements.

In this study total pore volume of each soil was calculated. All materials were weighed in a container with a known volume after being saturated with water. They were then maintained for three days at 50° C to dry and reweighted.

Particles density can be defined as the mass of all particles on the volume occupied by the soil without considered the empty spaces (soil particles volume):

$$Particles\ density = \frac{Mass}{Soil\ particle\ volume}$$

In Tab. 3 the values of these three parameters are reported.

Pure soils

Sand had the higher bulk density value, showing a high level of compaction and a high particle density followed by talcum and pumice. On the other hand perlite and expanded clay are lighter materials with a lower value of bulk density and particles density. Porosity was found to be higher than 60% in talcum and perlite, 58% for pumice and about 45% for sand and expanded clay.

Bulk density: Sand > Talcum > Pumice > Expanded clay > Perlite
Porosity: Perlite > Talcum > Pumice > Sand = Expanded clay
Particle density: Talcum > Sand > Pumice > Expanded clay > Perlite

Soil mixtures

Mars and Asteroid presented the higher level of bulk density, for this reason the soil was very compact and the level of porosity was lower than in the other soils. This feature was associated to the presence of sand, which intercalates in the empty space to limit porosity of each soil. For this reason Asteroid did not have the level of porosity expected, as it was assembled only with large particles. Moon and Test soils were similar as planned, with a difference in the bulk value due to the greater presence of talcum.

Porosity: Moon > Test > Mars > Asteroid
Bulk density: Mars > Asteroid > Test > Moon
Particle density: Mars > Asteroid > Test > Moon
Percent of Gravel: Moon = Asteroid > Test > Mars

Tab. 3 Bulk value, Porosity and Particles density calculated for each substrate.

	Bulk density	Porosity	Particles density
Mars	0.98	0.44	1.78
Moon	0.38	0.53	0.76
Test	0.48	0.5	0.97
Asteroid	0.81	0.37	1.29
Pumice	0.57	0.58	1.33
Talcum	0.71	0.62	1.87
Sand	1.34	0.46	2.51
Perlite	0.11	0.65	0.31
Expanded Clay	0.37	0.46	0.70

Angle of repose

The angle of repose or "critical angle" is the minimum angle (or a maximum slope) where grains maintain a pile due to the forces of gravity and the effect of friction among all particles. It is usually defined empirically by pouring a granular material on a surface and measuring the angle of the resultant conical pile. It is the sharpest angle of decay or the inclination of the slope between the surface of the heap and the horizontal level. This angle is always more than 0° and less of 90° and is usually in the range of 30-45°.

This property is linked to particles density, surface area and shapes and it depends on the coefficient of friction of the material. Irregular granules or elements with a strong grip power have a tendency to produce piles with steeper sides and a higher angle of repose.
There are several methods used to measure this property and in this study we used the "Fixed Funnel Method": it consists in the insertion of all material through a funnel to create a conic heap as show in Fig. 11. Gradually when the pile of material grows, the outlet funnel is moved upwards very slowly without interfering with the formation of the heap and in the same time reducing the effect of falling particles. A picture from the side of the cone has been taken with the camera objective disposed not too close to the pile to avoid perspective mistakes.

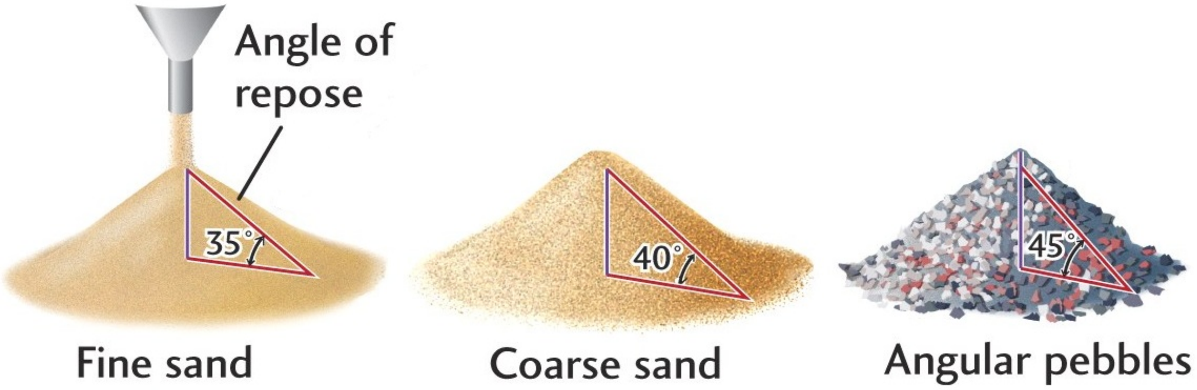

Fig. 11 Images of the angle of response of three different soils

Critical angle was measured for all materials used in this study once piled (Fig. 12). In Tab. 4 all values calculated on three different replicates are shown.

Tab. 4 Angle of repose of all materials used (SD derived from three repetitions).

	Angle of repose	SD
Asteroid	33.02	0.52
Mars	38.95	0.67
Moon	40.99	0.93
Test	40.69	0.82
Perlite	38.78	2.05
Pumice	33.74	1.06
Sand	35.51	1.43
Talcum	60.81	1.34
Expanded Clay	26.11	0.89

Pure soil

Pure material showed a variable angle of repose (Fig. 13). The highest value was found in the talcum which permitted a maximum angle of 60° due to the grip among the small particles of the material. Perlite had an angle of approximately 38° followed by sand and pumice respectively at 35° and 34°. Expanded clay, due to the round and big size of its particles, showed a very low value of angle of repose.

Angle of repose: Talcum > Perlite > Sand > Pumice >> Expanded clay

Simulant

The angle of repose of the simulants had similar values to the pure material and a lower standard deviation due to the ability of soil to form more regular pile. Asteroid presented the lower value of about 33° for the contribution of the expanded clay and the sand whilst Moon and Test had a similar angle of about 40° and a value in a range of 3 degrees of difference with Mars whom was a bit lower at about 39°.

Angle of repose: Moon > Test > Mars > Asteroid

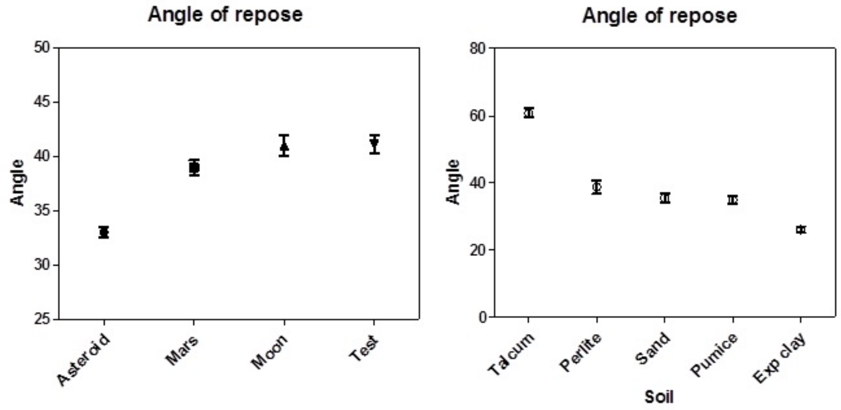

Fig. 12 Angle of repose showed in graph for each mater

Fig. 13 Pictures of pile derived from the four soils. From left, respectively, Moon, Mars, Asteroid and Test soil.

3.2 Experimental setup

Two chambers were assembled for the analysis of penetration performance. In each chamber there was a container with the soil and several seeds (Fig. 14). Using two cameras connected

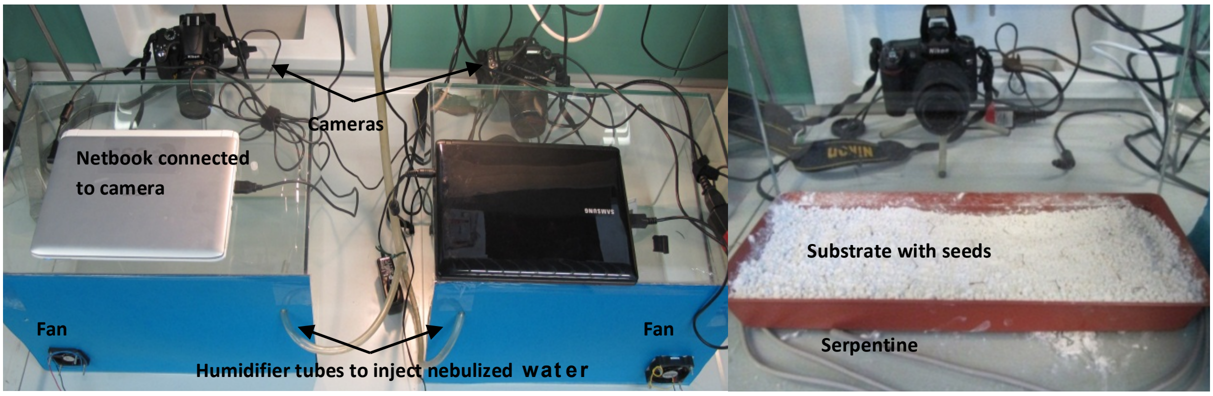

Fig. 14 Pictures of the experimental set-up

to a notebook a sequence of image was collected as shown in Fig. 15. All stored images were used to create a time-lapse video for each experiment and for accurate analysis of the movements. Several wet-dry cycles were used to mimic day and night humidity changes, and the image capturing started whilst dry and wet cycles alternate for several hours. Images were collected with a frequency of one picture every ten seconds.

About 20-25 seeds were used for each experiment for at least four days (20-24 cycles); as we collected a high number of images, the analysis of the data allowed us to investigate in details all movements made by the seeds.

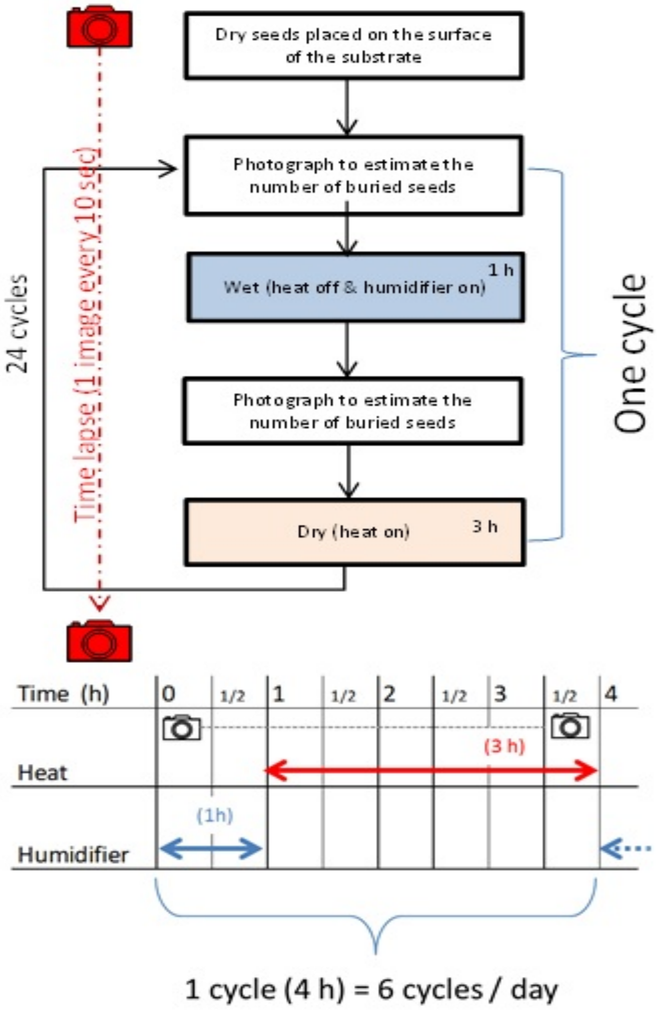

Fig. 15 Scheme of the set-up with the duration and a brief description of each operation performed during all stages.

WET CYCLE

During the wet cycle a humidifier was turned on, and a relative humidity of about 100% was reached in a few minutes. The humid cycle was maintained for 1 hour to allow a complete uncoiling of the seeds.

DRY CYCLE

During the dry cycle a serpentine and a fan were activated in order to dry quickly the soil and the air. The dry climate was kept for 3 hours to dry the soil and allow a complete coiling of the seeds.
An exception was made for the Asteroid mix, where the dry-cycle lasted approximately two hours due to the ability of the soil to dry more rapidly.

3.3 Results

3.3.1 Establishment of the seeds into the soil

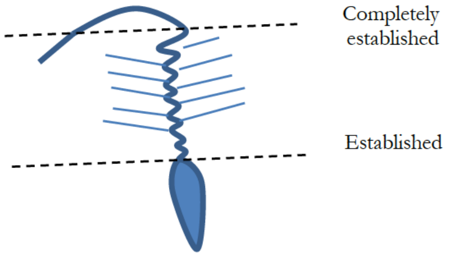

Fig. 16 Seed establishment conditions respect the ground

The establishment of the seed in the soil has been calculated after 24 cycles for about 40 seeds for each soil. Two conditions were considered to discriminate the successful strategy of burial and are illustrated in Fig. 16. The seed was considered "established" when only the carpel (the head of the seed) was underground. When a seed continued to penetrate into the soil until only the tail was visible, it was considered as "fully established". The percentage of established seeds in all different soils is shown in Tab. 5. The percentage of established seeds in the different soils was very similar, varying between 82 and 87%. However, the ability to penetrate deeper into the soil varied among the four soils. More than 67% of the seeds in Asteroid soil were fully established. However, the number of seeds that penetrate deeper into the soil decreased substantially in the remaining soils, with only 36%, 11% and 3% of seeds fully established in Mars, Moon and in Test soil respectively.

Tab. 5. Percent of seeds buried during all experiments.

	Tot	Established	Fully established	% Established	% Fully established
Asteroid	46	38	31	82.6	67.4
Test Soil	41	34	3	82.9	7.3
Moon	46	40	5	86.9	10.8
Mars	39	32	14	82.05	35.9

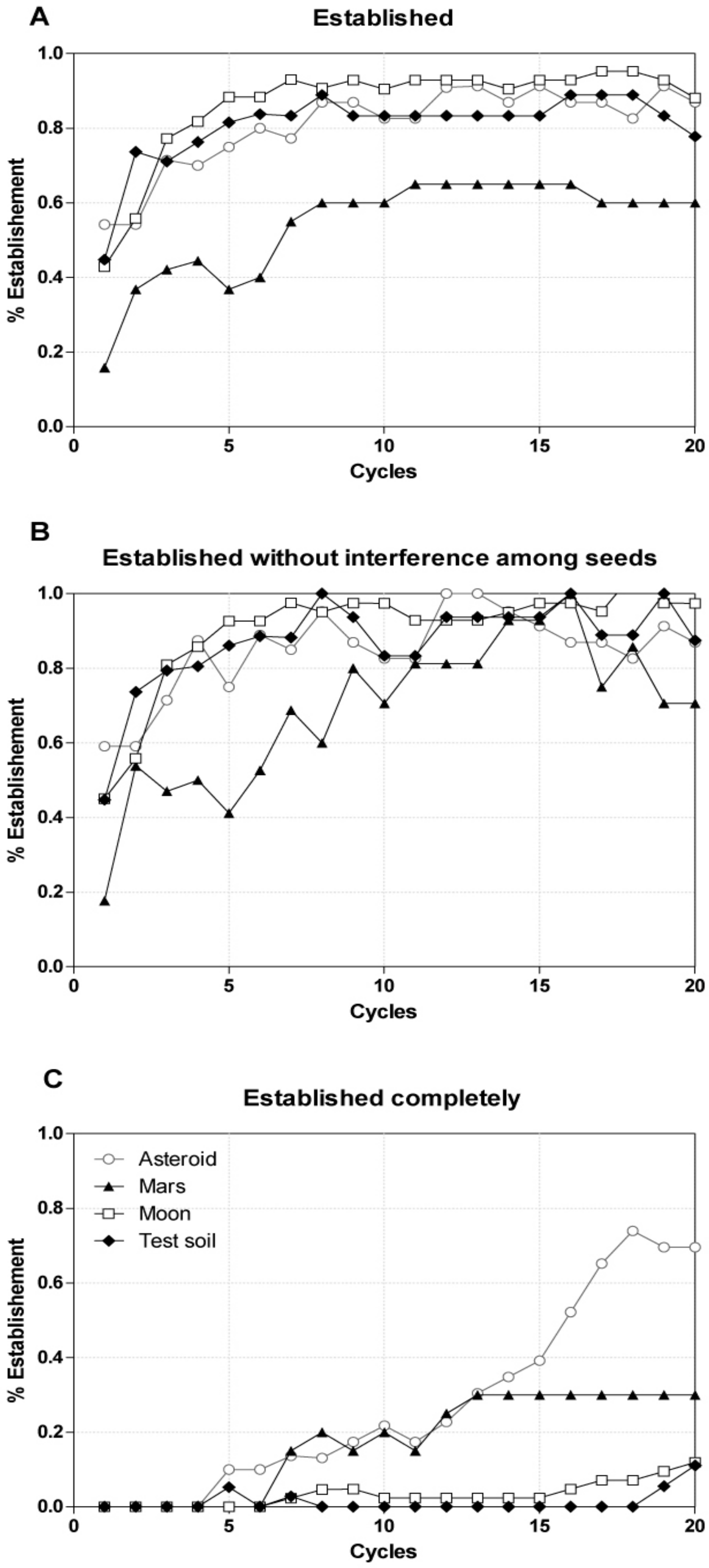

Fig. 17 The three graphs show the incremental number of buried seeds. A: number of buried seeds has been counted after every cycle without any interference consideration. B: number of buried seeds

In Fig. 17 the incremental number of seeds buried during the cycles is reported. The number increases drastically during the first 2-3 cycles, where more than 50% of the seeds established into the soil. The subsequent drop in the numbers indicates that sometimes the coiling-uncoiling motion can have a negative effect on the performance, in some other cases the neighbouring seeds can interferes each other, resulting in the extraction of some seeds from their borrow. For this reason two different graphs have been plotted. Fig. 17a has the full set of data, whereas interfering seeds were removed from the total count in Fig. 17b. Fig. 17c shows the trend of the fully established seeds.

All soils except Mars showed a similar trend of establishment, whereas Mars had the lower initial increase. The high rate of interaction registered in Mars could be associated to a higher mobility of the seeds in the soil and to a lower amount of crevices or obstacles where the seeds could start the drilling (due to the high bulk density and porosity of the Mars mixture). Indeed, as the spacing of the seeds at the beginning of each experiment was kept constant, the higher level of interference can only be justified by a higher mobility. If some seeds were too close, they started to interfere with each other, which prevented the penetration. The image analysis revealed that, in some cases, the seeds could cover more than 10 cm, and therefore we could not always totally prevent interferences. All interferences had a negative effect on the penetration of the seeds, causing the extraction of one or both seeds involved in the contact.

In regards to the fully established seeds, the cycle-by-cycle count revealed a high rate of establishment in the Asteroid mix. After only 5 cycles some seeds were completely buried into the soil. On the other hand, in Test and Moon mixes, the number of fully established seeds remained very low, probably due to the high amount of fine particles that filled the empty spaces of the soil. In the Asteroid and Mars mixes the number of completely established seeds increased from the 5th to the 15th cycle. However, from the 15th cycle onward, meanwhile in Mars there was no increment, a large amount of seeds started to penetrate in the asteroid soil.

3.3.2 Cycle length and condition at the beginning (wet-dry)

Start Condition: Dry *vs.* Wet

Some experiments were run to understand the importance of a wet or a dry initial starting phase for the seed performance. It is interesting to notice that seeds are generally launched by the parental plant in response to the dehydration of the awns. In this process, that will be investigated further in section 5, the seeds land in a semi-coiled configuration. Therefore, the "natural" starting phase of the cycle would be wet.

As showed in Fig. 18, in the wet starting phase, more than 60% of the seeds established after the first cycle, compared to 25% in the seeds in the dry starting phase. After less than 10 cycles no differences were seen between the two phases. This has a significant importance in the success of the *Erodium* dispersal strategy as the quicker the seeds can establish, the sooner they can start germinating. Therefore, the above results indicate that by coupling the launching and the coiling mechanism, *Erodium* plants are able to speed up the establishment process.

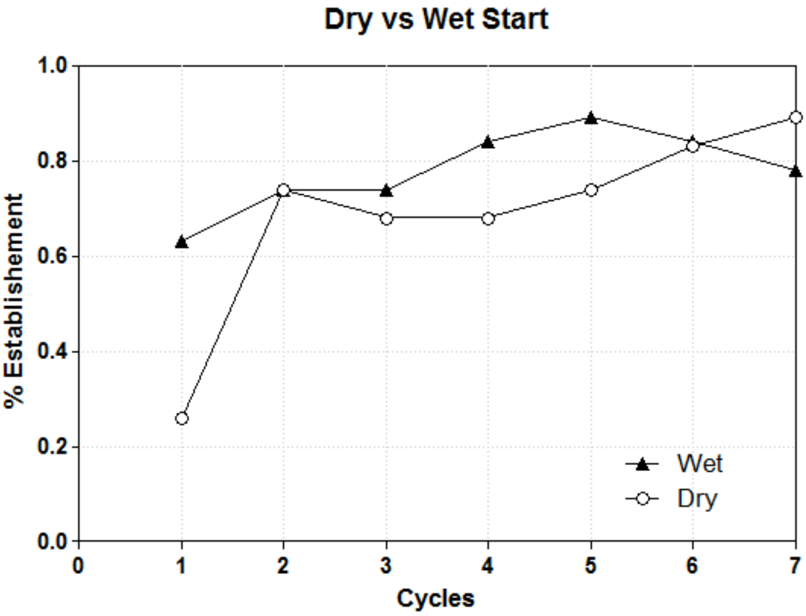

Fig. 18 Seeds establishment observed during the initial cycles where seeds present different start positions (Wet/Dry).

Cycle Length

Additional tests were done in order to understand whether the seed was benefitting from a total uncoiling of the tail. The length of the humid period and dry periods was modulated to 2h Wet - 2h Dry and 1h Wet - 3h Dry in two separate experiments and maintained for a total duration of 10 cycles. The first configuration was not sufficient to reach the fully coiled configuration, and this decreased significantly the performance of the seeds. In Fig. 19 the establishment rates for the Test soil in two different cycles are shown. The results clearly highlight the importance of both cycles for a quick establishment of the seeds.

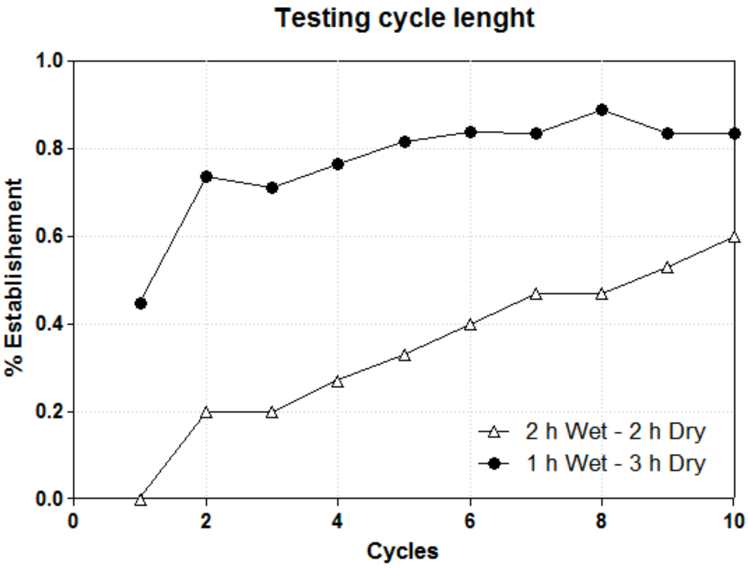

Fig. 19 Seeds establishment observed during 10 cycles in two experiments where the duration of the humidity cycle was different.

3.4 Basic principles of seed establishment and reasons of failure

The carpel plays a key role in the establishment process. If the carpel does not encounter an obstacle, it keeps on moving and turning with a clockwise or counter clockwise rotation, without any effect on penetration. For this reason in very flat or soft soils, i.e. pure sand or talcum, the seed is not able to block the carpel, as shown in Fig. 20. Therefore, if the soil is too flat or the seed head is not able to grip, the penetration cannot even start. However, it is important to note that with a free carpel the seed will move, thus increasing the likelihood of finding a crack or an obstacle.

Also the angle of the seed is important. It is influenced by the conformation of the ground but is also affected by the hairs in the twisting awn, which are accessories structures that enable the seeds to have a good angle of penetration (this features will be described in Chapter 4, where a thorough description of the seed is presented).

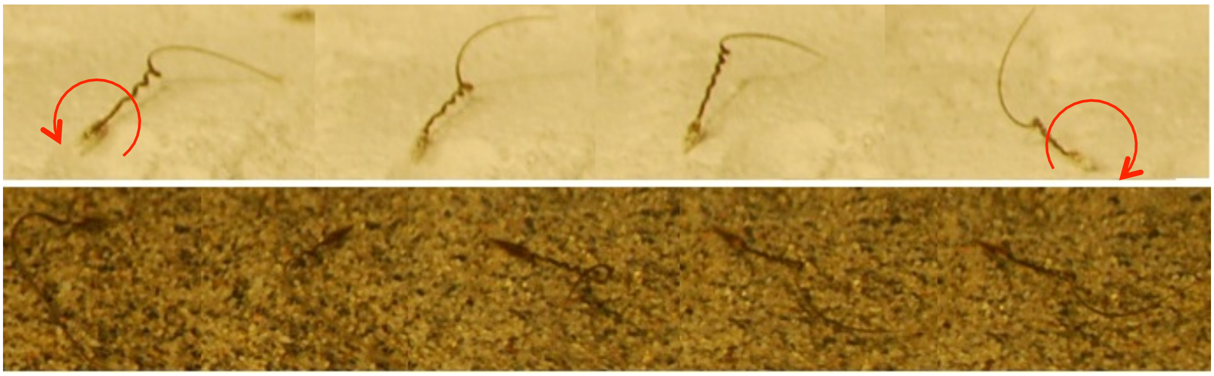

Fig. 20 *Erodium Cicutarium* seeds turning without being able to penetrate in talcum

If the particles are porous enough to let the tip of the seed into the pores, the continuous rotation can also lead to the penetration of the carpel into the rocks. Although this event is fairly rare, it has been observed for all types of granules used, i.e. perlite, expanded clay and pumice as shown in Fig. 21.

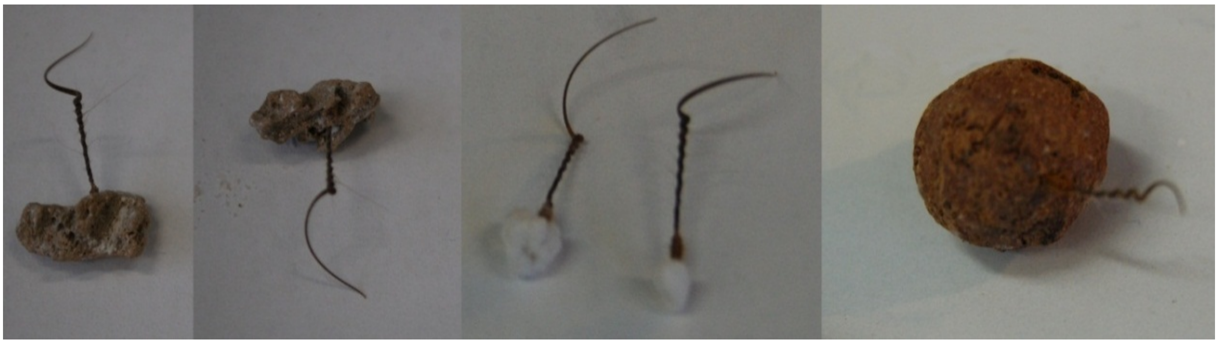

Fig. 21 Examples of carpels immobilized in rocks.

In Fig. 22 the distance travelled by a seed immobilized in a perlite grain is reported. When the seed cannot penetrate a crevice or a rock, due to the presence of the perlite grain, it will move onto the surface covering several centimetres every dry-wet cycle.

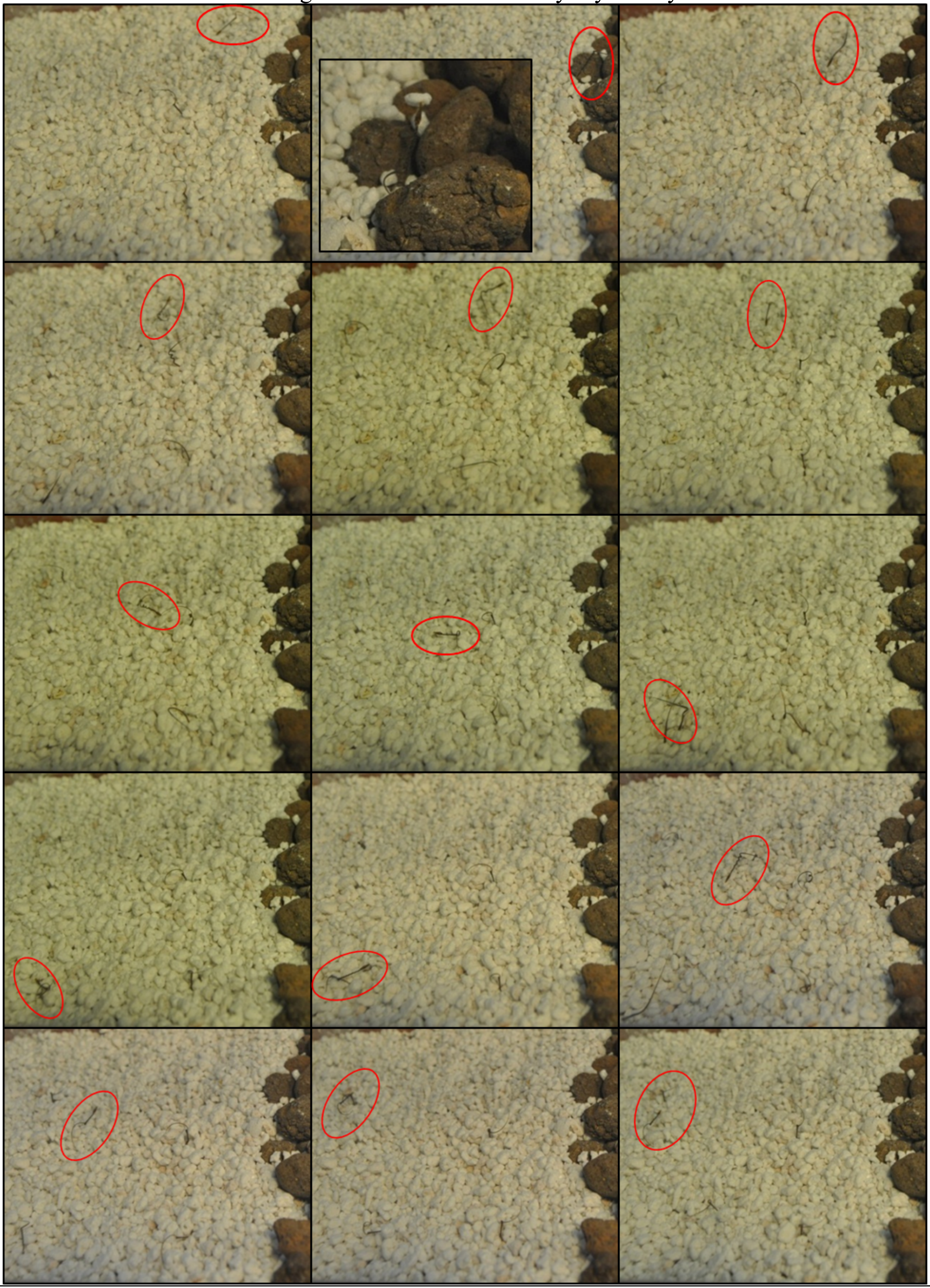

Fig. 22 Examples in which a seed above pure perlite rolls and moves on the surface as the carpel is blocked in a perlite stone (highlighted in the second frame).

During the cycles, if the seeds are free to move, they can get too close one to another and start to interfere, preventing the penetration. To avoid such phenomenon, a certain distance among all seeds has set before the start of each experiment: however, as the seeds in some occasions moved for more than 10 cm, we could always not prevent interferences. All interferences had a negative effect on the penetration of the seeds, causing the extraction of one or more seeds involved in the contact. Some examples are presented in Fig. 23.

Fig. 23 Images of several seeds interfering with each other during the penetration.

3.5 Conclusions

In all soils studied at least 80% seeds had the ability to penetrate inside the ground. Seeds were able to establish deeper in coarse and porous soils. As also concluded by other authors, the presence of cracks, obstacle and crevices is determinant for the performance. This because when the carpel does not encounter an obstacle, it moves around, crawling back and forth until it finds a place where to stop and start the burial process. The complete establishment of the seed into the soil was mainly observed in the Asteroid mixture, which was characterized by the highest fraction of particles bigger than 2 mm (i.e. more cracks and crevices), and the lowest angle of repose (i.e. less friction among the particles). More than 50% of the seeds established during the first wet-dry cycle, which suggests that the first cycle is very important for the performance. In fact, in nature plants propel theirs seeds thanks to the desiccation of the tissue. Therefore, when seeds land, they are desiccating, and they pass from a wet to a dry state. By doing so they are able to position themselves already with a good inclination angle, and start the drilling phase. On the other hand, when the establishment process started in dry (coiled) phase, there was a delay in the establishment of the seeds; therefore to accelerate the burial process it is important to start the cycle from a straight configuration. The length of the cycle and the subsequent partial coiling or uncoiling of the seed influenced its penetration performances.

4. Accessory structures and their contribution to the performance

4.1 Morphological traits

Some of the morphological characteristics of *Erodium cicutarium* seeds are resumed in table 6 and 7. The seeds had an average total weight of about 1-2 mg, and half of the mass is in the carpel, where the embryo is located, and the other half in the dispersal unit, the tail.

Tab. 6 The table presents a schematic representation of the seed on right and its main features on left.

	Average (14 seeds)	**SEM**
Wet		
Tail + seed	52.58 mm	0.98 mm
Seed	7.34 mm	0.15 mm
Tail	45.23 mm	0.90 mm
Dry		
Number of coils	6-9	
Uncoiled tail	12.55 mm	0.29 mm
Coiled tail	18.40 mm	0.46 mm
Diameter D1	0.300 mm	
Diameter D2	1.5-2.0 mm	

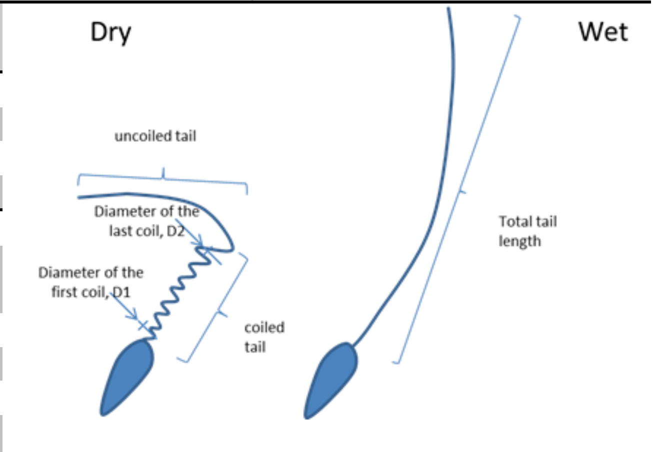

The coiled tail creates a spiral whose radius is increasing with the distance from the carpel: the diameter close to seed head is half of that in the final part of the tail (see also Fig. 43 in §6). The final shape of the spiral is tighter closer to the seed and looser towards the end. The number of coil can vary among ecotypes from 6 to 9.

Tab. 7 The weight of two ecotypes collected in different zones of Italy.

	Total weight (mg)	**% weight allocated in the carpel (mg)**
E. cicutarium (Piombino)	1.34 ± 0.04	0.49 ± 0.03
E. cicutarium (Island of Capraia)	1.72 ± 0.12	0.41 ± 0.02

In the seeds, the main features that help in the establishment into the soil are: a sharp tip, the spines along the carpel, the hairs along the awn, and the coiling-uncoiling movement of the awn (Fig. 24).

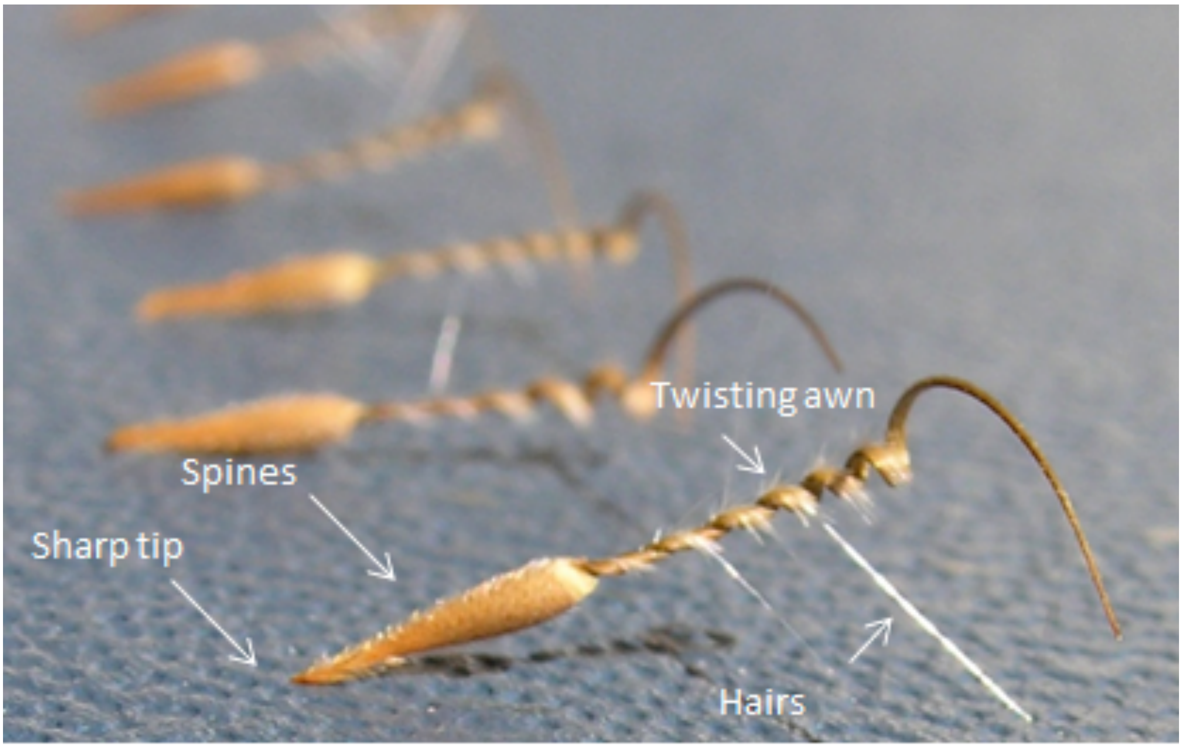

Fig. 24 Accessory structures of the seed: the sharp tip and the spines of the carpel, and the twisting awn and its hairs.

4.2 Structure of the carpel, the spines and the tip

The carpel has a conic structure with a sharp tip and short stiff spines or barbs along all its length. As shown in Fig. 25 they range from 180 and 480 μm. The longitudinal section of the head of the seed is an acute triangle, and the spike forms an angle of about 15° degrees. This is a very robust structure able to penetrate inside hard materials (e.g. stones, see Fig. 21 in §3.4). Looking at the disposition of the spines, there is a symmetry in the carpel, which can be described like an harpoon with a longitudinal plane of symmetry. The yellow arrows in Fig. 25 follow the orientation of the spines. The carpel can rotate in both directions, and therefore this uneven distribution allows the anchorage in both directions.

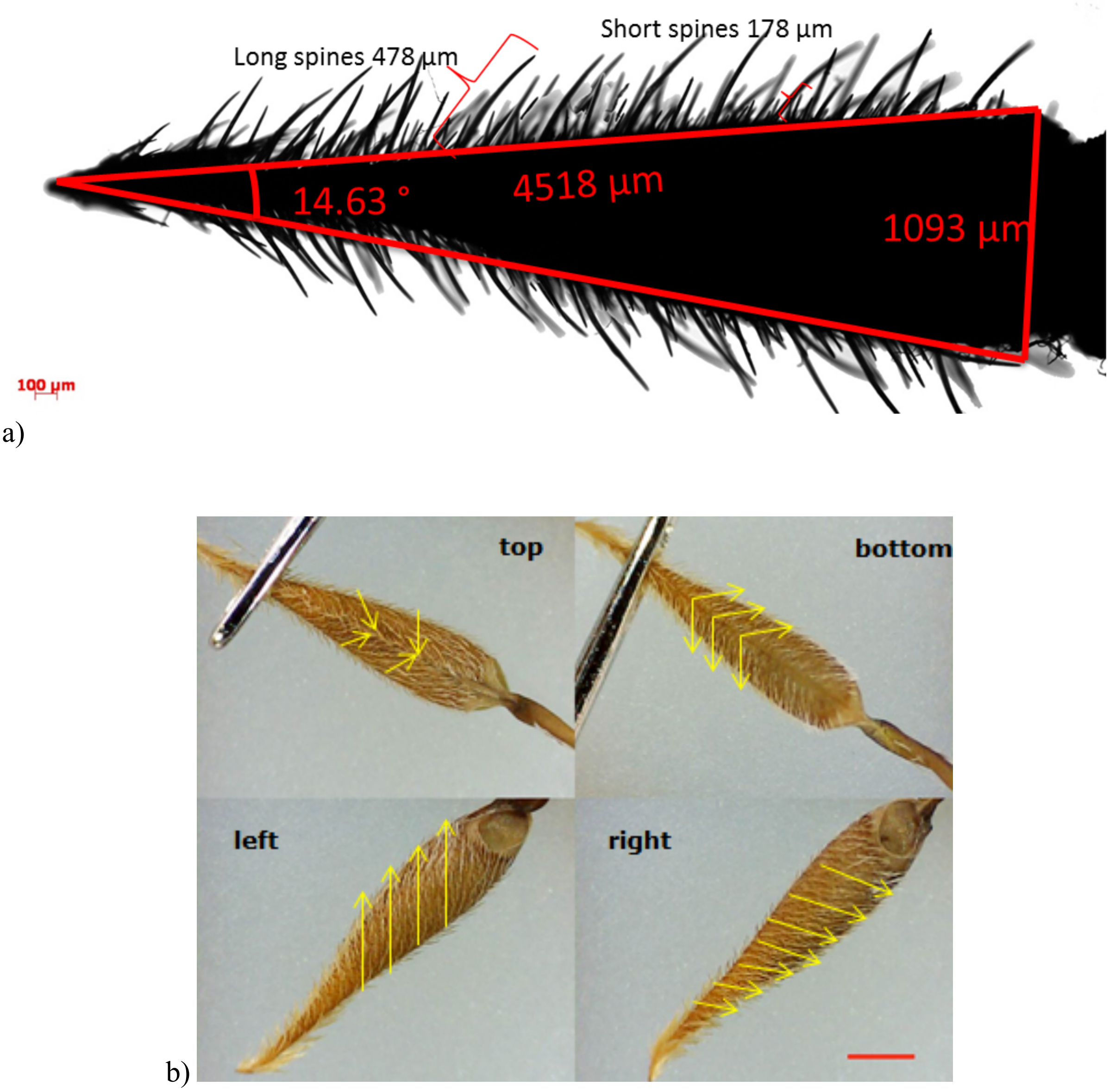

Fig. 25 Short stiff spines or barbs on the carpel are shown in the top (a). In the picture at the bottom, the mechanism of anchorage is revealed. The asymmetric distribution allows one side to be always opposite to the direction of extraction. At the same time one has no function when the seed turn back and vice versa (b).

4.3 The hairs along the awn and the angle of penetration

The hairs along the tail, situated in the external side, have a crucial role as they keep the seed at a certain angle with the substrate, together with the tail. In fact they provide the third touching point that allow the seed to achieve a certain angle with the soil. They are aligned with the tail when the tail is wet, and therefore enabling the wet seeds to lay flat on the surface. Then, during the coiling, the hair come out tangentially as shown in Fig. 26, and cause the seeds to rise from the surface and achieve a certain angle. The change in the disposition is a passive geometric feature, due to the change in shape of the awn. The presence of the hairs along the awn allows an up and down movement, that helps the penetration. Fig 26 right shows the change of orientation of the angle of rotation. This behaviour resembles the movement observed in a growing root into the soil, called circumnutation (Stolarz 2009), and it contributes to reduce soil resistance (Fig. 27). This angle was measured and varied from 6 to 24 degrees.

Fig. 26 Disposition of the hairs

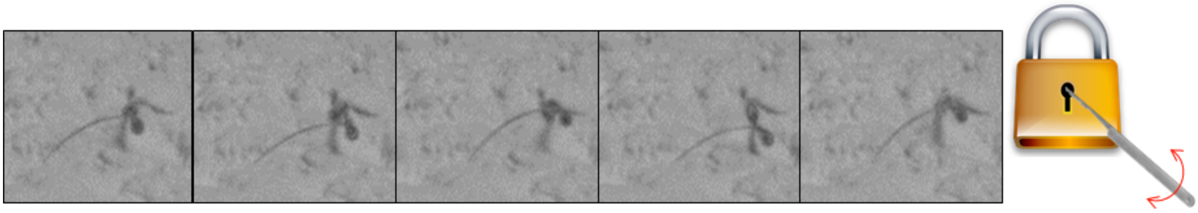

Fig. 27 Rotational movements of the seed whilst it tries to minimize the hardness of the soil by changing continuously the direction of penetration.

4.4 The twisting awn

Thanks to the coiling and uncoiling of the tail, the carpel, once a crevice has been found, rotates clockwise and counter clockwise and eventually penetrates the soil. Most of the work is done by the tail as it turns continuously: this enable the seed to penetrate into the soil. However, when the seed is placed in a vertical position the tail turns with little or no effect. A careful observation of the time-lapse videos, we discovered an interesting feature: the first and the second coils of the tail can result in a very irregular trajectory (Fig. 28).

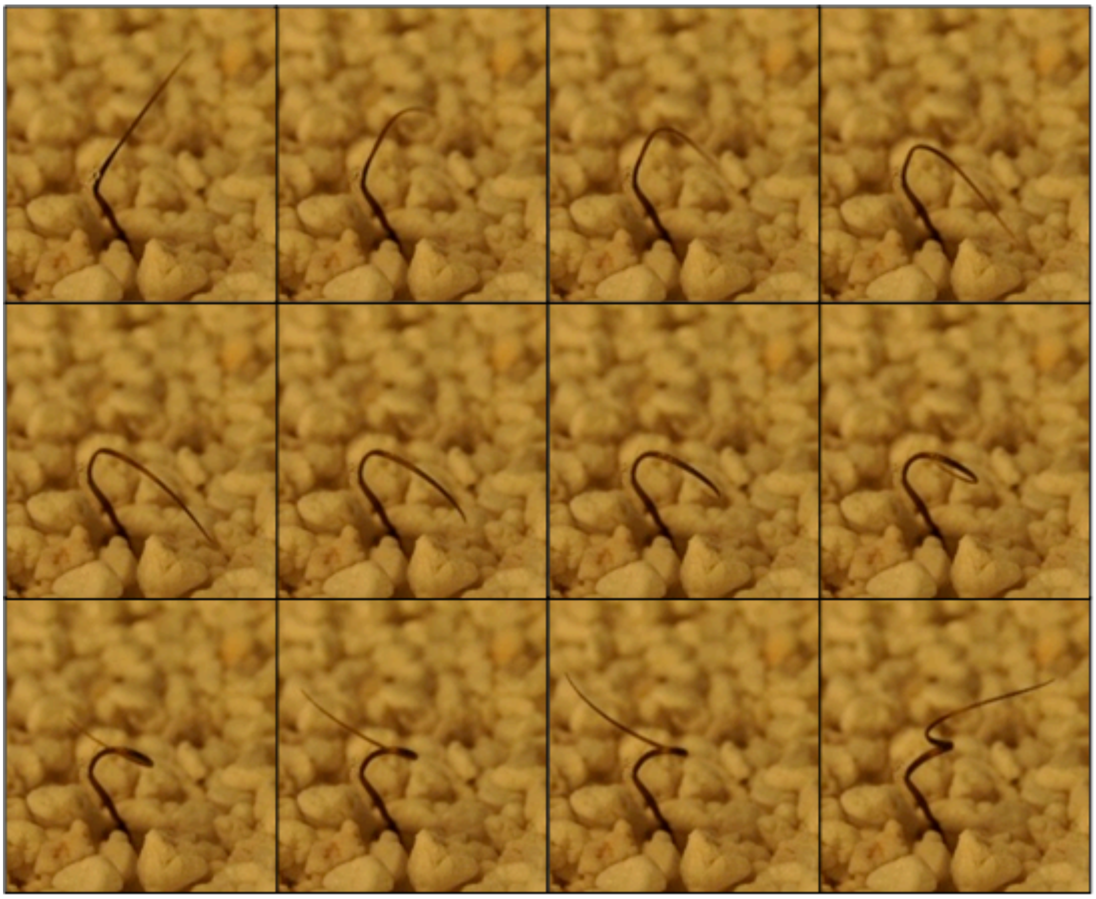

Fig. 28 First coil of the seed after a wet cycle. The last portion of the tail is curved and grasp directly into the soil.

Using two cameras we were able to rebuilt the 3D trajectory of the tail (Fig. 29) and we could observe this feature. With the exception of the very first coil, the tail follows a planar trajectory, whereas the first coil follows an irregular path that helps the seed to achieve a more vertical position.

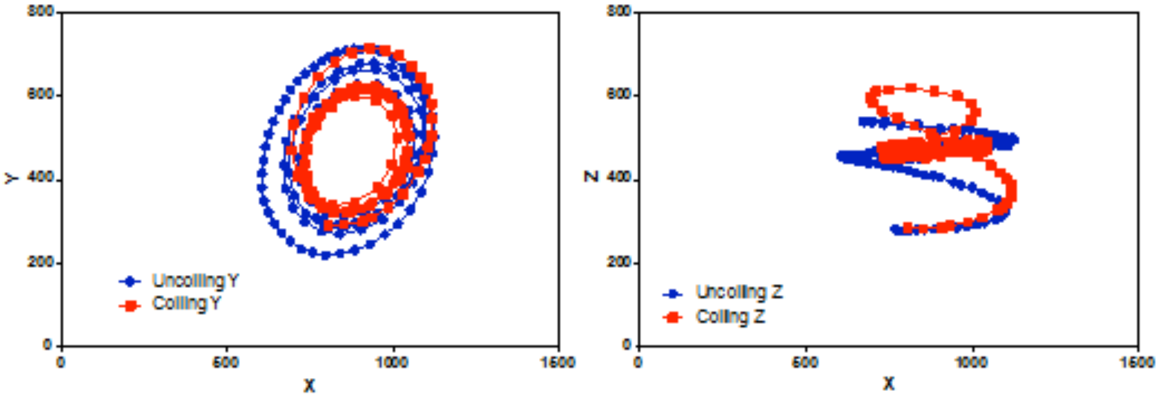

Fig. 29 3D trajectory of the tail built by Stereovision during the coiling and uncoiling where x, y, z are the axes of the Cartesian coordinate system. In red is marked the trajectory during coiling movement and in blue during uncoiling.

To conclude our set of observations, we tried to measure the strength of the tail on a flat surface to have an order of magnitude for our models. The experiment was done on a fine scale. The seed was blocked around a needle, and placed above the scale plate. Only the tail was allowed to touch it, and the maximal push of the tail was recorded during the coiling of the awn (Fig. 30).

When the equilibrium was reached, the tail was set free to rotate and then replaced again on the scale, to record the strength of the second coil, and of the third. Maximal torque was measure for the three coils of the awn. A similar approach was used to measure the maximal push of the carpel. The tail was blocked and the only motion allowed was the rotation. The seed was enclosed in a glass capillary tube placed above the scale. When a drop of water was placed inside the glass, the seed started uncoiling and the push over the scale was recorded (Fig. 31).

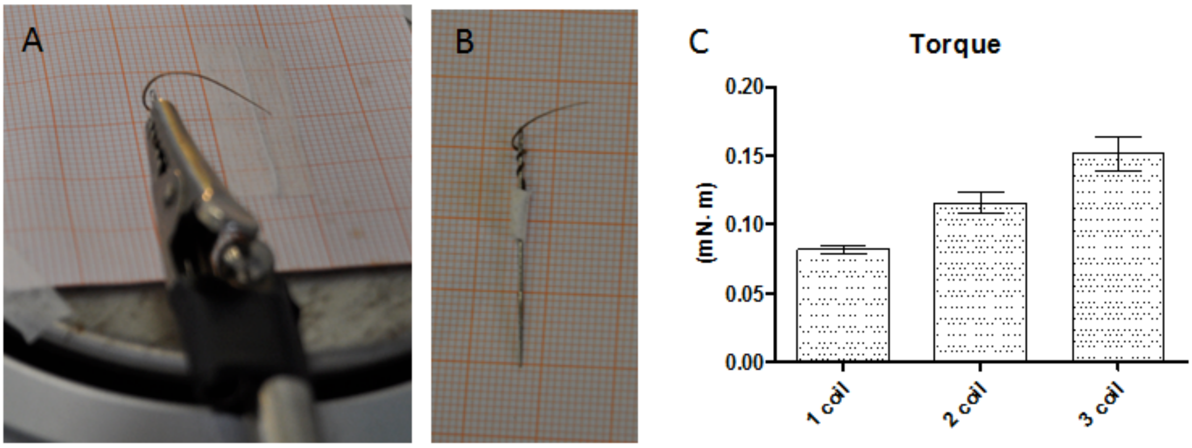

Fig. 30 Experimental set-up (a, b) and results (c) of the maximal torque measurements of the tail.

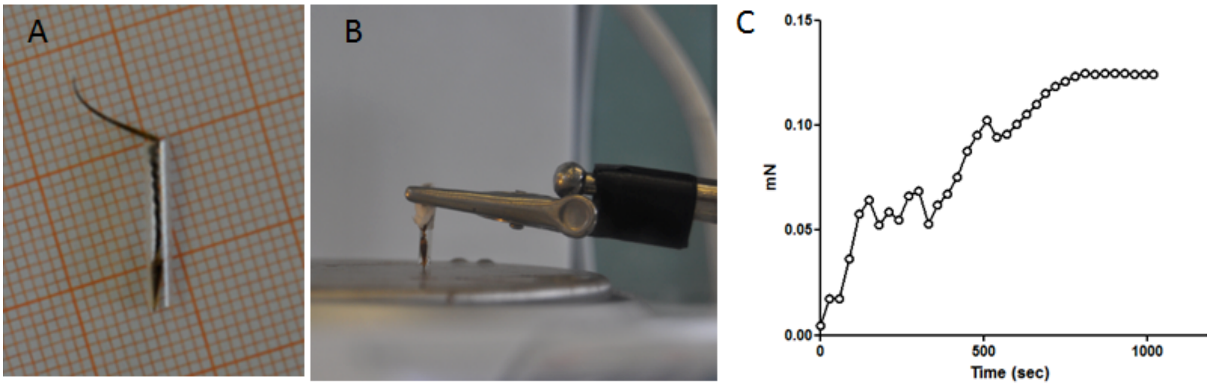

Fig. 31 Experimental set-up (a, b) and results (c) of the maximal push of the carpel when all the seed is blocked.

4.5 Conclusions

All the accessory structures are equally important for the performance of the seed. The spines on the carpel help by allowing a preferential forward motion of the seed during the movement. The hygroscopic motion of the tail is fundamental for the overall drilling movement, and together with the awn hairs, it modifies the angle of penetration to reduce the hardness of the soil. The hairs along the awn remain in an aligned position and have no influence when the seed is wet, but they are important once they come out in the drying phase for the maintenance of a certain angle and to scrape away some particles with their rotation. We observed a particular path of the tail during the first coil, in particular during the transition from the wet to the dry phase. Nevertheless, at this stage, we do not have sufficient data to conclude that one of the two motions (e.g. coiling or uncoiling) is more effective than the other.

5. LANDING PHASE

5.1 Importance of the landing for biomimetic transfer

This part of the project focused on the landing phase in order to understand its contribution in the establishment of the seeds In fact when a seed departs, the explosive elastic movement of the tail causes a very fast spinning of the seed (Evangelista et al. 2010). Here we tried to elucidate if this mechanism has been developed only to increase the dispersal distance or has any effects on the penetration of the seeds. The landing phase is responsible of the initial state of the drilling performance of each new seed. The study of this mechanism directly by observing the nature is an opportunity to analyse features evolved by nature to help the development of a device.

Compared with a seed of the same mass without the hairy awns, the drag is expected to significantly influence the trajectory, causing a decrement in the maximum dispersal range. In addition the awn is very important both for the initial elastic force, which drives the lunch phase, and for the subsequent burial phase by drilling the soil once the seed has landed. However, it is important to consider that species with intricately branched and hairy awns, that have a high-drag, are mainly dispersed by wind: occasionally, this results in a very long dispersal distance. This lunch mechanism has been studied by Evangelista et al. (2010), but its effect on the landing phase and how it affects seed burial performance has not been considered. The speed before landing and the velocity of several seeds were measured to understand how the initial elastic dispersal mechanism affects the impact on the soil.

5.2 Experimental procedure

Experimental setup

The *Erodium* landing phase was filmed using a high-speed video recording camera, operating at 100-125 frame s^{-1}. The setup consisted of a Charge-Coupled Device recording camera (CCD), a tray filled with a substrate where seeds landed. Four incandescent lights, each of 200 watt, were used: of these, three were situated in front of the camera and one above the tray. As landing substrate we used talcum powder which formed a white and clear background enabling us to observe the imprint left by each seed when landing. Shutter speed was set at 1500 µsec to limit the blur effect, and the experiments was conducted in a well illuminated place (with a resolution of 800x600, clear frames were obtained with four lights each with a power of 200 Watt). Next to the set-up a second video camera (HD camera operating at 25frame s^{-1}) was installed to monitor a tray adjacent to the first one, and filled with ½ talcum powder and ½ perlite (Fig. 32A). This addition was performed for two reasons: first to increase the chances to film a landing although with less time-definition and second to observe the behaviour in a different substrate.

The first approach for the study of the landing implied the problem to register exactly the end point of the seed trajectory where a still CCD camera is continuously recording. The use of entire plants does not suit this approach for two main complications: the first one is the waiting time of the launch and the second one is the difficulty to predict with accuracy the impact site. Furthermore, the acquisition needs an optimal contrast and a very good illumination. Collecting data at 125 fps generated a large quantity of information not easily manageable, depending on quality of the image, which besides creating files with huge size also limited large dimension (i.e. limitations due to the speed of data exchange between the camera and computer). Moreover, a large amount of light and a good contrast were required by the camera. For this reason, it was not possible to film a very large site with the consequent decrease of the possibility to identify the point of landing. It was therefore necessary to perform a very high number of launches to achieve our goal. As a result of these limitations, in the present project, the fruit was detached from the mother plant and a fracture between the carpel and its linking structure was manually made. The last force to detach was usually given by the temperature of the illumination, which dried the awns to the point of launch. This method is an easy way that avoid recording the launch of a seed directly from the plant, and it can also be used to mimic as much as possible the natural conditions.

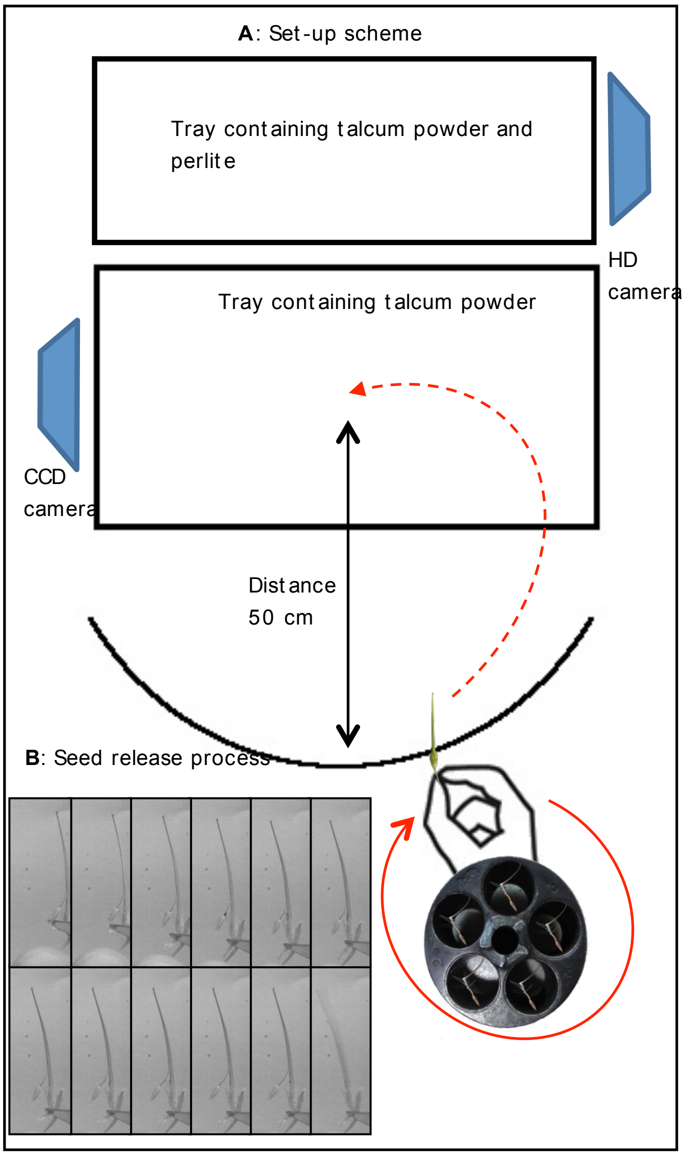

Fig. 32 A: experimental set-up. B example of a detachment phase resume in 12 pictures (about 20fps).

5.3 Detachment phase

Our launching procedure was achieved using a harvested bird's beak fruit at a good grade of maturation. The fruit was grabbed with the fingers to the base, taking care not to touch the carpels. Once placed at a distance of about 50 cm, the carpel was scraped with a cutter, from the point of attachment to the base (see Fig. 32B). Using this technique the tail started its internal bending and the seed was fired in a moment, helped by the heat of the lights. Simply by rotating the hand and detaching sequentially all remaining seeds, several take-offs could be done with a single bird's beak fruit. The first launch in this “five bullet rifle” (Fig. 32A) was used to predict and estimate the subsequent trajectories, increasing in this way the possibility to centre the point of landing. The launch dynamic of a group of seeds belonging to the same fruit was found to be very similar. Using this procedure an average distance of approximately 50 cm between the tray and the starting point was selected, in accord with previous studies (Stamp 1989, Evangelista 2010). The starting height has been kept at 15±5 cm as we observed in the majority of the plants. In several cases, the height of the fruit has been demonstrated to reflect weak statistical effects on dispersal, with the exception of plants under natural conditions, were ballistic dispersal interfered with neighbouring plants (Stamp 1989).

5.4 Factors affecting the dynamic of the launching phase

As flying characteristics of each seed are unpredictable, some considerations should be reported since flying distance is strongly influence by several factors. First of all the inclination of the fruit can generate various types of parabolas as shown in Fig. 33.

This behaviour has been shown for similar dispersal mechanism and it has been modelled in the past (Swaine 1979, Lucas 1982). A straight or acute angle results in a longer distance compared to an obtuse angle. In nature the majority of the seed are disposed in a vertical position. This fact can be in conflict with the logical idea that evolution privileged long dispersal mechanism, but it has been demonstrated to be a suitable solution to limit the interference of neighbouring plants (Gross 1982, Stamp 1989). Nevertheless some of them have been found to be inclined and the launch angle can differ from value reported from literature, in Tab. 8. This change in the starting position generates different trajectory. The paths that are derived from acute angles generate take-offs that can have a long distance but have more probability to impact tall obstacles. While in the case of an obtuse angle, as well as for the vertical position, the plant is able to disperse its seeds in the air reaching

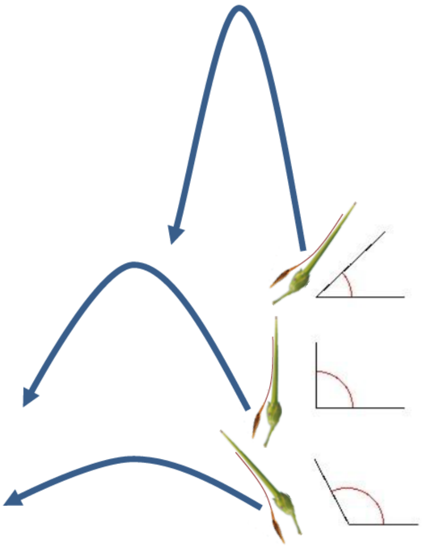

Fig. 33 Relation between the trajectory of the seed and the angle of inclination of the

a superior height. This behaviour, even if it reduces the flight distance of each seed, has many advantages, such as the ability to "climb" objects and reach high places like fissures in rocks or in taller plants, limiting space competition with other plants or greatly increasing the dispersion in situation of strong winds (Zeide 1976, Stamp 1989). All this observations are in accord with previous study performed by Evangelista (2011).

5.5 Seeds conditions

Tab.8 Kinematic data of *Erodium cicutarium* initial phase of launch and predicted values by Evangelista et al. (2011).

Parameter	Observed (mean ± s.d.*)	Predicted
Initial launch speed (m s^{-1})	4±2	5.1
Initial angular velocity (rad s^{-1})	200±100	182
Launch angle (deg)	40±30	set to 40
Desiccation at launch (estimated from shape)	0.1±0.05	set to 0.1
Distance thrown (m)	0.51±0.08	0.50

*Means of eight launches.

Seeds were harvested and preserved until maturation for several days. A fast drying during the maturation, in few cases caused the entanglement of the last portion of the tail in the central fruit structure. This effect is showed in nature when all seeds in a fruit twist completely before being launched (i.e. Fig. 2). For this reason all seeds used in this study have been subjected to the same condition; they were harvested in the final state of maturation, and preserved for a maximum of 2-3 days at room temperature attached to stems, where all leaves were cut off to prevent leaf rot. In some cases, a pre-treatment, which consisted in a desiccation at 40°C for 10 minutes, was made before the procedure to increase the explosive power of seed dispersal. This pre-treatment was not necessary when the fruit was ripe to avoid any risk of accidental release. In any case in nature, *Erodium* plants usually shoot its seeds in very sunny days and in arid period, and thus this treatment could mimic the dry condition of the moment of the launch in nature. Coiled seeds maintained at different temperature of 24°C, 30°C and 50°C for one hour did not show any increase or decrease in the speed of uncoiling once immerged in water. This observation lead us to the hypothesis that desiccation factor and the subsequent change in the elastic power explosion during the launch is the most important factor affecting the trajectory of the seeds. In addition, it is well known that for ballistic physic of object of very small dimension, as the seeds of *Erodium*, both size and weight frequently are of secondary importance because of small differences derived by effects of gravity and air friction.

5.6 Data analysis

Several launches were captured on high-speed video cameras and were used for the calculation. The videos obtained the normal HD camera (20 fps) were also utilized to refine the results. All launches that were too weak were not considered.

5.6.1 Landing categories

The recorded landings can be divided into different categories that are presented below, together with some examples.

Category 1

Seeds in this category entered the soil like a dart. Therefore they buried immediately at the landing (Fig. 34).

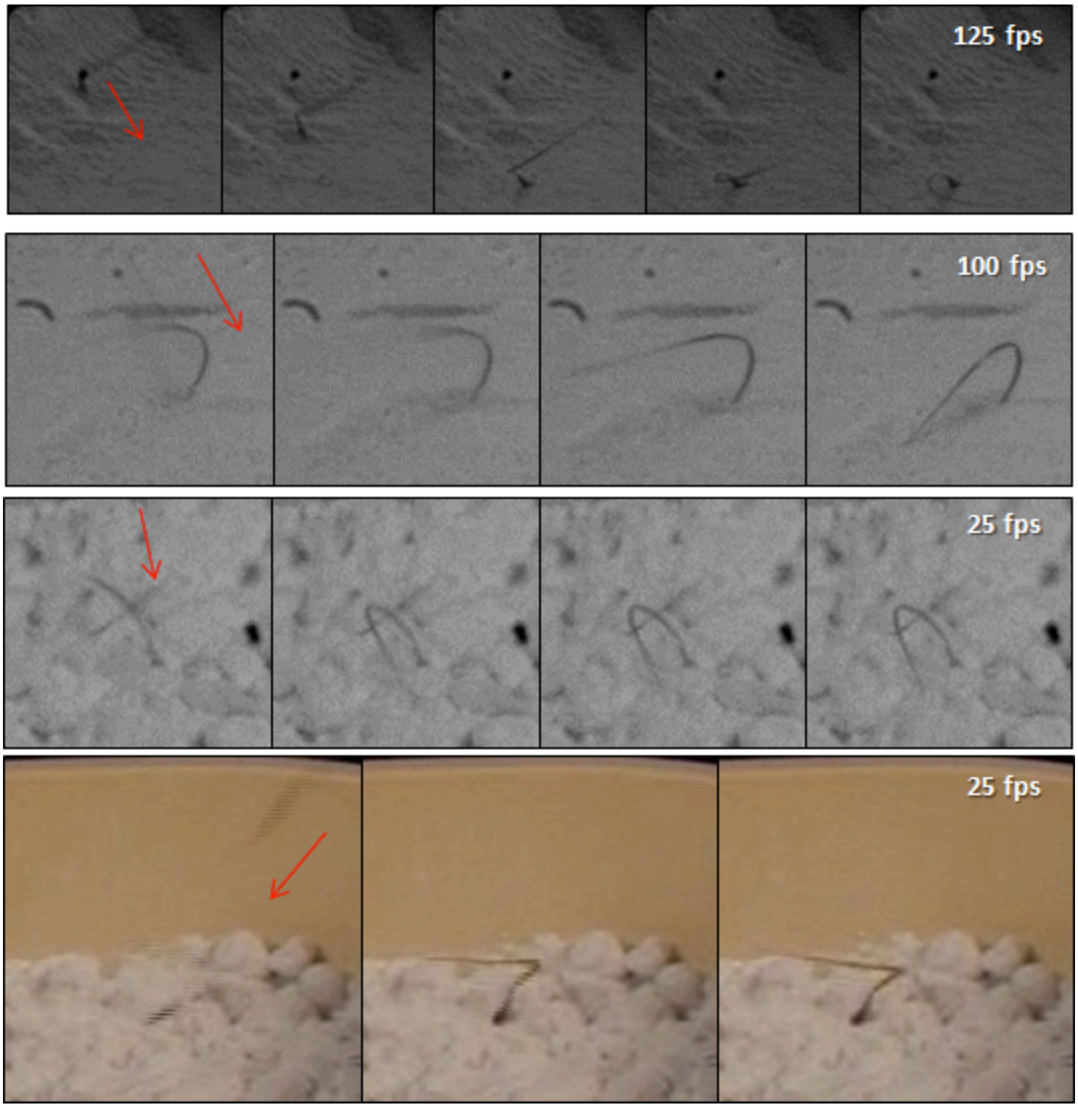

Fig 34. Category 1. Images were collected with the CCD or the HD video recording camera. Red arrows indicate the trajectory of the seed before landing.

Category 2

The seeds landed on the tail, and bounced or rolled before stopping (Fig. 35).

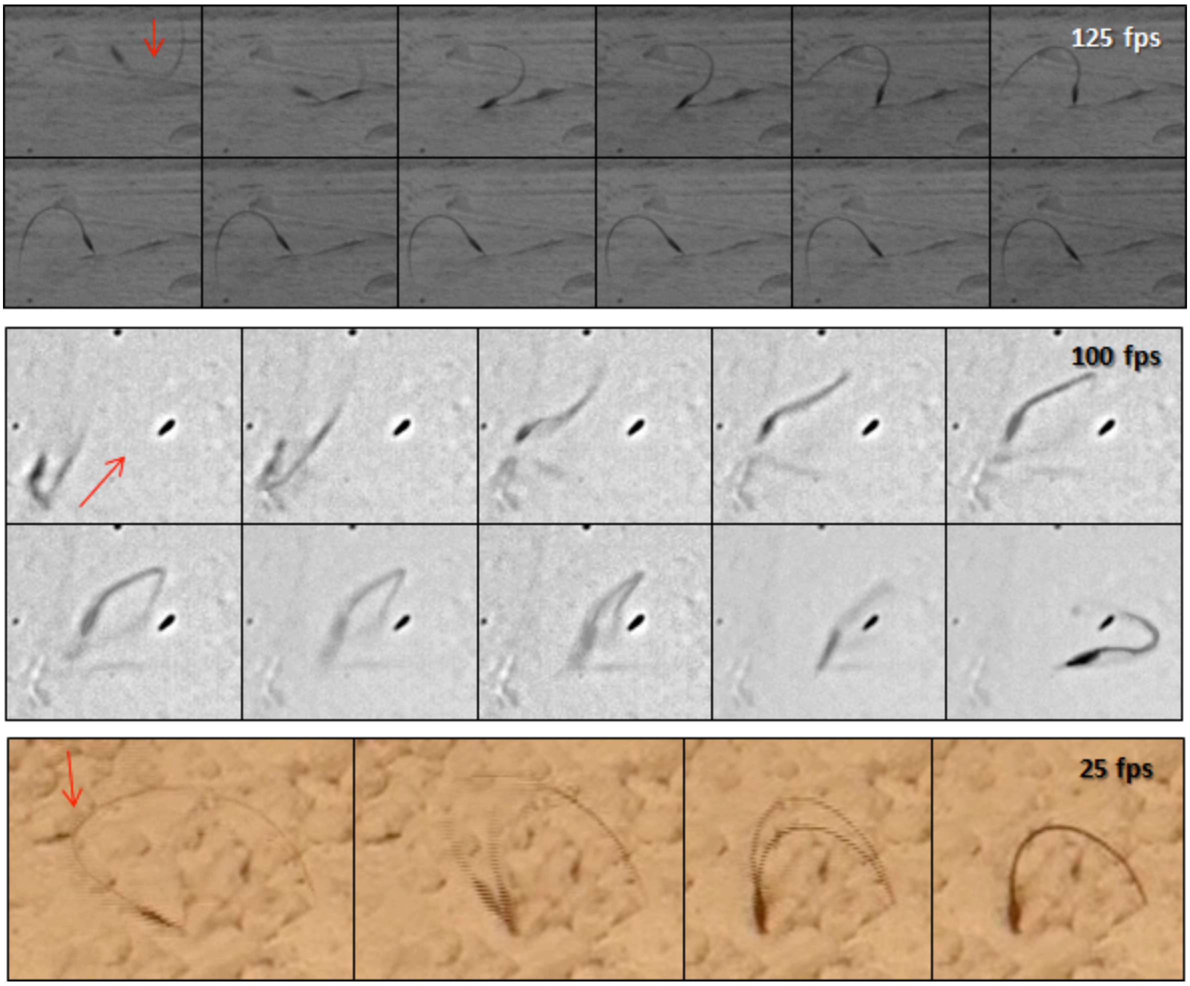

Fig. 35 Several examples reported frames by frame of a seed bouncing and rolling after landing. Red arrows indicate the trajectory of the seed before landing.

Category 3

Seeds impacted the soil with the carpel and bounced around it (Fig. 36).

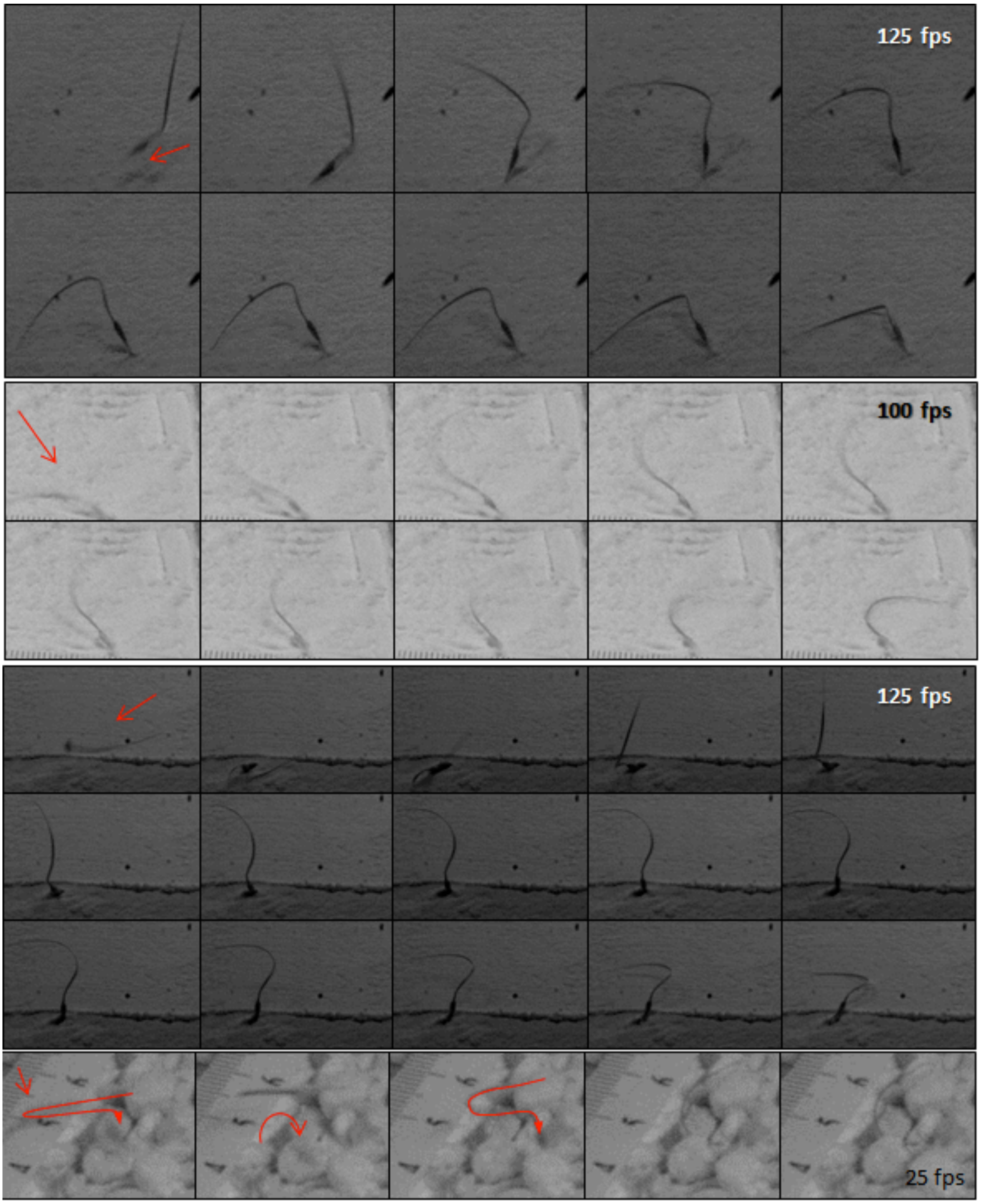

Fig. 36 Several examples reported belonging to category 3 in which seeds impacted the soil with the carpel and bounced around it. Red arrows indicate the trajectory of the seed before landing.

5.6.2 Coiling after landing

The first coiling after impact has been considered as part of the final process of the landing. Here below some example of seeds coiling after impact are shown (Tab.9):

Tab. 9 Several examples reported frames by frame of all explicative situations of the coiling movements after landing are shown below:

Seed belonging category one, burying themselves inside the soil. All these seeds are in a favourable position to drill the soil after few coils and the effect mechanism causes effective penetration.

Collected by 25 fps HD camera on a mix of ½ talcum powder and ½ perlite.

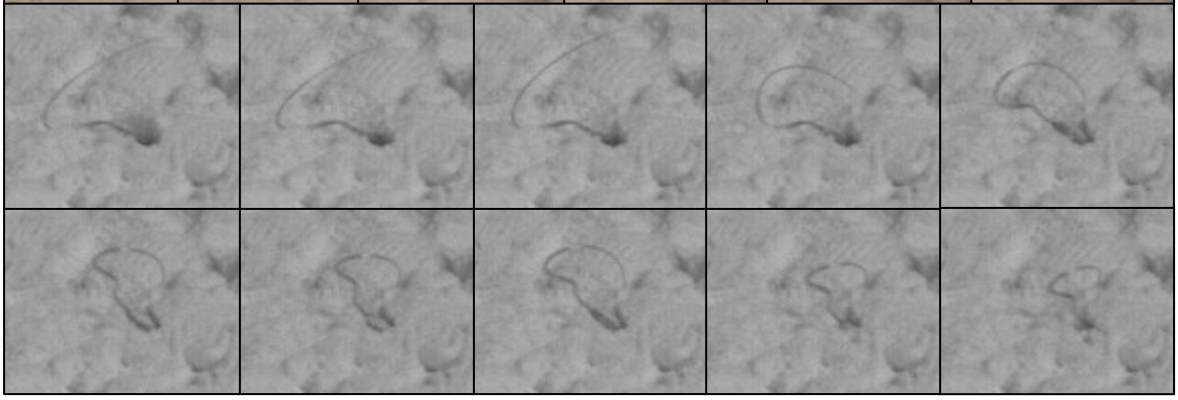

Seed belonging category two, falling to the side. Seeds which fall to the side can stand up and lay down after the tail coiling:

The first frame sequence has been collected by 125 fps CCD camera on talcum powder and the second by an HD camera on a mix of ½ talcum powder and ½ perlite.

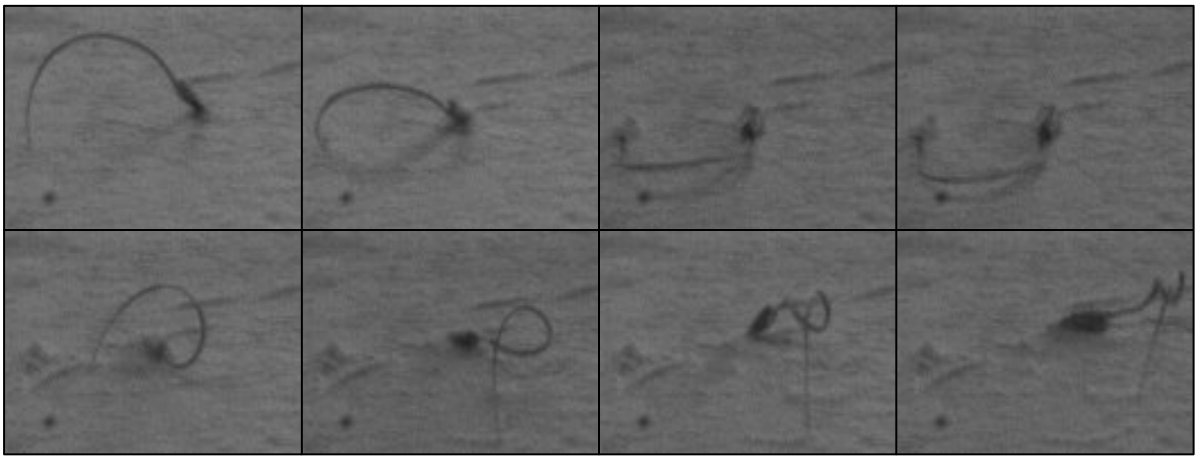

Here below two examples of seeds that fail to anchor their carpel and because of the coiling are driven out. Collected at 25 fps HD camera on a mix of ½ talcum powder and ½ perlite.

Here a seed from a steady position in which seed lies down, disposes itself to start the penetration phase. Collected at 25 fps HD camera on a mix of ½ talcum powder and ½ perlite .

Impact position

The impact position of the seed has been monitored in all analysed launches. The movement as the rotational force of the seed is influenced by the trajectory, and the impact to the soil presented a quite variable angle and dynamic to be simply resumed. The image examination described at least three categories of landing.

1. Seed immobilized into the ground.

This category includes all seeds that reach immediately the goal of burying themselves and penetrating the soil directly as a result of the fall (no additional movement of this seeds was seen except for settling arrangements due to vibrations of the elasticity of the tail and the subsequent coiling). Usually this behaviour occurred when the impact to the soil corresponded with the moment in which the spike of the carpel was turned in favourable position (Fig. 37), thanks to its weight and the final shape of the seeds, which is slightly curved. It was also noted that often a seed that directly penetrated the soil with a very vertical position did not achieve any contacts with the soil after the first complete coiling.

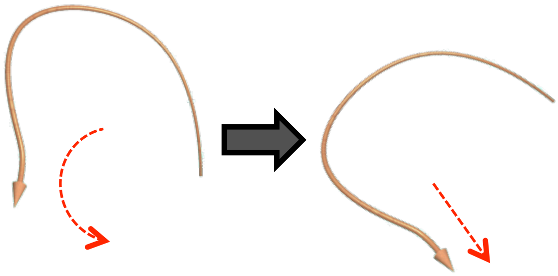

Fig 37. Image of a common fall position in which a seed penetrate directly the soil.

2. Seed Revolution.

Another category is that of the seeds which touch the soil with the curved portion of the awn, revolving (Fig. 38).

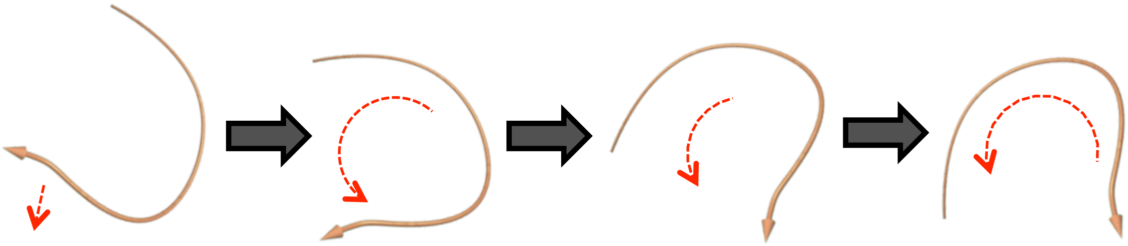

Fig. 38. Image of a seed revolution after the contact with the soil.

This event generated the elastic response of the seed structure, which resulted in a turn. Usually the weight of the carpel drove the tail revolution. This is related to the angle of impact with the ground and this representation is only a simplification of a common behaviour after this impact. Seeds that landed in this way, moved away from their position of origin, from few to up to several centimetres. In this position both the grade of desiccation, which modifies the tail curvature, and the trajectory generated different elastic responses. In the case of opposite impacts, when the tail pushed against an obstacles, the seeds repetitively turned, before in a direction and then in another as shown in Fig. 39.
During this kind of revolution the seeds carpels was the main part of the seed in contact with the soil, and the final position could be maintained until the tail bend in response to the loss of balance.

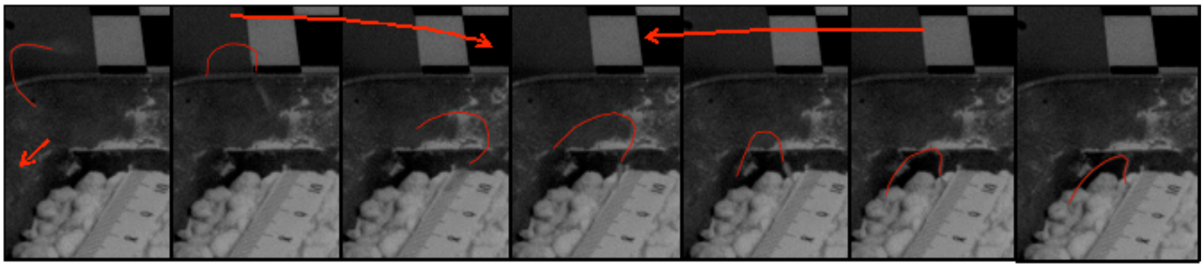

Fig. 39 Seed that after hitting the container, fell down in the soil and rebounded again to the container and stood for a while in a in vertical position.

3. Tail Rotation.

The last group of seeds considered in this study is formed by seeds which fell into the soil with all parts, mainly the carpel, or simply lay flat on the surface (Fig. 39, left). Virtually if a seed lies on a horizontal plane after it is launched, with a shape similar to a semi-circle, all parts of the seed touch the ground with the exception of the parts of the seed which are slightly curved. So the impact position is the same as placing the open seed on the ground, where all its parts are in contact with the soil. Moreover, in the majority of the observations, the seeds stopped their flight immediately, especially the ones in the talcum, after lying on the ground. So this landing results in only the first step of Fig. 40. However, as in the previous category, sometimes the impact speed forced the seed to rebound or to rotate around the axis that runs along the length of the carpel, without tipping (Fig. 40). This effect caused a tail rotation in the longitudinal axe of the seed spike.

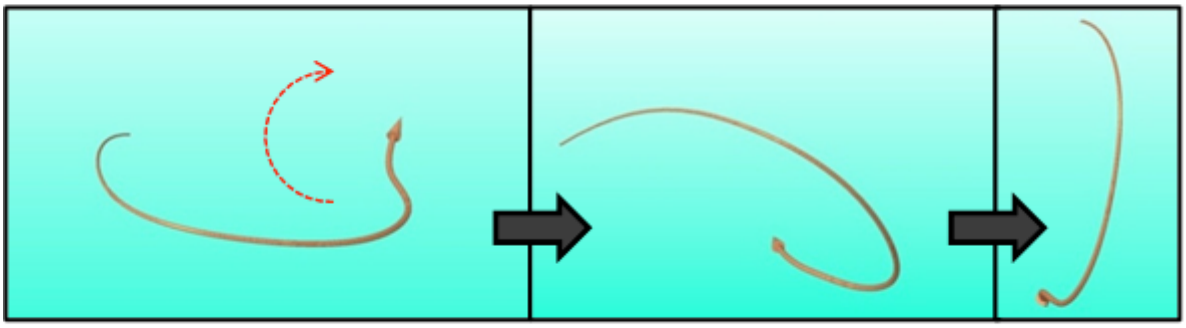

Fig. 40 Image of the tail rotation of a seed after a landing impact. The row indicates the direction of the rotation of 90° respect the ground.

4. Unsystematic movements.

The last category of the landing is represented by seeds that exhibited mixed features among these three groups, i.e. seeds which presented the carpel in a favourable position but because of the torsion of the tail went out the substrate, seeds which after the rebound with the ground penetrated the soil or seeds which simultaneously showed movements belonging to more than one group.

5.7 Results

The landing speed was approximately 1.4 ± 0.5 m s^{-1}, as shown in Tab. 10. The revolution of the seed has been predicted to be about 53 ± 16 m s^{-1} but this value is strongly affected by the centre of gravity of the seeds and the position of the carpel respect to the tail. In a complete turn it can change considering only 6 frame of 1/125 sec from 20 up to 100 m s^{-1} when the centre of gravity is working positively with the gravity vector. Tail rotation was observed to be more regular along a 180° torsion and with an average speed of almost 43±7 m s^{-1} and with a similar value for all different frames.

From a total of 45 launches observed with the CCD camera and the HD camera, 27% of the landing fell in the first category (immobilized seeds). We included in this category all the seeds that did not penetrate directly the soil but fixed themselves in a favourable position and were therefore able, with only a few coils, to enter the soil. About 33% of landings were seeds belonging to the category two, where a seed was able to complete a revolution after falling on its side. The shape of the seed was found to affect this behaviour, and usually when a seed was very dry it turned its spike in a way to get an advantage from this rotation in order to set the curved part of the carpel in a crevice. Seeds that landed in the pure talcum powder rolled down less than in the mix of ½ talcum powder and ½ perlite talcum. This occurred as a soft ground (i.e. talcum) absorbs the elastic rebound compared to perlite: indeed, in the latter soil seeds that rolled could move for more than 10 cm. It is also possible that in this landing, the seeds remained upright in an "L" position before coiling and falling down. On the other hand 31% of the launches fell into the third category, that of seeds which lay down on the soil. The difference between this category and the first one can be sometimes linked to the slow coil movement of the tail, which resulted in a perfect circular shape, whilst usually seeds which centred and penetrated directly the ground were more curved. These seeds anyway are able to wrap objects like big rock or paper foils and exploit them as anchorage and support to insinuate into the soil. The remaining 9% of the seeds showed highly variable movements and fell into the fourth category of unsystematic movements. A preliminary analysis on seeds that impacted against an object (e.g. the light) before falling down shows that they can lose up to half of their energy (average of two seeds about 0.82 m s^{-1}).

Tab 10. Landing speeds values registered during landing impact.

	Mean	Stand. Dev.
Average landing speed (m/sec)	1,39	0,297
Seed revolution speed (rad/sec)	52,79	16,04

Impact position distribution by categories			
1°	2°	3°	4°
26,66%	33,333%	31,11%	8,88%

Tail rotation speed (rad/sec)	42,94	6,22

5.8 Conclusions

All the launches showed a variable behaviour, and were evenly distributed among the identified categories. The drag affected the impact speed of the seed; indeed meanwhile previous studies measured an initial average velocity of 2±4 m s^{-1}, the average speed recorded during the landing was 1,4±0,3 m s^{-1}.
The angular velocity had a great influence in the impact dynamic causing both speed revolution and tail rotation. Tail rotation speed or seeds revolution movement were found of a good value of approximately 50 m s^{-1}: this indicates that the initial angular velocity affected the dynamic of the landing seed after the impact, ultimately resulting in revolution or rebound effects. If the aim of the seed is to penetrate or to catch a support, the ability to rebound and rotate on the soil surface is an undoubted advantage for an object that ends with an heavy and sharp spike (i.e. carpel). The initial angular speed influences both the penetrating chance and the distance covered by each seed once landed. This speed is able to increase the force of the carpel directly by turning the seed into the soil as the movement of a screw. However, if the position of the impact it is not favourable to the penetration, it can increase the distance travelled by the seed. From the position of impact every seed can travel from few centimetres to up to several centimetres, and this parameter it is also influenced by soil composition (i.e. pure talcum, ½ talcum powder and ½ perlite). In fact the elastic shape of the seeds can facilitate rebound performances if hard surface or obstacles are impacted.

The initial high angular velocity can influence the dynamic of the launch mostly when the seed falls to the side, increasing the distance covered, and due to its shape maximizing the contact between the carpel and the soil when the seed is twisting. Anyway it can work positively if the seed impacts the soil with all its conferences in contact with the terrain (category 3): it would then work as a screw to fix the spike into the ground, and for the same motivations this can improve the force of penetration when the seed buries itself directly into the ground.

This rotation speed should be analysed more in detail in the future and could improve the distance of the rolling seeds in several conditions, such as strong wind, inclined terrains or when an impact with very hard object happens (i.e. stones). Preliminary analysis performed on seeds that encountered an object during the flight showed a simultaneous reduction of the speed and of the chance to penetrate directly into the soil; this can explain why *Erodium cicutarium* plants prefer to launch their seed in height and not through a direct trajectory that increases the travelling distance: this reduced the likelihood of contacts with neighbouring plants. These results confirm the adaptability and the flexible characteristics of this seed: its launch dynamic revealed a good probability to directly penetrate into the ground or to be in a very advantageous position to penetrate the soil after the first coil (i.e. almost 1/3 of all cases analysed).

6. Modeling of the self-burial strategies

6.1 Introduction

The burrowing capabilities of the *E. circutarium* are enabled by its particular geometrical configuration, accessory structures, and the tissue structure of awn (Fig. 41). The cyclic humidity variations, occurring during the day and overnight, in the ground cause the awn to wind and unwind. This motion, combined with the carpel geometry and accessory structures, such as carpel barbs, awn hairs, and an inactive awn region, allow the seed to penetrate and drill into the ground. The study of this WP is focused on the analysis of self-burial strategies of *Erodium* seed by means of literature search and numerical modelling. Modelling was performed by means of finite element (FE) analysis through a commercial code. In particular, since FE method is a structural based analysis, special attention was paid to the tissue structure of awn. In the following, awn structure and its winding mechanism, seed leverage and positioning on the ground and the carpel penetration into the substrate are investigated. The investigation of these key aspects is the first step toward a more complex model that is able to describe awn kinematics on the ground and seed penetration into the soil.

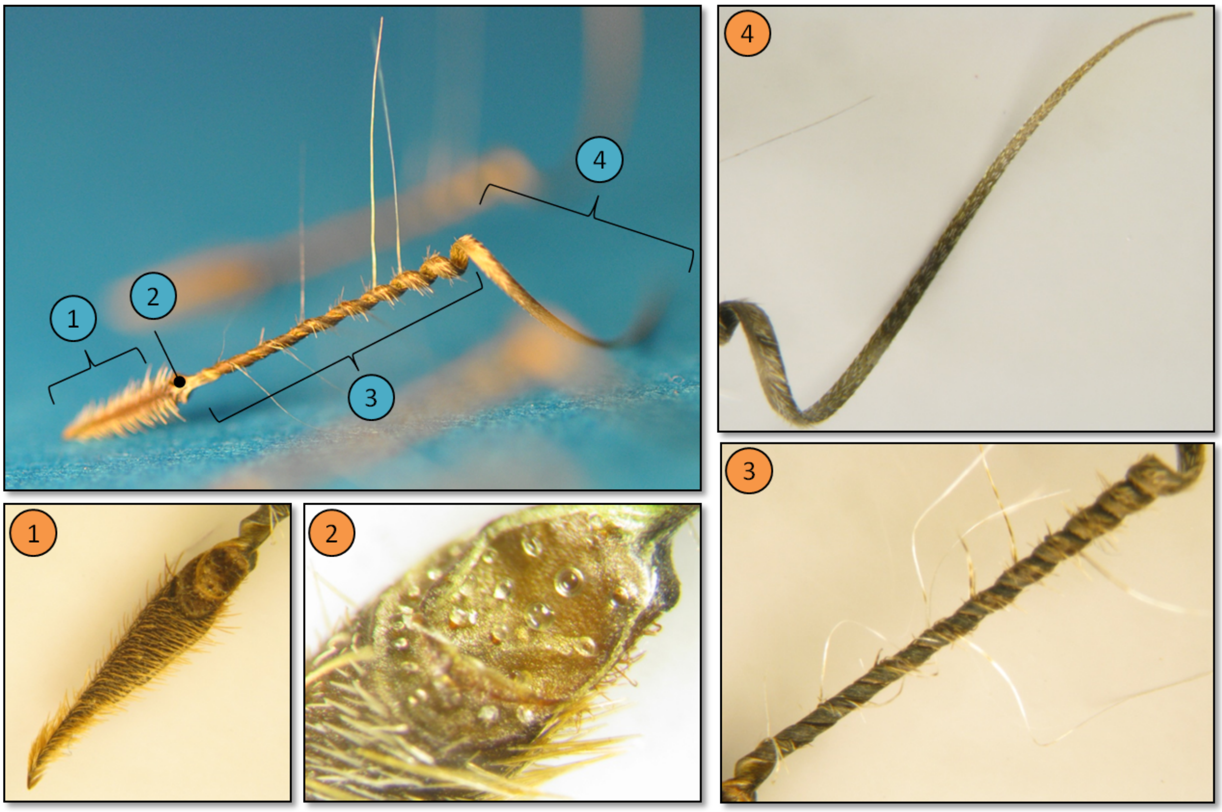

Fig. 41 *Erodium cicutarium* seed and its accessory structures: 1) carpel with sharp tip and barbs; 2) the carpel-awn region with two symmetrical cavities; 3) hygroscopic, coiling, region of the awn with long and short hairs; 4) awn tail, not hygroscopic region of the awn with short hairs.

6.2 Awn winding and unwinding

The hygroscopic tail is the actuating part of the seed for the penetration into the soil. The seed kinematics depends on awn winding and unwinding movements. A properly anchored awn can transmit to the seed the rotary and translational movements, which are fundamental for the seed to penetrate the soil. While the *anchorage* may be provided by the hairs and the not-coiling-region of awn, the winding and unwinding are resulting from the particular awn tissue structure.

6.2.1 The awn structure and function

The *Erodium* awn consists of two layers: the inner and thicker one, facing towards the inside of the coil (i.e., the ventral side of the coiled awn), and the outer one, that faces outwards from the coil (i.e., on the dorsal side of the coiled awn). When the layers were experimentally separated, it was observed that the inner layer coils more tightly than the complete awn, whereas the outer layer coils only slightly towards the inner layer. Also the longitudinal strips of the inner layer, as well as the mechanically separated cells, have been found to coil (Abraham et al. 2012). Thus the macroscopic hygroscopic behaviour of the awn is believed to be the result of the cooperation of the inner-layer cells capable to coil hygroscopically (Fig.42). It has been found by Abraham *et al.* (2012) that the cellulose microfibrils are wound around the cell in a very tight tilted helix (Fig.). It seems that the cells from the inner layer coil when they dry, while the cell wall matrix contracts against the cellulose microfibril scaffold.

It has been noticed that, the outer layer has a function of increasing the rigidity of the awn and does not play a role in the coiling mechanism, as the inner layer can coil by itself even tightly than the entire awn (Abraham et al. 2012). That means that the coiling mechanism is not simply described by the classical *bilayer structure effect* (based on the different interface strain of two layers with different expansion properties). Indeed, the hygroscopic coiling originates from specialized cells, which can coil because of the cellulose microfibrils arrangement in the tilted helix. The stable configuration of each one can be totally described by the tilt angle and the desiccation factor (Aharoni et al. 2012). Interestingly, the tilt angle of the cells is larger on the proximal part than on the distal part of the hygroscopic region of the awn (Fig. 43).

Relevant aspects for the awn actuation are: i) macrostructure - 3D shape of the awn (initial and final configurations) as an helical structure; ii) microstructure - microfibers arrangement of the awn cells in tilted helix; iii) from microstructure to macrostructure - parallel linear arrangement of the cells in the awn; iv) desiccation factor. Elucidating the biomechanical principles involved in the considered aspects can support the development of highly innovative actuation solutions; modelling activities, in turn, can effectively support such an investigation. The next section is dedicated to the State of the Art in modelling with the aim to extract the relevant principles and characteristics for the understanding of awn properties by means of model simulations. It is worth remarking that no description is provided in literature as regards the transition region between the coiling region and the distal, uncoiled one.

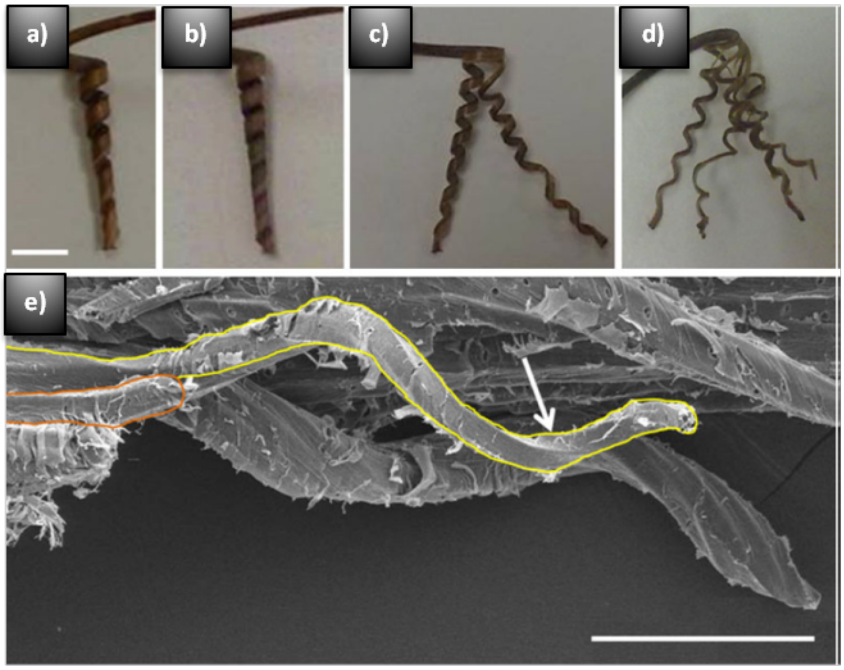

Fig. 42 Cooperative cell spiraling creates the macroscopic coil. a) coiling region of the awn (5 coils); b) inner layer of the awn coiled tightly than in point a) (7-8 coils); c) and d) the inner layer split into once and twice still coils to about same extent as the complete inner layer; e) a single coiled cell and a group of coiling cells in background (made by scanning electron micrograph of the inner layer). Scale bars (a-d) 5mm and e) 100 μm. From Abraham *et al.* 2012.

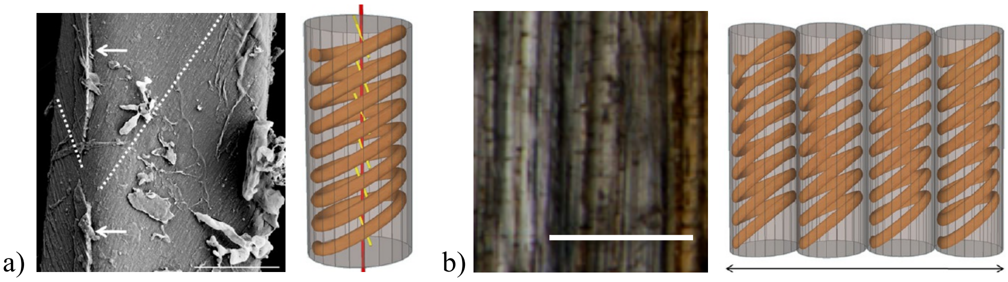

Fig. 43 a) Cryo-scanning electron image showing the change in microfibril angle in a single cell, marked by a broken line, and a schematic showing the arrangement of cellulose microfobril in a tilted helix (scale bar - 5 μm); b) longitudinal section of the inner layer showing the cells' alignment with the length of the awn (scale bar - 100 μm) and a scheme illustrating the cell arrangement and the identical cell polarity in the inner layer of the awn at the coiling region. From Abraham *et al.,* 2012.

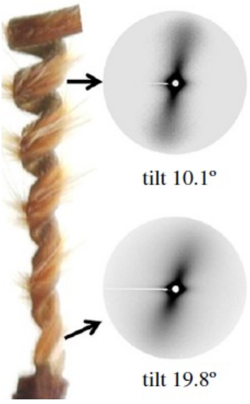

Figure 44. The cellulose microfibrils organization in the cell walls of the coiling cells: small-angle X-ray scattering (SAXS) pattern of a vertical sample from the inner layer of the awn, measured at the top and bottom parts of the coiling region. The tighter coil in the bottom part shows a larger SAXS tilt. From Abraham *et al.* 2012.

6.2.2 Models for coiling in literature

The computer modelling of the awn can be useful to better understand both the material properties and geometrical parameters of the awn, as well as the kinematics of the seed. The helical structure is the core parameter of the *Erodium* awn and understanding its generation and kinematics is a first step to perform.

Evangelista *et al.* (2011) have developed a kinematic model (Fig.45) of the hygroscopic region of the awn. In order to compute shape variations, a desiccation factor was considered. Beam elements with rectangular section were used. Initial awn shape was modelled as a logarithmical spiral (Fig. 45). Indeed, logarithmic spirals are very common in natural structures and living beings, as they are constructed by keeping the spiral angle constant (Fig. 45) (Evangelista et al. 2011). The awn shape was completely defined by four parameters: maximum awn diameter, spiral angle, number of terns and awn height (Fig. 45) (Table 11). A desiccation, x_d, factor ranging from 0 to 1 was used to simulate hydration and desiccation. This factor was used as a premultiplier for the curvature k(s) in the system (1) from the dry shape:

$$\begin{aligned} \mathbf{u}' &= k\mathbf{p} \\ \mathbf{p}' &= -k\mathbf{u} + \tau\mathbf{b} \quad ,(1) \\ \mathbf{b}' &= -\tau\mathbf{p} \end{aligned}$$

where $\mathbf{u}$ is the tangential vector of the awn backbone, calculated as the derivative of position vector,
$\mathbf{r}(t)$ with respect to the arc length, s, $\mathbf{u}'$ is its derivative,
$\mathbf{p}$ is the unit principal normal vector, defined as $\mathbf{p} = \mathbf{u}'/k$, $\mathbf{p}'$ is its derivative,
$\mathbf{b}$ is the unit binormal vector, defined as $\mathbf{b} = \mathbf{up}$, $\mathbf{b}'$ is its derivative,
k is the curvature, calculated is $k(s) = |\mathbf{u}'(s)|$,
τ is the torsion, calculated as $\tau(s) = -\mathbf{p}(s)\cdot\mathbf{b}'(s)$.

The curvature was then integrated so as to determine the current shape of the awn. The model was validated by comparing the predicted awn geometry with that observed with the time-lapse video.

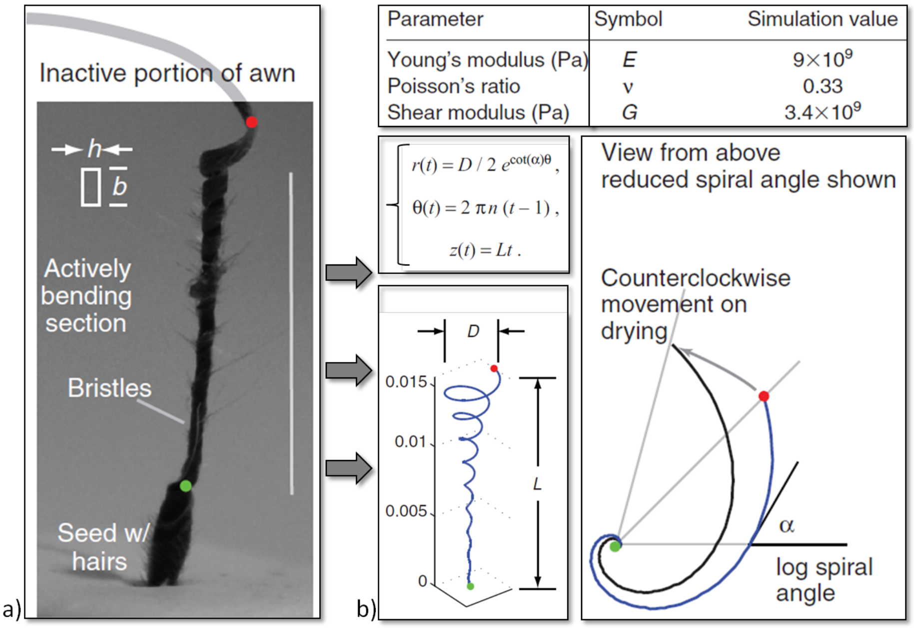

Parameter	Symbol	Simulation value
Young's modulus (Pa)	E	9×10^9
Poisson's ratio	ν	0.33
Shear modulus (Pa)	G	3.4×10^9

$$\begin{cases} r(t) = D/2\, e^{\cot(\alpha)\theta}, \\ \theta(t) = 2\,\pi n\,(t-1), \\ z(t) = Lt. \end{cases}$$

Fig. 45. *E. cicutarium* awn model. The hygroscopically active awn region is modeled as logarithmical spiral. Model shape parameters are the maximum diameter *D*, height *L*, number of turns *n*, spiral angle α, and section width *b* and thickness *h*. Model material properties are Young's modulus *E*, Poisson's ratio *α*, shear modulus *G*. The proximal (seed) end of the active region is shown by green dot and the distal end of the active region is shown by red dot. Scale bar, 15 mm. The mathematical representation of the logarithmic curve has parametrical form and the shape is defined by the parameter t=[0,1]. This model was developed in Matlab (The MathWorks, Natick, MA, USA). From Evangelista *et al.,* 2011.

Table 11. Awn shape and section properties measured from *E. cicutarium* awns. From Evangelista *et al.* 2011.

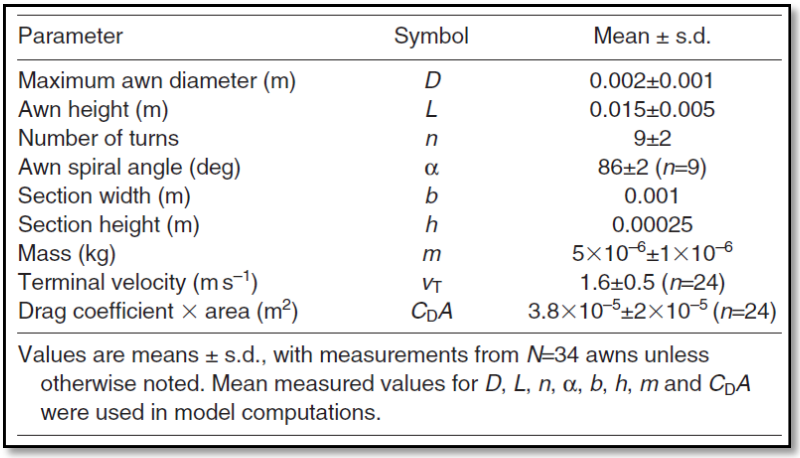

Parameter	Symbol	Mean ± s.d.
Maximum awn diameter (m)	D	0.002±0.001
Awn height (m)	L	0.015±0.005
Number of turns	n	9±2
Awn spiral angle (deg)	α	86±2 (n=9)
Section width (m)	b	0.001
Section height (m)	h	0.00025
Mass (kg)	m	$5\times10^{-6}\pm1\times10^{-6}$
Terminal velocity (m s^{-1})	v_T	1.6±0.5 (n=24)
Drag coefficient × area (m^2)	C_DA	$3.8\times10^{-5}\pm2\times10^{-5}$ (n=24)

Values are means ± s.d., with measurements from N=34 awns unless otherwise noted. Mean measured values for D, L, n, α, b, h, m and C_DA were used in model computations.

Eberle *et al.* (2009) have developed a 3D FE model of tendril coiling by exploiting the commercial solver ANSYS 11.0 (ANSYS, Inc. Cannonsburg, PA, USA) (Eberle et al. 2009). Special beam elements ("Beam188" 3D linear finite-strain beam element with six degree of freedom per node that allows the use of user-input cross section and the implementation of a lengthwise tapper) subjected to thermal expansion were used to mimic the strain caused growth. The coefficient of thermal expansion, CTE, was used as a growth factor which dictates a certain growth rate. By applying a temperature load as the growth stimulus and a CTE gradient across the circular cross-section of the tapered cylinder as the differential response to the stimulus, differential dorsal and ventral elongations were achieved (Fig.46). The growth stimulus was considered to be linear from proximal to distal ends of the tendril and was simulated as the temperature gradient.

The dimension of a true tendril was used (tapered cylinder of 10 cm length, proximal diameter of 0.30 mm, distal diameter of 0.15 mm and 7 cm length, proximal-end diameter of 0.52 mm, distal-end diameter of 0.40 mm for *Luffa cylindrical* and *Adenia lobata* respectively). A force along with a small rotation (0.05 rad) was applied to the small end of the tendril in order to break symmetry, while the proximal end of the tendril was fixed. The elastic modulus was of 33 MPa.

The driving parameters of this model are the temperature gradient along the tendril axis and the thermal expansion coefficients (CTE) on the ventral and dorsal side (being interpolated in between). The calculation of the temperature gradient was based on the strain measurement on the dorsal side of a true tendril. The total dorsal strain measured was simulated by temperature function $T(x) = 43x+29$, where x is the abscissa along the longitudinal tendril axis, and dorsal CTE = 10^{-2} K^{-1}. While the dorsal α was a fixed value, the CTE dorsal to ventral ratio was changed. It was found that to generate geometry similar to the true tendril a CTE dorsal to ventral ratio of 10:1 should be used for this type of model.

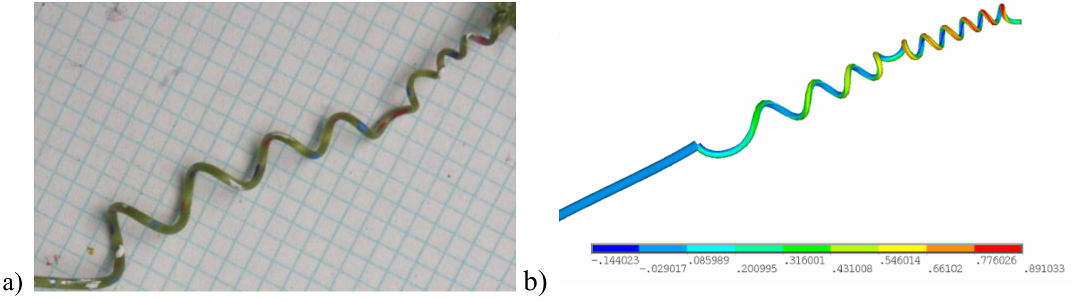

Fig. 46 a) Picture of the coiled tendril. Coloured markings were first applied as dashed line to the tendril in its uncoiled configuration. (10*10 boxes is a 1 inch square grid.) From Eberle *et al.* (2009).

Sawa *et al.* (2011) have developed model to predict the nematic elastomers (NEs) coiling into the twist nematic elastomers (TNEs). This behaviour can be described as the evolution of a flat bar into helicoids which then jumps to ribbons while temperature changes (Fig. 47) (Teresi et al. 2012). The theory of finite elasticity with distortions was used to model the behaviour of NEs into TNEs by using the software COMSOL Multiphysics (COMSOL Inc): 3D incompressible non-linear elasticity with large distortions was exploited. The model is in agreement with the experimental data. The stimulus for geometry change is again given by a temperature, while the definition of distortions allows the structure to bend and twist with extremely large changes in configuration. Such a model, originally developed for a different problem, can be useful for modelling the formation of the considered awn shape.

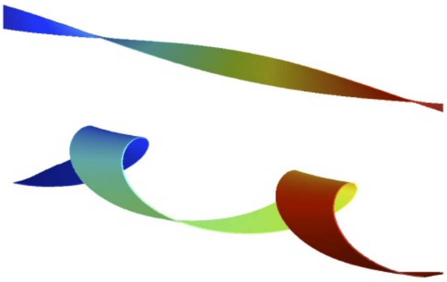

Fig. 47 A thin bar of TNEs may assume different shapes according to its temperature; the transition from a flat shape (not shown) to an helicoid (top) is quite smooth; beyond a threshold temperature, the film buckles to a ribbon (bottom). From Teresi and Varano (2012).

Tab. 12. What can be learned from the existing models.

	Reference	Model	Insights for the awn model	lacking aspects
1	Evangelista et al. (2012)	awn curvature during unwinding	logarithmic shape	uses 1D rod
2	Eberle et al. (2009)	FEM to model the tendril coiling by using temperature gradient as actuation	use of the thermal coefficient of expansion to simulate the dimensional changes; use of temperature as the desiccation factor	the deformation is based on bilayer principle
3	work of L. Teresi in Sawa et al. (2011)	FEM with finite elasticity with distortions to predict nematic elastomers coiling	use of temperature as a desiccation factor; use of the specific form of coefficient of expansion to guide the distortion of structure	uses 2D sheet

The first model suitably describes a backbone curve for the awn, mainly based on corresponding helix parameters. Such a backbone can be used as a starting element for the construction of more realistic, 3D awn structures. Such an extension might not be straightforward, since steric (i.e., contact) constraints must be accounted for when sweeping awn cross-section along a given backbone.

The tissue deformation modelled by a temperature gradient and an applied function of the thermal expansion coefficient is a simple and efficient way to model coiling and uncoiling of the structure. However the proposed models do not take into account the hierarchical structure of the awn. On contrary it resembles the characteristics of bilayer structures such as conifer cones and tendrils.

Hereafter we propose a modelling approach that incorporates some features of the cited examples (Tab. 12) and which is consistent with the microscopic constituents of the awn tissue.

6.3 Understanding the *Erodim c.* awn by modelling

6.3.1 *Physical models*

Hereafter we explore a mechanical principle of the coiling process of *Erodium* awn, based on the use of an elastic rubber band, in order to develop preliminary physical demonstrators of an artificial counterpart of the awn. Despite the fact that such an activity was not originally foreseen in the project workplan, it was added in order to better understand the winding mechanism in the awn.

6.3.2 Bilayer principle

One of the approaches to make the band coil is to use a classical bilayer principle (Gerbode et al. 2012), which is characterized by a different strain at the interface between the two layers. To try this, a sealing silicon layer was put onto a pretensioned rubber band (Fig. 48a). Some artificial plastic hairs were applied on the silicon layer in order to investigate their movement during the coiling (see section “movement of the awn hairs” for deeper explanation). After the silicon layer was fully cured the released band coiled with the coils of the same diameter Fig. 48b). The coils irregularities were due to the unequal silicon coverage along the band. In this case the bending was achieved by an axial asymmetric contraction, caused by the fact that the rubber band tends to contracts more than the silicon on it. To achieve different diameters coils the silicon layer was put on the band using different band pretension. More tight coils correspond to the higher pretension of the band (48c).

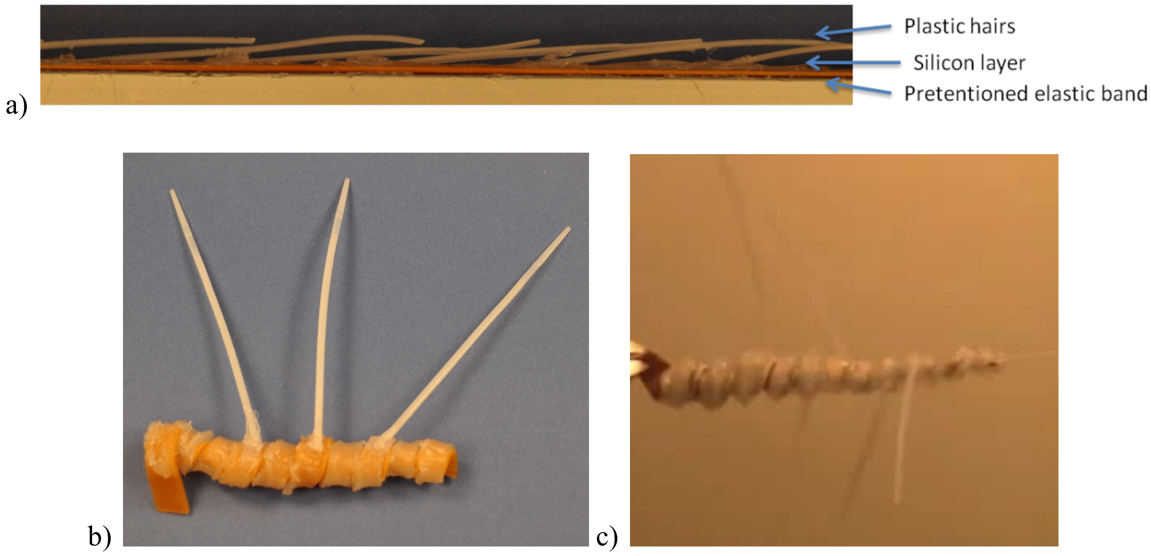

Fig. 48 Physical model of *Erodium* awn built by using a bilayer principle: a) pretensioned elastic band with a curing silicon layer on it and artificial plastic hairs; b) coiled configuration of released band with silicon and plastic hairs, coils have the same diameter as the silicon was put on the uniformly pretensioned band; c) coiled configuration of released band with silicon and plastic hairs, coils have different diameters as the silicon was put on differently pretensioned band – the tighter coils correspond to the higher pretention of the band.

6.4 ‘*Erodium*’ principle

It was proposed by Abraham et al. (2012) that the particular cell arrangement with tilted fibers of cellulose, shown in 42b, is the key of the coiling mechanism of *Erodium* awn. The idea is that the microfibers shrink less than the surrounding matrix, thus inducing local constraints on deformation. From a macroscopic viewpoint such arrangement gives a preferential direction of strain that would ‘guide’ structural deformation during the volume change (Fig. 49). In particular, the structure would have the oblique direction of strain with different angles on frontal side with respect to the backward side in accordance with the orientation of microfibril tilted helixes.

The awn winding was filmed under the optical microscope to better visualize the morphological changes. It was observed the emergence of some oblique creases on the ventral side of the awn just the instant before the formation of curvature (Fig. 50). It is possible that the creases are formed as a result of preferential strain deformation produced by a cooperative winding of the cells. To test the soundness of this hypothesis a correlation study between inclination of creases and coil diameter was performed on one example of *Erodium* awn.

The crease phenomenon was further investigated to understand if the oblique angle was constant or not along the awn height. The Erodium awn was divided into six coils and on each coil the oblique crease angle was measured (Fig. 51). The oblique crease angle with respect to the distance from the seed is reported in the plot of Fig. 52. The angle decreases with increasing distance. Also it can be noticed from the Fig. 51 that the coil diameter increases with increasing distance from the seed. It is possible that the coil diameter depends on the oblique crease angle. To test this hypothesis the physical model was built by inducing oblique strains on the elastic band.

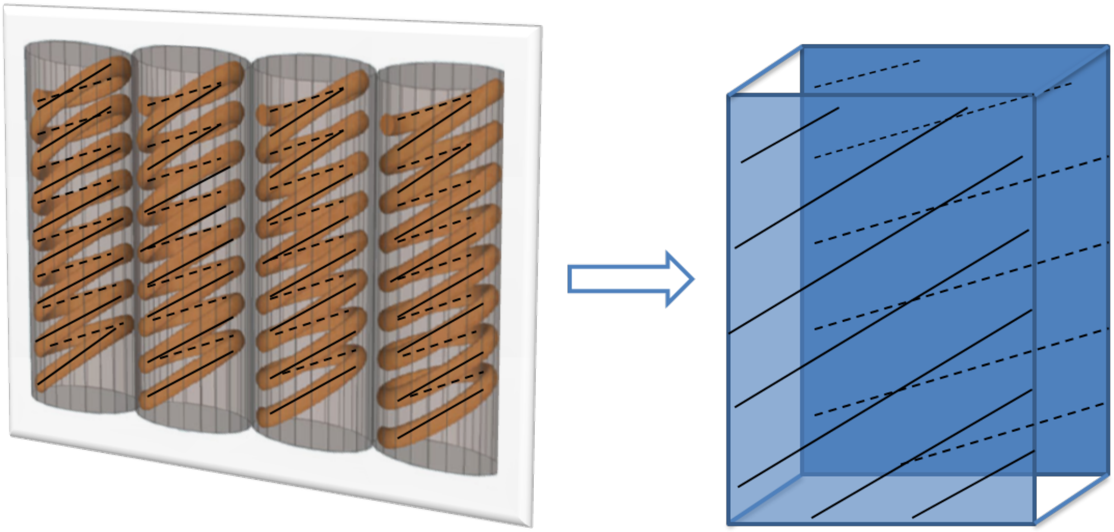

Fig. 49. Schematic representation of the principal strain directions emerging from the arrangement of cells and their cellulose microfibers in the *Erodium* awn. These strain lines determine the deformation of the structure during the volume change.

Fig. 50 Pictures of the ventral side of awn during the winding. The oblique creases during the winding can be seen (some of them are indicated by white arrows). The angle of creases is indicated in white and is approximately 135° in these pictures. The orange squares are of 1 mm width.

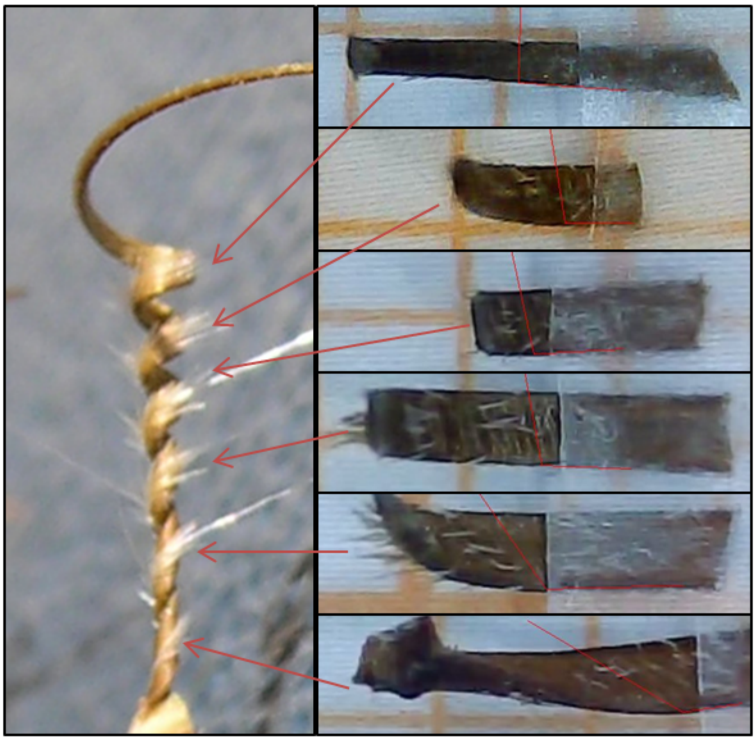

Fig. 51 *Erodium* wind awn and observation of the oblique creases on each coil. The oblique crease angles are indicated by red lines.

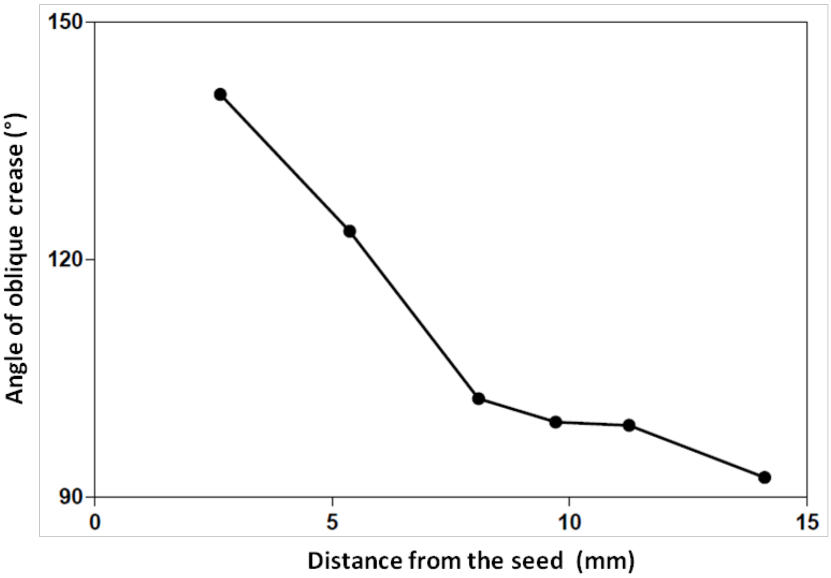

Fig. 52 Plot of the oblique-crease angle with respect to the distance on the awn from the seed. The angles were recovered from the images of Figure 51.

6.4.1 Oblique-strain principle

To better understand the origin of curvature in *Erodium* awn, we tested the hypothesis of oblique strain principle by using a physical model composed by an elastic rubber band with the oblique silicon strips distributed onto it. The oblique-strain principle of deformation is based on the inhomogeneous shrinkage/swelling of composite material due to the fiber arrangement inside the matrix.

The elastic rubber band was initially pretensioned, before putting the silicon on it, as in previous case. The strips of sealing silicon were put obliquely (approximately with the angle of 45° to have some insights on the induced deformation) and equally spaced on the pretensioned band (Fig. 53a). The band coiled when it was not tensioned any more, after the silicon was cured. Coils were of the same diameter.

Another layer of the silicon strips was added on the opposite side of the pretensioned band to see the effect on the deformation of the band. The pretension was the same as in the previous case, while the oblique angle was halved with respect to the other side. The resulting coils almost disappeared. Although, the angle of newly added silicon strips was different, the silicon strips on one side compensated the deformation induced by the silicon strips on the other side. Thus it was decided to add the silicon strips only on one side of the band in the next experiment in order to preserve coiling behaviour.

In order to achieve coils with different diameter a second band was used. In this case, the silicon strips were put with different oblique angles (approximately from 30° to 90°) (Fig. 53b). The resulting coils with smaller diameter correspond to the strips with smaller oblique angle.

It is worth to notice that the oblique creases on the real model result from the stress-induced strains, while the oblique silicon strips at band produce stress which in turn induces a strain. However, corresponding findings are consistent. The oblique creases were observed on the ventral side of the coils while the oblique silicon strips were put on the dorsal side of the coil. Thus the oblique creases are induced by the compression oblique stresses perpendicular to them on the ventral side, while the oblique silicon strips induce traction oblique stresses perpendicular to them on the dorsal side, so that the two configurations are consistent (Fig. 54).

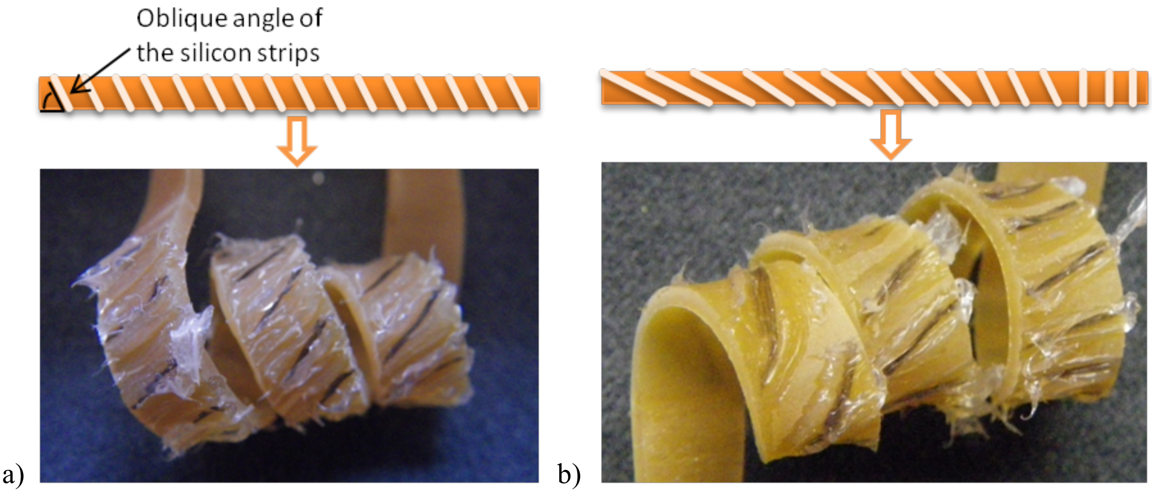

Fig. 53 Physical model of *Erodium* awn build by oblique-strain principle: the schematic representation of the silicon strips applied to the elastic band and the picture of resulted coiling band. a) The silicon strips were put with the same oblique angle on the pretensioned elastic band, the resulting coils are of same diameter; b) the silicon strips were put with different oblique angles, the resulting coils are of smaller diameter for the strips with smaller oblique angle.

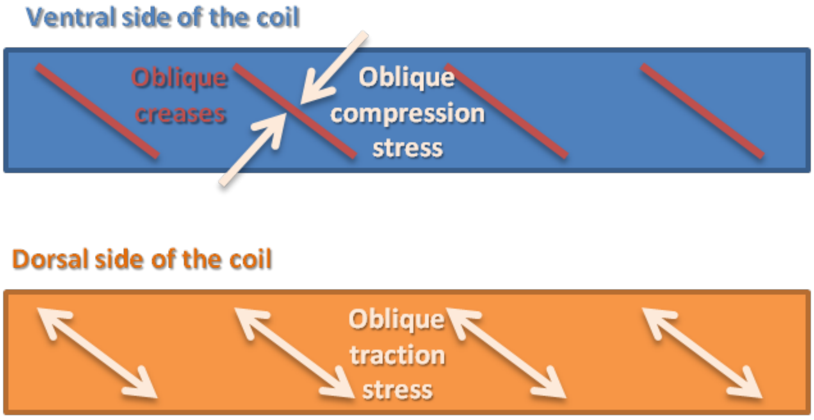

Fig. 54. Schematic representation of the oblique stress direction for the observed oblique creases and for the physical model of elastic band with silicon strips.

6.5 FE modelling

6.5.1 Bilayer and oblique-strain modelling principle

The objective of this section is to show how the two principles considered above (i.e., the bilayer and the oblique-strain modelling principle) may be introduced into a simple FE model. The idea is to shrink the structure by reducing the temperature, and introduce some changes in geometrical configuration by unequal (i.e. not isotropic) shrinkage of structure. The volumetric changes can be obtained by the variation of temperature (i.e. the solid objects generally swell if the temperature increase and shrink if the temperature decrease), while the desiccation factor can be given by the coefficient of temperature expansion (CTE).

Let for simplicity take a rectangular band with the properties of the silicon material and with CTE equal to 10^{-3} K^{-1}, chosen so as to get relevant bending effect to be qualitatively analysed. When a temperature gradient is applied between two faces the band bents toward the lowest temperature (Fig. 55a), because an asymmetrical longitudinal volumetric change occurs between ventral and dorsal sides. No twisting occurs, in this case, only bending. The structure can twist (Fig. 55b) in case the isotropic CTE is replaced with the anisotropic CTE described by matrix with components different from zero corresponding to the height - width direction (i.e., the x-z direction in the model). In this case, the structure mostly undergoes twisting and the temperature gradient enables the asymmetrical deformation between ventral and dorsal sides along the oblique axis x-z. A mixed deformation of bending and twisting can be obtained, by adding the component along height (i.e., the z component) into the CTE matrix (Fig. 55c). These observations, despite associated simplifications, allow for a comprehension of the induced bending/twisting on the structure. Larger deformations could be modelled by more elaborate modelling approaches (essentially based on finite elasticity), which nonetheless are outside the scope of the present document.

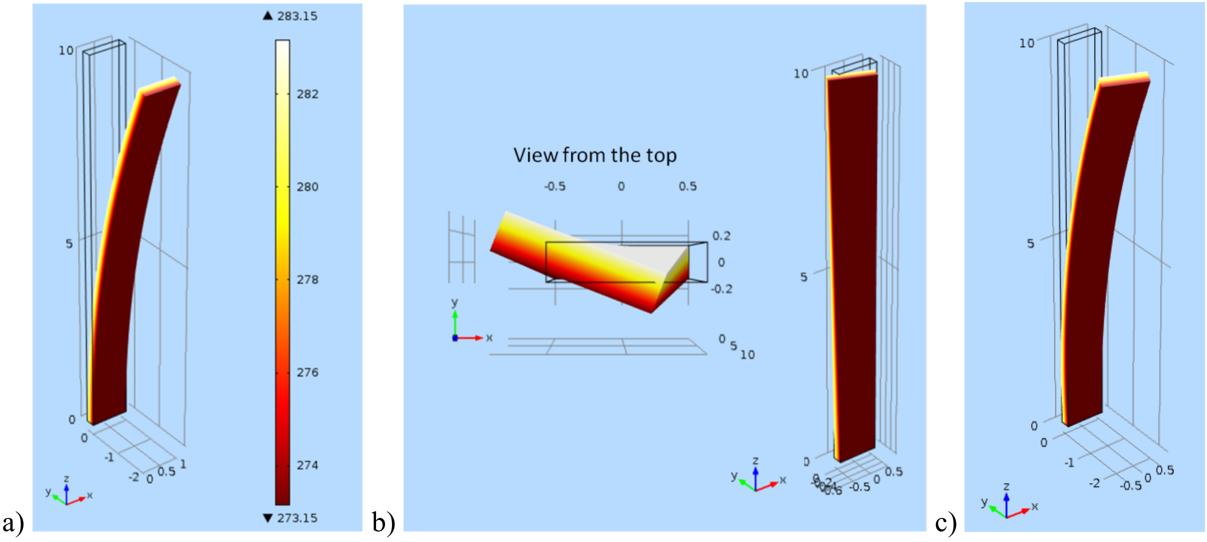

Fig. 55 Modelling the structural deformation by a) bilayer principle, b) oblique-strain principle, c) mist concept. The model was built in Comsol Multiphysica 4.3 by using Solid Mechanics and Thermal Stress modules and solving the stationary problem. The combined use of these modules allows the calculation of stresses and strains produced by thermal expansion/shrinking. Indicated dimensions of structure are in mm. The elastic isotropic material with silicon properties was chosen from build-in Comsol library. The colours on the structure indicate the temperature gradient by which the asymmetrical volumetric changes were obtained, see coloured bar in the a) image for the temperature values in K. The temperature gradient of 10° was applied between two faces of band. The initial temperature of the un-stressed configuration was 293.15 K. The initial configuration is shown on the images by continuous black lines.

6.5.2 Geometry of the awn

The geometry of deforming structure is very important in the deformation process. The *Erodium* awn has 2 stable geometrical configurations (Fig. 56): one is the unwind configuration and second is the winded structure. We consider the unwind configuration as initial, from modelling viewpoint, because it corresponds to the formation of the awn on the plant. We consider the winded geometry as a final configuration, because it is a result of the deformation of the unwind one after the seed has been detached from the plant.

By following Evangelista *et al.* (2011) the final configuration can be constructed by giving to the backbone of awn a logarithmic shape. However, a special attention should be paid to the geometrical parameter, such as spiral angle, to avoid the reversing and overlapping of the turns. For example, in Fig. 57a a final configuration of awn coiling region, constructed by using parameters reported in Evangelista *et al.* (2011) is shown. In this geometry the coils of proximal part are deformed differently from *Erodium* awn coils. By changing the helix angle from 86° to 88° the coils became more regular and similar to the real awn coils (Fig. 57b) and by increasing the angle again till 89° the structure become dissimilar from the awn (Fig. 57b). It can be noticed from Fig. 55a that the initial configuration of *Erodium* awn is not a straight band but a slightly curved ribbon. This curvature can be approximately represented by a logarithmic helix similarly to the final configuration, described by one turn or by partial (incomplete) turn. Also the maximum diameter of the helix should be changed to a lower value.

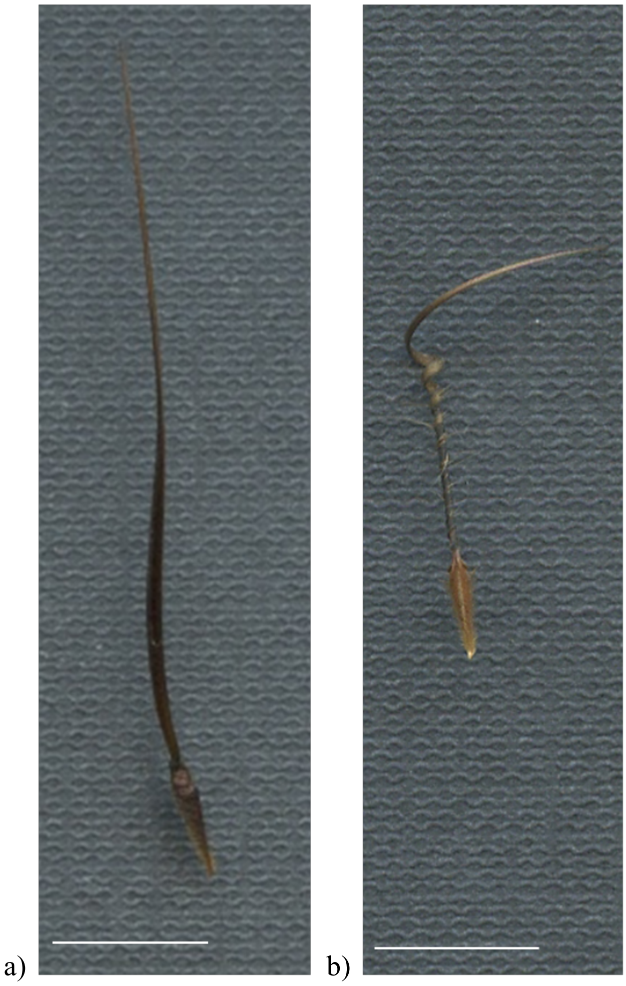

Fig. 56 a) Whet awn corresponding to the initial configuration and b) dry awn corresponding to the final configurations (scale bar – 1 cm).

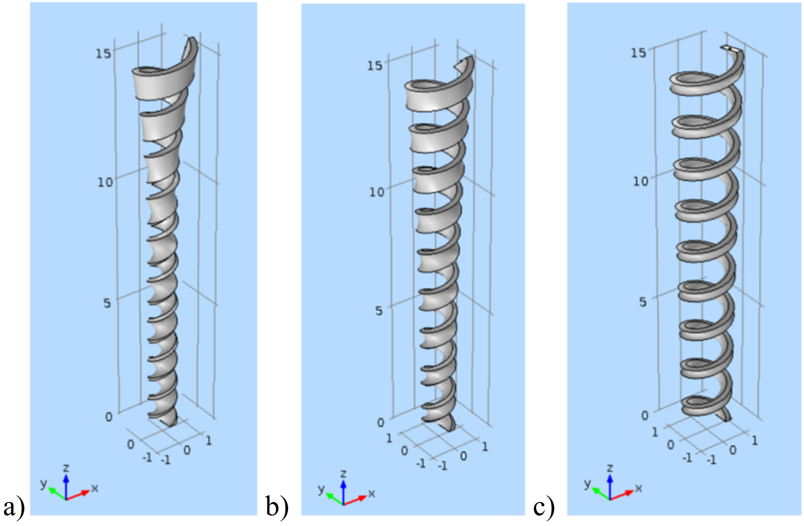

Fig. 57 3D geometry of the *Erodium* described by a backbone with logarithmic shape a) by using the parameters of Evangelista *et al.* (2011), the parameters used can be also seen in Fig. 45 and Tab. 11 (see section 6.2.2); b) by using the parameters of Evangelista et al., 2011 and changing the spiral angle from 86° to 88.27°; c) by using the parameters of Evangelista et al., 2011 and changing the spiral angle from 86° to 89.43°. This geometry becomes more sensitive to the variations of log-spiral angle when it approaches 90°. The backbone was positioned into the centre of coiling layer. The geometry was built in Comsol Multiphysics 4.3. The dimensions of awn are indicated in the plots in mm.

6.5.3 Winding of the awn

Here we are using FE modelling with attempt to implement the oblique-strain principles on the awn geometry, by specifically addressing the suitability of the starting (beam) geometry for describing the considered coiling process. The model was build in Comsol Multiphysics 4.3 with the initial configuration of unwind awn and geometrical parameters in Fig. 58a. As previously, Solid Mechanics and Thermal Stress modules were used to solve stationary problem. The constitutive material was considered to be linear-elastic with parameters taken from Evangelista *et al.* (2011) (Fig.44). The anisotropic CTE was chosen with component $CTE_{\mathbf{tz}}= 10^{-3}\ K^{-1}$ (where **z** is vertical tangential to surface vector and **t** is perpendicular to **z** and tangential to surface vector) in order to get appreciable result, other components were set to zero. By applying temperature gradient (i.e., temperature gradient was of 10°) between ventral and dorsal sides of awn geometry a twist deformation was obtained (Fig. 58b).

Some geometrical features were varied in order to evaluate the deformation sensibility. By changing the logarithmic angle the twist deformation did not changed significantly. The geometry with tilted logarithmic helix was also evaluated. No appreciable differences have been found between the deformation of tilted-logarithmic-helix and regular-logarithmic-helix.

The proposed model aimed at assessing the suitability of the adopted awn geometry for describing deformations induced by the oblique-strain principle. To produce large bending and coiling in order to model the awn kinematics, more complex FE techniques suitable for larger distortions should be implemented, as mentioned above. An accurate investigation of the relation between coil diameter and stress orientation can only be tested in such a more complex modelling environment (this is outside the present scope).

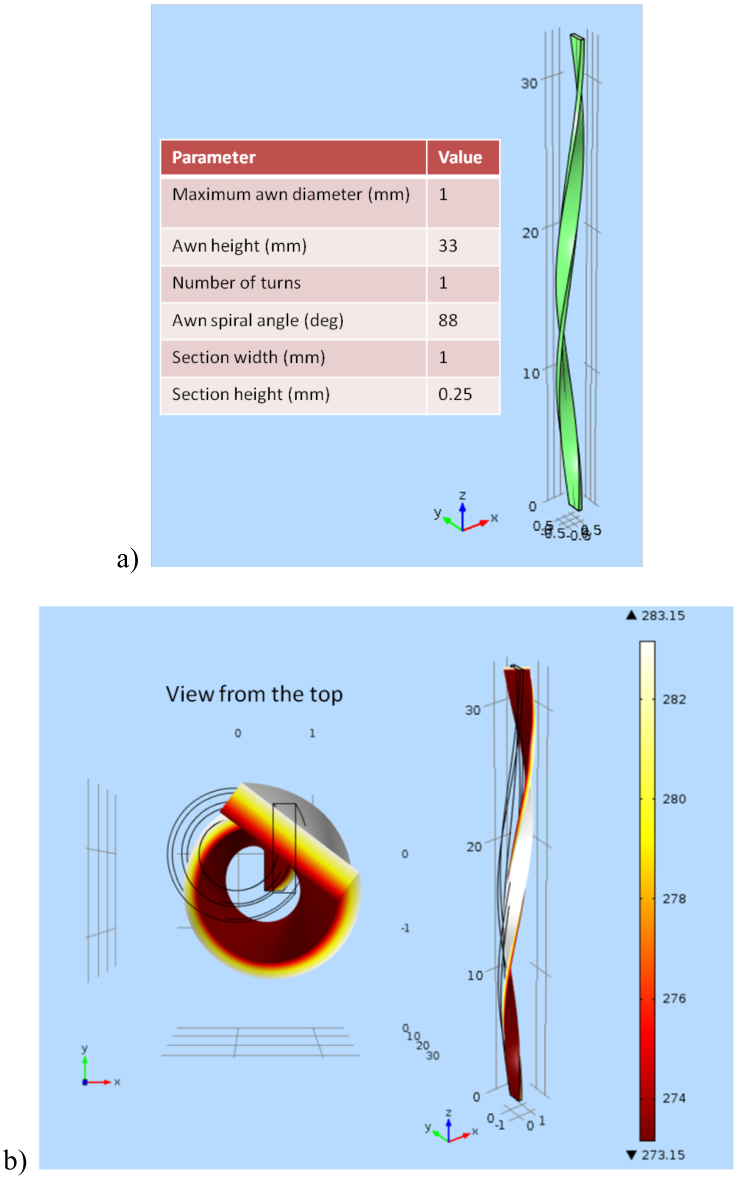

Parameter	Value
Maximum awn diameter (mm)	1
Awn height (mm)	33
Number of turns	1
Awn spiral angle (deg)	88
Section width (mm)	1
Section height (mm)	0.25

Fig. 58. Model of the oblique-strain principle applied to the geometry of unwind *Erodium* awn. a) The geometry plot of unwind *Erodium* awn constructed by a logarithmic helix backbone, the parameters used are reported in the enclosed table. b) Plot of the awn-geometry deformation that was induced by applying oblique-strain principle. The coloured bar indicates temperature values in K. Reported dimensions of structure are in mm. The initial temperature of the un-stressed configuration was 293.15 K. The initial configuration is shown on the images by continues black lines.

6.6 Seed displacement on the ground and importance of the accessory structures

In this section the seed positioning and leverage are analysed by means of numerical modelling, in order to preliminarily evaluate the influence of gravity and awn geometry and material properties on it.

6.6.1 Seed positioning on the ground

Seed penetration into soil is correlated to the accessory structures, which in turn also affect seed positioning on the ground. Indeed the studies by Stamp (1984) have shown that the awn tail and the awn hairs help the seed to penetrate the soil. Moreover, the accessory structures

influence the movement and position of the seed on the ground. The seed penetration depends on the forward movement, on the blockage mechanism of the backward movement (i.e., anchorage), and on seed inclination. These aspects are further discussed below.
The seed forward movement depends on the awn unwinding. Its mean velocity can be approximately estimated as:

$$\frac{L_{unwind}-L_{wind}}{t_{cycle}} = V_{seed} \ , \tag{2}$$

where L_{unwind} is the length of hygroscopic region of unwind awn,
L_{wind} is the length of hygroscopic region of wind awn,
t_{cycle} is time of one unwinding cycle,
V_{seed} is the forward velocity of the seed.

By this estimation the seed forward mean velocity is nearly 1 mm/min in unimpeded conditions.
The seed leverage is important for the penetration (Stamp 1984). The seed cone angle, the inclination and length of awn tail and the length and inclination of awn hairs influence the seed position. The configuration of interest is the wound one, because it is the unwinding movement that pushes the seed forward, while the *Erodium* anchorage is provided by awn tale and/or the awn hairs (Fig. 59a). The orientation of the awn hairs and the seed barbs is important for the anchorage as they prevent the backward movement. This configuration depends on whether the awn tail touches or not the ground, as well as on potential contacts between hairs and ground; a main affected quantity is the seed leverage angle shown in Figure 59a.

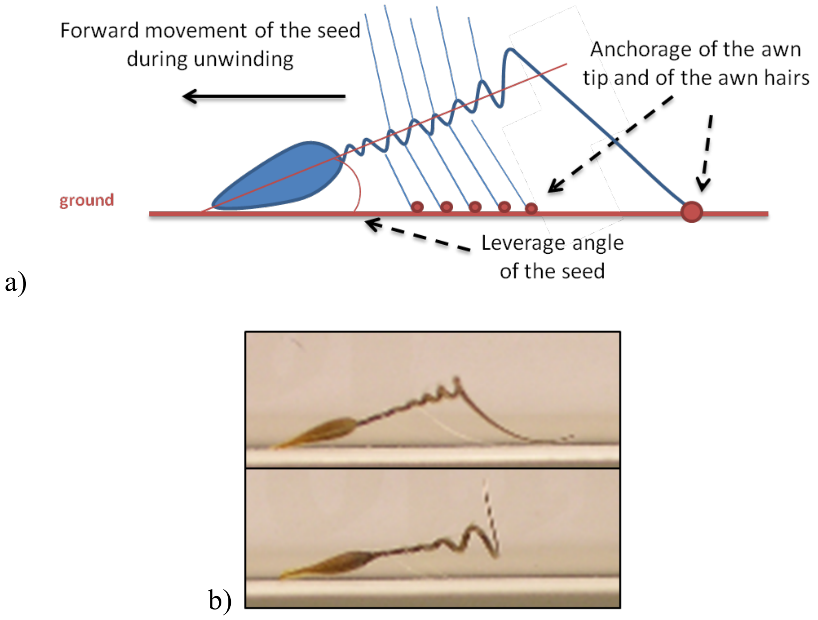

Fig. 59 Scheme of the *Erodium* seed positioning, leverage, and anchorage a) during the forward movement of the seed, and b) with respect to the position of the awn tail.

6.6.2 Movement of the awn hairs

The awn hairs are situated on the non-hygroscopic dorsal layer and they are not hygroscopic as previous described in section 4. They have a compliant type of movement. During the winding and unwinding of the awn the awn hairs move as well: they close during unwinding and open during winding (Fig. 60a). The awn hairs movement can play an important role in the interaction of *Erodium* and the soil during the winding and unwinding.

In order to better understand the emergence of awn hairs movement a physical model was build. The awn model was built as described in the section “Bilayer principle”, by putting the silicon layer on the pretensioned elastic band. Plastic flexible bands were added on the silicon layer before the silicon had cured (Fig. 48a).

By winding and unwinding of the flexible band movement of the plastic hairs can be observed (Fig. 60b). They become opened during the winding and closed during the unwinding similarly to the *Erodium*.

a)

b)

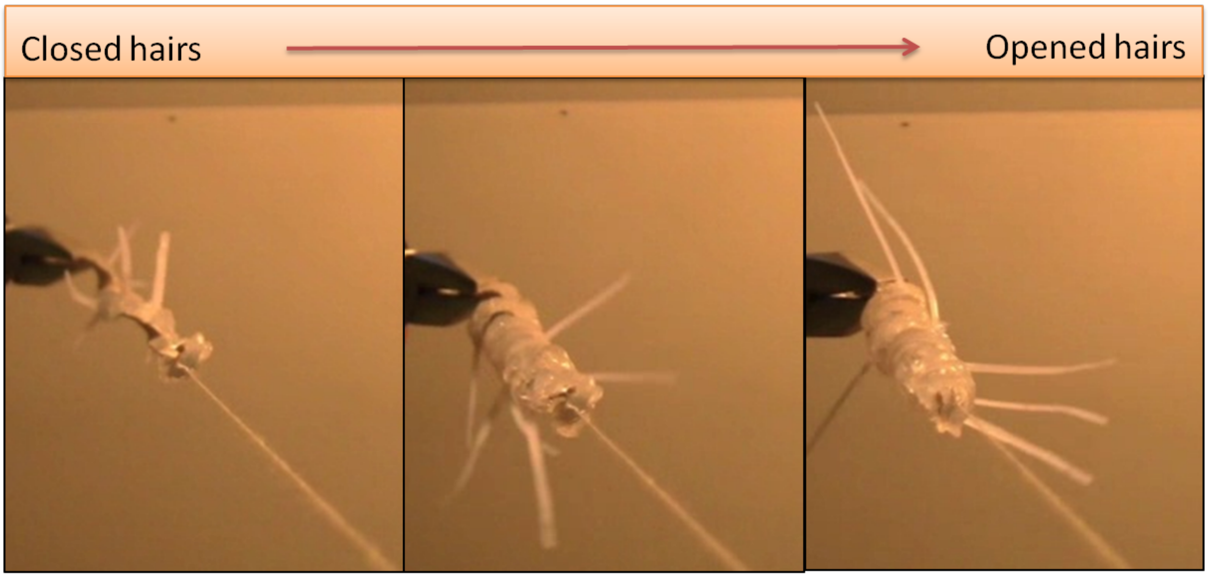

Fig.60 Picture of a) the winding *Erodium* awn and b) winding physical-model awn to visualize the sequence of the opening *Erodium* hairs and plastic artificial hairs.

6.6.3 Seed leverage with respect to the gravity and the awn geometry

Being the seed leverage very important for the soil penetration, the seed position on the ground was analysed by numerical models, namely 3D FE models. Three configurations were tested with the wound awn: i) the anchorage is provided by the awn tip, with the awn tail modelled as a straight rod; ii) the anchorage is provided by the awn tip, with the awn tail modelled as logarithmic spiral; and iii) the anchorage is provided by the awn hair.

Gravity is a main parameter to take into account for the space exploration of planetary bodies. The objective was to evaluate the deformation of the structure under its own weight and resulting changes in seed leverage in different gravitational conditions: Earth (g = 9.8 N·kg^{-1}), Moon (g = 1.62 N·kg^{-1}), Mars (g = 3.71 N·kg^{-1}), and Jupiter (g = 24.92 N·kg^{-1}). Moon and Mars were chosen as the closest target planetary objects, whereas Jupiter was chosen as the most massive planet in the Solar System and thus with worst gravitational conditions from structural viewpoint. It is worth to notice that the contact between structure and ground provided by the weight is considered to be sufficient to keep contact (i.e., for the seed to be in contact with the soil). This assumption is not generally true under low gravity conditions, yet modelling of such an aspect is outside the scope of the present document (it will be tackled by subsequent investigations).

All the simulations were performed with the geometrical parameters of a real *Erodium* seed (Fig. 61); they are reported in the Tab. 13. The size of body is very important for the structural evaluation, since it simultaneously affects weight and stiffness (due to mass distribution). To this purpose, three sizes were tested with the same geometry: small length scale of the real *Erodium* – order of mm (i.e., total length is approximately 2 cm), middle length scale – order of cm (total length is approximately 2 dm), and large length scale – order of dm (total length is approximately 2 m).

All the models were built in Comsol Multiphysics 4.3 by using the Beam Module and solving the stationary problem. The awn was modelled as a logarithmic helix beam with rectangular cross section. The seed was modelled as a beam of circular cross section instead of a cone solid, for simplicity. The equivalent diameter of cross section was chosen in a way that the total volume was the same as for the conical seed with the same height. No contacts were implemented, for simplicity; anchoring was imposed by suitable constraints (see below). The material properties were the same as used by Evangelista *et al.* (2011): Young's modulus =9×10^9 Pa, Poison's ratio = 0.33, and density = 800 kg·m^{-3}.

The seed model was position on the ground as in Fig. 59. The gravity vector was perpendicular to the ground. Two constrains were applied: i) the seed tip can slide only along one longitudinal axis on the ground plane; ii) the awn tip/awn hair can only rotate on the ground around an axis that is perpendicular to the seed-sliding axis (Fig. 62).

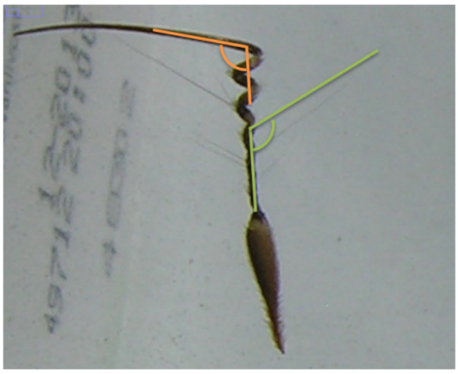

Fig. 61 Picture of the Erodium taken as a reference for the geometrical parameters of model. The awn hair angle and the awn tail angle are indicated in green and orange respectively.

Tab. 13. Geometrical parameters of the reference *Erodium*. Parameter signed by * is taken from Evangelista *et al.* (2011).

Parameter	**Value**
Awn maximum diameter	2 mm
Awn spiral angle*	86°
Number of coils	7
Awn height	16 mm
Section width	0.5 mm
Section height	0.25 mm
Awn mass	1.47µg
Awn tail length	11 mm
Awn tail angle	101°
Seed mass	1.32 µg
Seed height	8 mm
Seed diameter	1 mm
Seed equivalent diameter	1.366
Awn hair length	6 mm
Awn hair angle	125°
Awn hair diameter	60 µm

6.6.4 Awn tip anchorage: straight awn tail

The first model has a simplified geometry for the awn tail. It has as a straight-rod shape tangent to the final segment of the last awn helix (Fig. 62). The objective of these simulations was to verify how the size and different gravity conditions (i.e., load conditions) may influence the seed leverage.

In Fig. 63 the resulting von Mises stress, rotational field around *x*, and qualitative deformation plots for the structures of small, middle, and big dimensions in Earth gravity conditions are shown. The stresses and rotational field increase with increasing dimensions, linearly. Variations of the seed leverage angle with respect to the dimension of structure and gravity conditions are reported in the Table 14. The seed leverage angle changes appreciably only for the conditions on Jupiter for the large structure (i.e., the seed have been lowered by approximately 2.57°) (Fig. 64). In all the others cases angle variation is less than half degree.

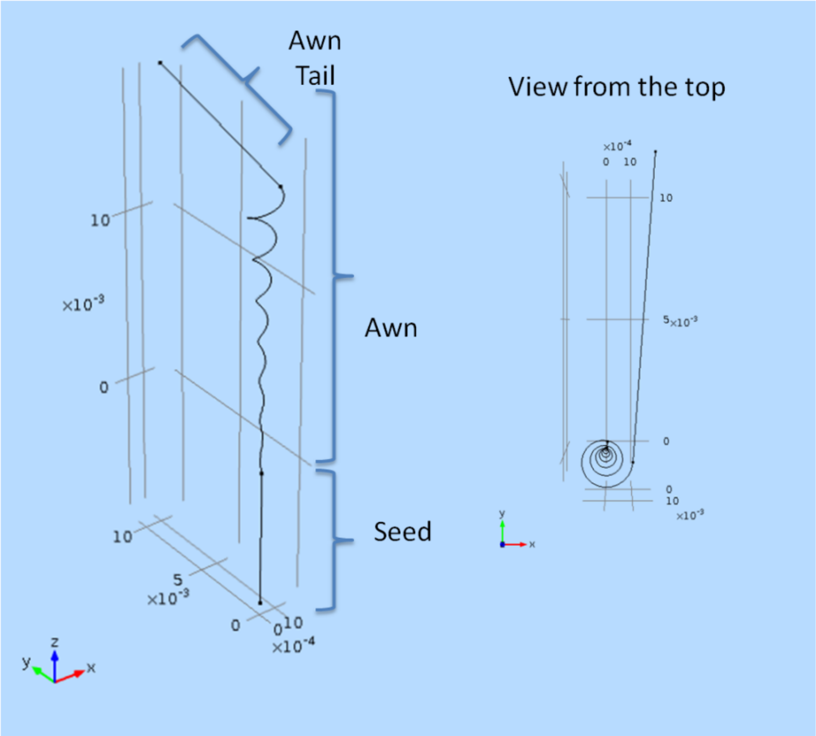

Fig. 62 Model geometry of *Erodium* with straight awn tail. The reported numbers are in m.

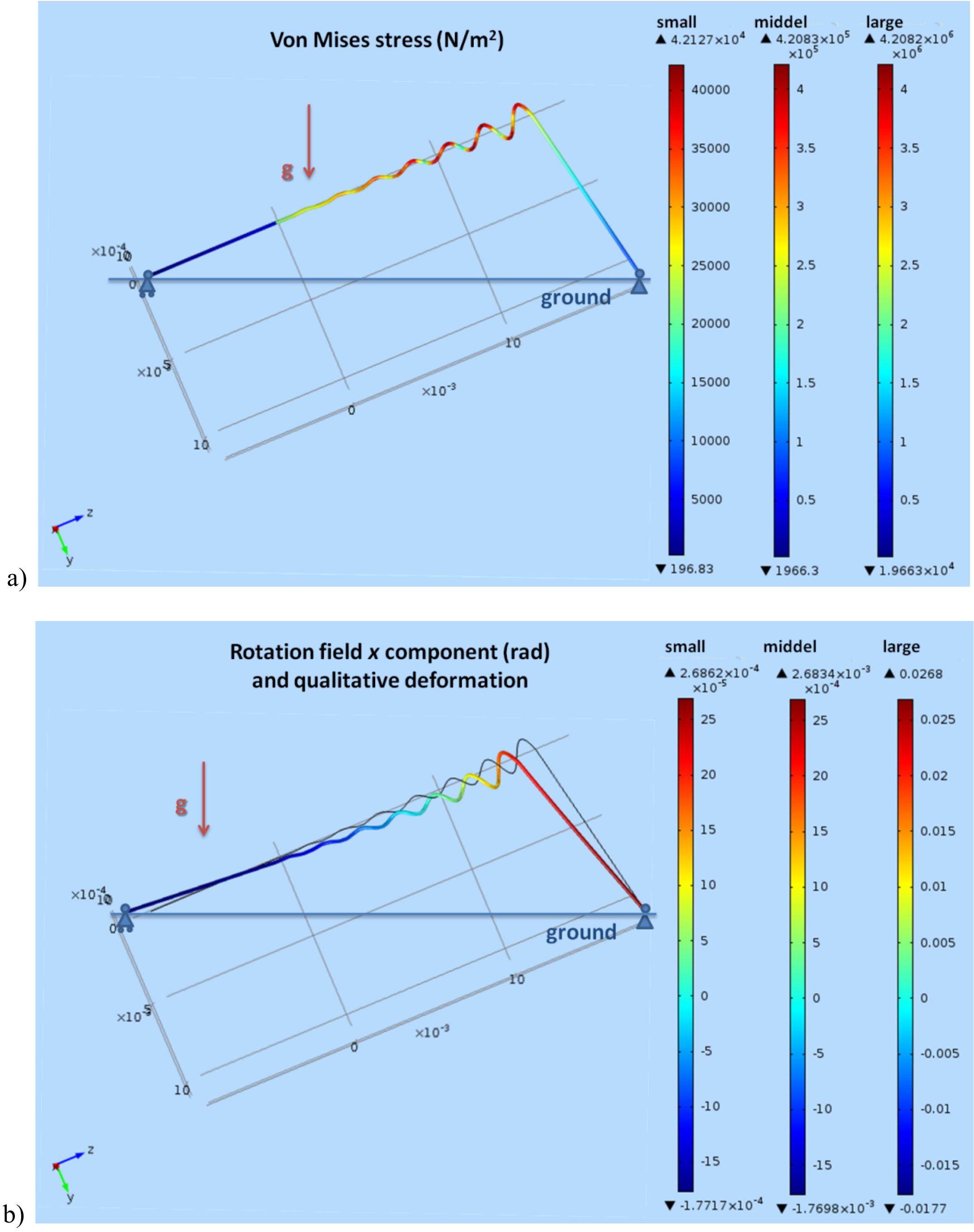

Fig. 63 Plots of a) von Mises stress, and b) rotational field around *x* and qualitative deformation of the *Erodium* with anchored straight awn tail on the ground in the Earth gravity conditions for small, middle, and large length scales. The gravity vector is indicated by **g** and is 9.8 m·s^{-2}. Two constrains on the seed tip and on the tail tip are indicated together with the ground line.

Table 14. Variations of the seed leverage angle (rad) with respect to the length scale of structure and gravity conditions for the *Erodium* with anchorage by straight awn tail.

	Earth	Moon	Mars	Jupiter
small length scale	1.77×10^{-4}	0.292×10^{-4}	0.671×10^{-4}	4.51×10^{-4}
middle length scale	1.77×10^{-3}	0.292×10^{-3}	0.671×10^{-3}	4.51×10^{-3}
large length scale	1.77×10^{-2}	0.292×10^{-2}	0.671×10^{-2}	4.51×10^{-2}

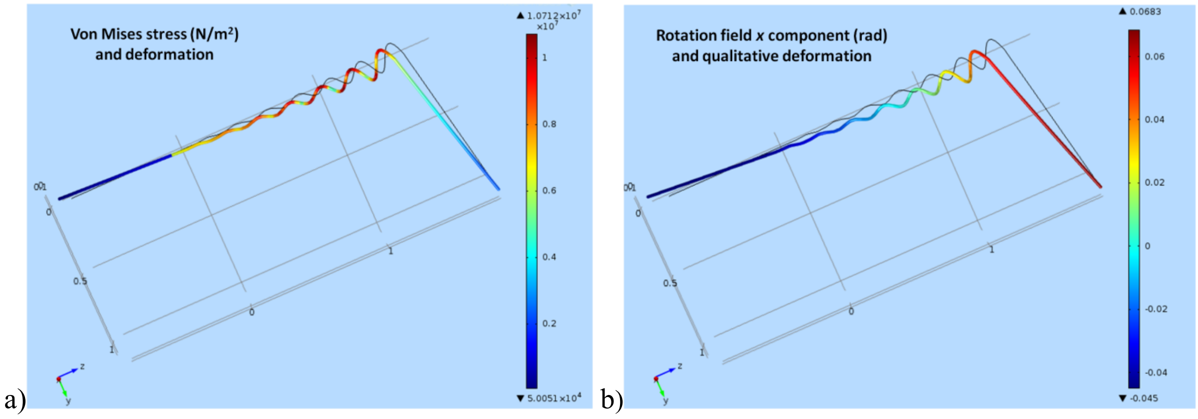

Fig. 64 Plots of a) von Mises stress and deformation, and b) rotational field around *x* and qualitative deformation of the *Erodium* with anchored straight awn tail on the ground in the Jupiter gravity conditions with large length scale.

6.6.5 Awn tip anchorage: logarithmic awn tail

The second model has the awn tail with a curved geometry similarly to the real *Erodium*. The curved geometry is more appropriated from the kinematic viewpoint, for example for rolling on the ground, but can respond in different way to the loads with respect to the straight bar. The objective of these simulations was to verify if the curved awn tail induces some differences with respect to the previous model.

The curve was described by a logarithmic helix and it is continuous with the awn main structure (Fig. 65). It was found that the resulted stresses and deformations were substantially the same. However, from the variations of seed leverage angle (Table 15) it can be observed that a curved tail resists slightly better (i.e., the seed has been lowered 7% less with respect to the previous case).

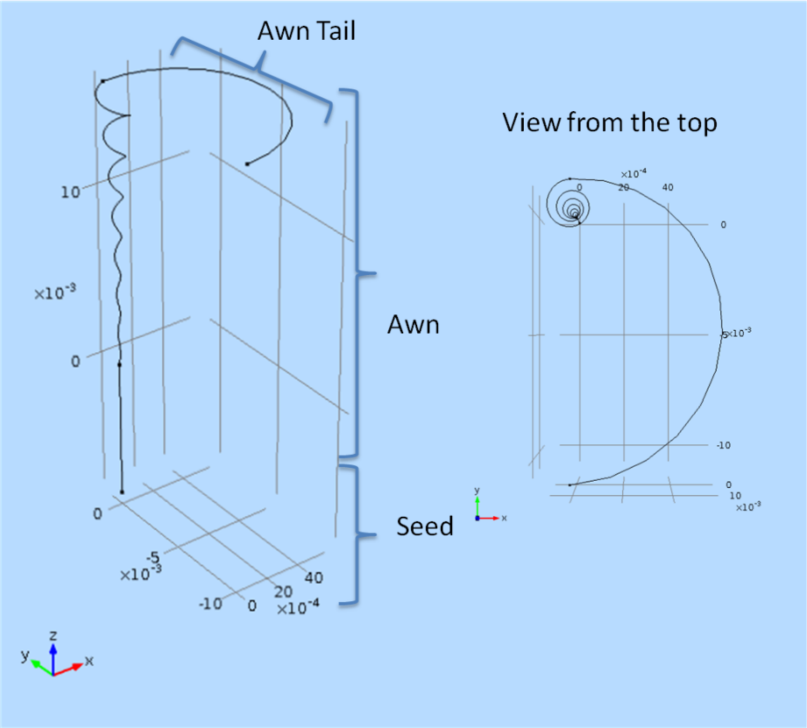

Fig. 65 Model geometry of *Erodium* with curved awn tail. The curve is defined by a logarithmic helix. The reported numbers are in m.

Table 15. Variations of the seed leverage angle (rad) with respect to the length scale of structure and gravity conditions for the *Erodium* with anchorage by curved awn tail.

	Earth	**Moon**	**Mars**	**Jupiter**
small length scale	1.66×10^{-4}	0.275×10^{-4}	0.630×10^{-4}	4.23×10^{-4}
middle length scale	1.66×10^{-3}	0.275×10^{-3}	0.630×10^{-3}	4.23×10^{-3}
large length scale	1.66×10^{-2}	0.275×10^{-2}	0.630×10^{-2}	4.23×10^{-2}

6.6.6 Awn hair anchorage

The third model takes into account the contribution of awn hairs into the seed leverage on the ground. The awn hair was modelled on the fifth coil as one indicated in the Fig. 60. The objective was to evaluate the deformation of the structure with respect to the dimensions and gravity conditions.
The awn tail was modelled as in the second model but rotated upward in order to avoid the contact with the ground. The structure resisted only with small dimensions and collapsed under its weight for bigger ones, because of the awn hair buckling. In the Table 16 are reported variations of the seed leverage angle (rad) with respect to the gravity conditions. The seed have been lowered appreciably in Earth and Jupiter conditions (i.e., 0.61° and 1.56° respectively) (Fig. 66), while other two cases angle variation is less than half degree.
It seems that the awn hair anchorage can be functional only for the structure of a dimension comparable with the *Erodium* one; however the cooperative anchorage of more than one awn hair may be successful also for the bigger dimensions.

Table 16. Variations of the seed leverage angle (rad) with respect to the gravity conditions for the *Erodium* with anchorage by awn hair and small length scale dimensions.

	Earth	Moon	Mars	Jupiter
small length scale	1.07×10^{-2}	0.177×10^{-2}	0.405×10^{-2}	2.72×10^{-2}

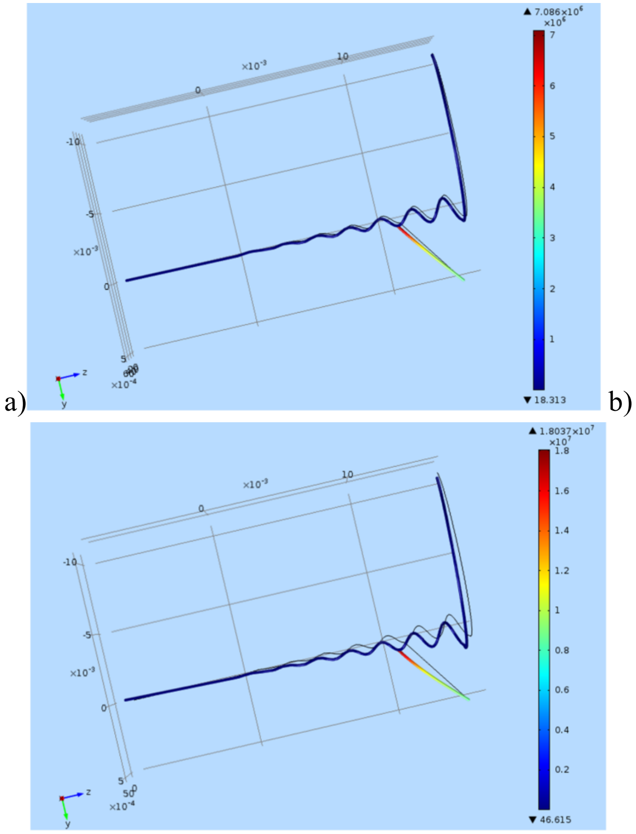

Fig. 66 Plots of von Mises stress and deformation of the small-length-scalen *Erodium* with anchored awn hair in a) Earth and b) Jupiter gravity conditions.

6.7 Seed penetration into soil

Penetration problems in geomechanics involve the insertion or intrusion of solid bodies into the ground. Numerical modelling of such problems can improve our understanding of the physical processes involved, which in turn can lead to better interpretation of test results and more accurate estimation of soil dynamics and characteristics. Moreover, it can effectively support the development of high-tech artificial devices well suited for optimal navigation and soil monitoring/exploration.

6.7.1 State-Of-Art modelling approaches

Several modelling strategies were proposed for tackling such a problem mainly based on the finite element approach (see below). However, such simulations are extremely complex, mainly because the problem involves large deformations that make it difficult to design an appropriate finite element mesh. Indeed, at least in principle, the soil elements beneath and around the penetrating body should be sufficiently small to achieve good accuracy in the numerical results. However, the use of fine elements inevitably leads to severe mesh distortion and even negative element Jacobians due to the very large deformation in the soil around the penetrating body.

One of the early attempts to solve penetration problems numerically was made by Kiousis (2005), who proposed a smart strategy to simulate the displacement of piles into the ground by introducing artificial node relocation. The model exploited the cylindrical symmetry of the problem and the displacements were obtained by large strain theory assumptions together with the imposition of a kinematic field similar to that one derived from expansion of cavities in soils (Vesic 1972). Kiousis model ruled penetration simulations till the early 90s when, thanks to the development of computer science and the increase in computational power, Van den Berg suggested the introduction of an Eulerean formulation in order to avoid mesh distortion and node relocation (Van den Berg et al. 1996). This new model managed to erase the incorrect assumption of a pre-bored hole superimposed to the axis of symmetry as initial condition for the penetration to proceed. Since no reliable solution was available to properly account for large plastic deformations, Van den Berg proposed to introduce an Eulerean framework in order to prevent any unwanted element distortion. The adopted Eulerean framework was a special case of the so-called Arbitrary Lagrangian Eulerean (ALE) method, in which the movement of the element nodes and the material points is decoupled. This method successfully avoided mesh distortion, allowing more complex penetration simulations, but it was limited to known material flows at boundaries. Moreover the method couldn't simulate the complete penetration process right from the ground surface. Nevertheless, it introduced a new paradigm for numerical modelling of penetration. With the introduction of Eulerean analysis it seemed to be possible to develop three-dimensional and more complex models without relying on the axial symmetry loading conditions and displacements.

In recent years, coupled Lagrangian-Eulerean simulations have been carried out for a large number of problems, especially in geomechanical ones involving large displacements and deformations (Mahutka et al. 2006). In this kind of simulations it is possible to recognize both Lagrangian and Eulerean descriptions in the same model. It is worth to recall few basic aspects for both approaches, for ease of presentation. As usual, if a continuum deforms or flows, the position of the small volumetric elements changes with time. These positions can be described as functions of time in two ways: for the Lagrangian approach, the movement of the continuum is specified as a function of its initial coordinates and time, while in the Eulerean description movement is specified as a function of its instantaneous position and time. In simulations based on the Lagrangian formulation the interface between two parts is precisely defined and tracked. In these simulations large deformation of a part can lead to extremely challenging (yet unavoidable) mesh and element distortion, as mentioned. Conversely, the Eulerean technique exploits a reference mesh which remains undistorted during deformation; however, the interface between two parts cannot be described as precisely as with the Lagrangian formulation. In view of these assets, a coupled Eulerean-Lagrangian (CEL) method was proposed, which successfully blends the strengths of both formulations above (Henke et al. 2007). In CEL simulations the Lagrangian mesh is generally used to discretize structures, while Eulerean mesh is used to discretize the soil (in this way, large soil deformations do not induce mesh distortion problems). This approach has however some limitations: in certain cases the required computational costs do not justify the accuracy of the results; contact formulation between Lagrangian and Eulerean bodies is not optimal, as some numerical diffusion can occur during the simulations; the model cannot simulate history-dependent material behaviours, such as the stress-path dependence exhibited by many soils.

A novel methodology was recently proposed in the biomechanical field (Oldfield et al. 2012), namely for the insertion of a needle in soft tissues. To study such a problem, a cohesive approach was used. More in detail, cohesive elements have been widely used in crack propagation analysis as they allow the inclusion of active surfaces as the simulations develop. An early attempt to use this technique was recently presented in another work ((Misra et al. 2008), based on cohesive elements with two active faces: using a simple traction-separation relationship (in which the force is directly proportional with displacement), it was possible to determine whether cohesive elements are intact or not (in the latter case, they are removed from the simulation). Based on this strategy, a line of zero-thickness cohesive elements has been introduced by Oldfield (2012), superimposed to the needle path, so as to simulate the progressive penetration of the rigid needle into the tissue below. By this method, a good level of accuracy can be obtained, but it is not possible to use axial symmetry, and the three-dimensional version of cohesive elements is not stable when facing large displacements (it only works for pre-defined penetration paths), and moreover material properties of the cohesive elements have to be introduced.

In summary, a killing strategy for numerical modelling of penetration problems is still an open research field already when considering the penetration of rigid bodies (thus accepting some degree of simplification) into a continuum medium. Techniques developed for non-linear solid mechanics and fluid mechanics (being the Eulerean approach mainly used in such a field) were successfully blended, yet the killing numerical scheme still has to come. A wise exploitation of principles from mechanics of cohesive materials was also introduced, holding potential for further developments. It seems reasonable to study penetration of deformable objects into the soil once consolidated proper methods for the simplified, rigid penetrator problems.

6.7.2 Seed penetration model

In the following a three dimensional model is presented, suitable for studying seed penetration into the soil. The model reminds the ones used by Kiousis and Van der Berg as the axial symmetry of the problem is exploited, thus avoiding plain strain approximations and with the main aim of saving computational costs. Due to his rigorous geometric and boundary conditions this model seems to be more accurate than the other state-of-art approaches. The dynamic implicit solver in the Abaqus 6.11 software was used. The finite element analysis software Abaqus was chosen, since it is worldwide recognized as the most powerful tool for the considered non-linear problems; moreover, the implicit integration method was chosen to improve accuracy and reliability of the solution. All the simulations were run on a dual core, Intel Xeon CPU @2.4+2.4 Ghz, and 48.0 GB RAM computer.

Geometry

The model exploits the axial symmetry of the problem. The part simulating the soil is a rectangle 15-mm wide and 15-mm deep having one side relied on the axis of symmetry, the dimensions of the part are chosen to avoid any boundary interferences while saving computational costs.

The part simulating the seed is instead modelled as half of a cylinder with a conic tip. The dimensions of the seed are strictly related with its conical tip; it was imposed in fact that the tip has to be 7.34 mm deep with a tip angle θ = 7.32°, as obtained by experimental measurements (Fig.67); in the following simulations three different values of the conical angle will be used in order to evaluate the influence of such a parameter on the penetration process (θ = 7.32°, θ = 14.64° that is twice the base geometry and θ = 3.66° that is half the base geometry), this choices lead to three different radius values of the cylindrical part of the seed (Fig. 68). The deep dimension of the cylindrical tip of the seed is not important for the simulations and it was imposed to 2 mm.

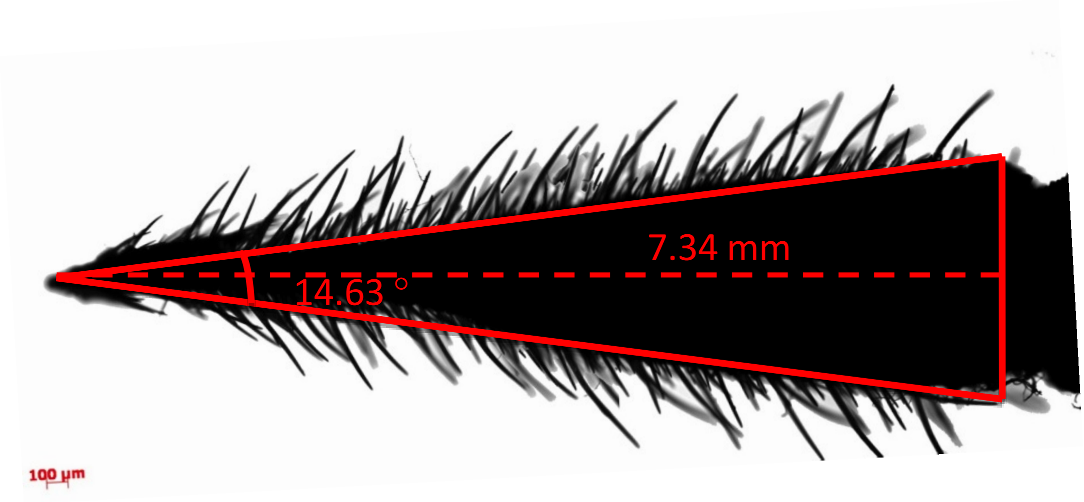

Fig. 67 Seed dimensions obtained by experimental measurements, the image was made by using optical microscope.

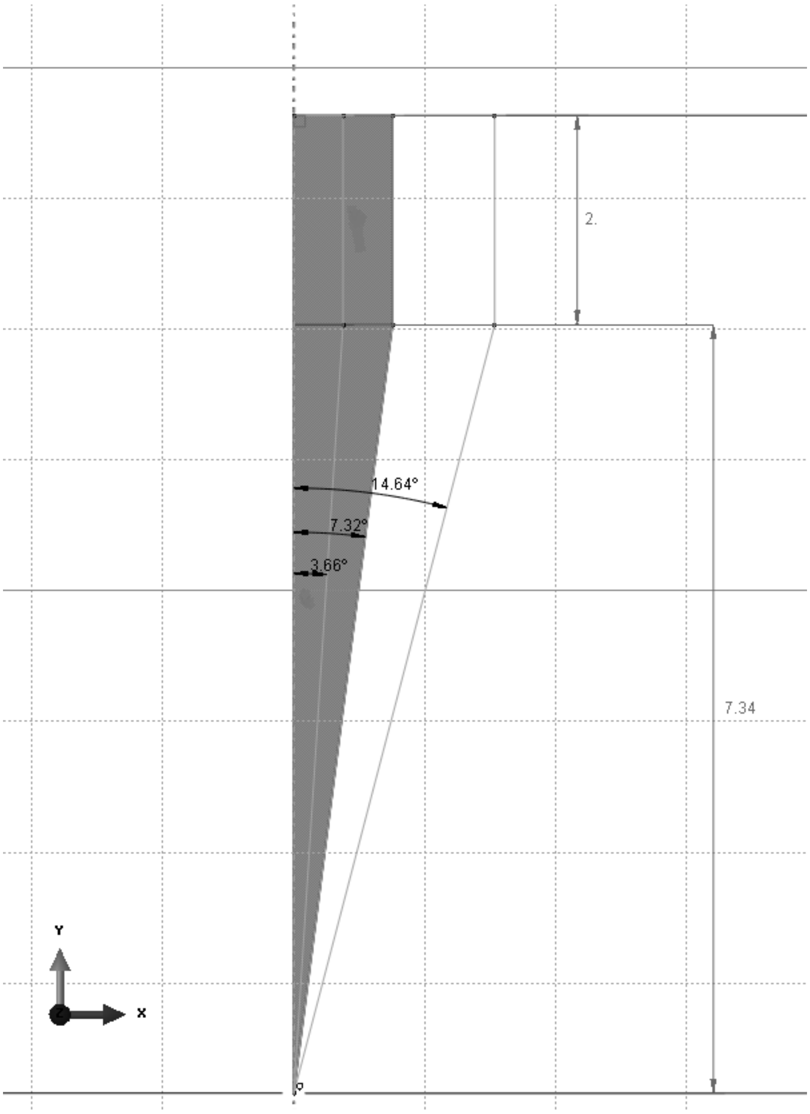

Fig. 68 Alternative model geometries obtained by varying the tip angle ϑ. In grey the experimental measured shape is shown. The reported numbers are in mm.

Finite element simulation methodology

It would be extremely expensive to model the penetration process of the seed into soil using a complete three-dimensional formulation. Instead, using the symmetry of the problem, an axis-symmetric simulation has been constructed. The two parts of the model were meshed using three nodes linear axis-symmetric elements CAX3. The whole model is formed by 1150 nodes and 2096 elements, 1800 of which were used on the soil part.

To model the seed movement it has been necessary to introduce a reference node. The reference node provides the point at which displacement or force boundary conditions are applied as an input and/or reaction forces and penetration displacements are obtained as an output. Using the reference node allows to apply boundary conditions correctly to all the elements of the seed.

All contacts in the model were defined by using the penalty contact algorithm (Abaqus Theory Manual 2008). Contact formulation is one of the key aspects of the model. It involves: the external surfaces of the seed, the top surface of the soil (ground surface) and the side of the soil model relying on the axis of symmetry. The seed is considered the "master" surface, thus it has been modelled using a finer mesh having an average dimension element of

0.74 mm, while the other surfaces are considered the “slave” ones with an average dimension element of 1.5 mm; the “master-slave” formulation simply states that slave nodes cannot penetrate master surfaces while the opposite is still possible. As for the normal behaviour, the penalty method has been taken in consideration, while for the tangential behaviour a trial value (equal to 0.1) for the friction coefficient was imposed between seed and soil.
As for the boundary conditions, the bottom edge of the soil part is free to move tangentially but not normally, and the same condition has been imposed for the side edge of the soil part. The nodes superimposed to the axis of symmetry are free to move along the axis, while they have to maintain the cylindrical symmetry when moving normally. The ground surface has been left free to move and the boundary conditions on the seed have been imposed to the reference node. Furthermore, the reference node of the seed is forced to move along the axis of symmetry and cannot rotate.
Finally, great efforts were made to achieve the best combination between results stability and model reliability by tuning convergence values. Indeed, in implicit models the ALE remeshing technique cannot be used, and so evaluating convergence values becomes the main task to reach solution stability and avoiding mesh distortion. Convergence parameters can be obtained from the numerical model.

Material properties

The choice of the materials’ models to be used was not obvious. To evaluate the stability of the model simply linear elastic models were firstly used to simulate the soil. This obviously lead to unrealistic force values needed to penetrate the soil, but it allowed tuning convergence parameters and meshing dimensions to avoid excessive elements distortions. Once stability was achieved it has been imposed to use a more realistic, porous elastic model to simulate the soil behaviour, while for the seed the simple linear elastic model was considered sufficiently accurate.

In Abaqus the porous elastic material model is characterized by four different parameters:

- Bulk modulus
- Poisson’s ratio
- Void ratio
- Tensile limit

The bulk modulus and the Poisson’s ratio describe the resistance to a three axial compression and the ratio between transverse and axial strain respectively and were obtained from the literature (Baltodano et al. 2006).
The void ratio is defined as the ratio of the volume of voids to the volume of solid material. A face-centred cubic regular lattice packing (for which packing efficiency is optimal, Gauss et al. 1931) was assumed: it implied a void ratio equal to 0.24. Such an extremum value (which overestimates the void ratio of real soils as well as that of the dummy soils reported in Tab. 3), was chosen not to focus on porosity at this stage (indeed, seed geometry was primarily addressed). In the same spirit, a large value for soil density was chosen, see Tab. 17.
Moreover, the tensile limit in Abaqus mainly describes the traction behaviour of the porous materials. In the porous model, in fact, the elastic part of the material volume change is considered proportional to the logarithm of the pressure stress, according to the following equation:

$$\frac{\kappa}{(1+e_0)}\ln\left(\frac{p_0+p_t^{el}}{p+p_t^{el}}\right) = J^{el} - 1 \tag{3}$$

where κ is the logarithmic bulk modulus,
e_0 is the initial void ratio,
p is the equivalent pressure stress, defined by:

$$p = -\frac{1}{3} trace\, \boldsymbol{\sigma} = -\frac{1}{3}(\sigma_{11} + \sigma_{22} + \sigma_{33}) \tag{4}$$

In which the initial value of the equivalent pressure stress; J^{el} is the elastic part of the volume ratio between the current and reference configurations, and p_t^{el} is the elastic tensile strength (tensile limit) of the material (in the sense that $J^{el} \to \infty$ as $p \to -p_t^{el}$). The stress-deformation behaviour of the considered material model is shown in Fig. 69.

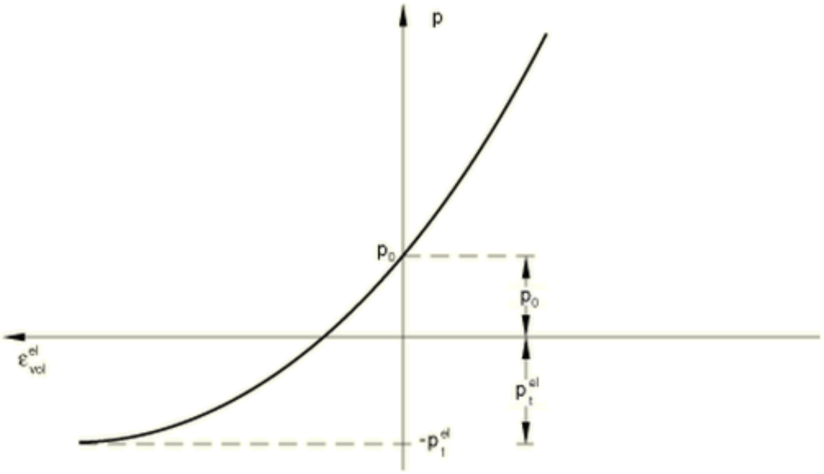

Fig. 69 Plot of the typical stress-deformation relationship for an elastic porous material model (Abaqus Theory Manual 2008).

In the carried out simulations, the condition $p_0 = 0$ was imposed (so, no initial stresses are present in the undeformed soil), while tensile limit was obtained from literature (Baltodano et al. 2006). Relevant values are reported in
Table 17. Seed material properties are obtained from (Evangelista et al. 2011).

Table 17. Material models' properties used in simulations.

Seed Material Model		
Young's Modulus [GPa]	Poisson's Ratio [--]	Density [Kg/m^3]
10	0.3	800

Soil Material Model				
Log Bulk Modulus [GPa]	Poisson's Ratio [--]	Tensile Limit [Pa]	Density [Kg/m^3]	Void Ratio [--]

4	0.3	100	1800	0.24

6.8 Results of the finite element simulations

The results of the simulations are reported below; they are also compared with known experimental data. In particular, using the maximum force attainable by the seed, the penetration displacement is investigated.

The simulations start with the seed completely outside of the soil part, as in Fig. 70, these initial conditions are the same for all the carried out simulations. Parameters and modelling options varied during the simulations are listed below:

- Seed geometry (θ = 7.32°, 14.64° and 3.66°),
- Soil material model (Porous elastic, Linear elastic)
- Loading conditions (linear increasing force/displacement, smooth step increasing force)
- Damping effects

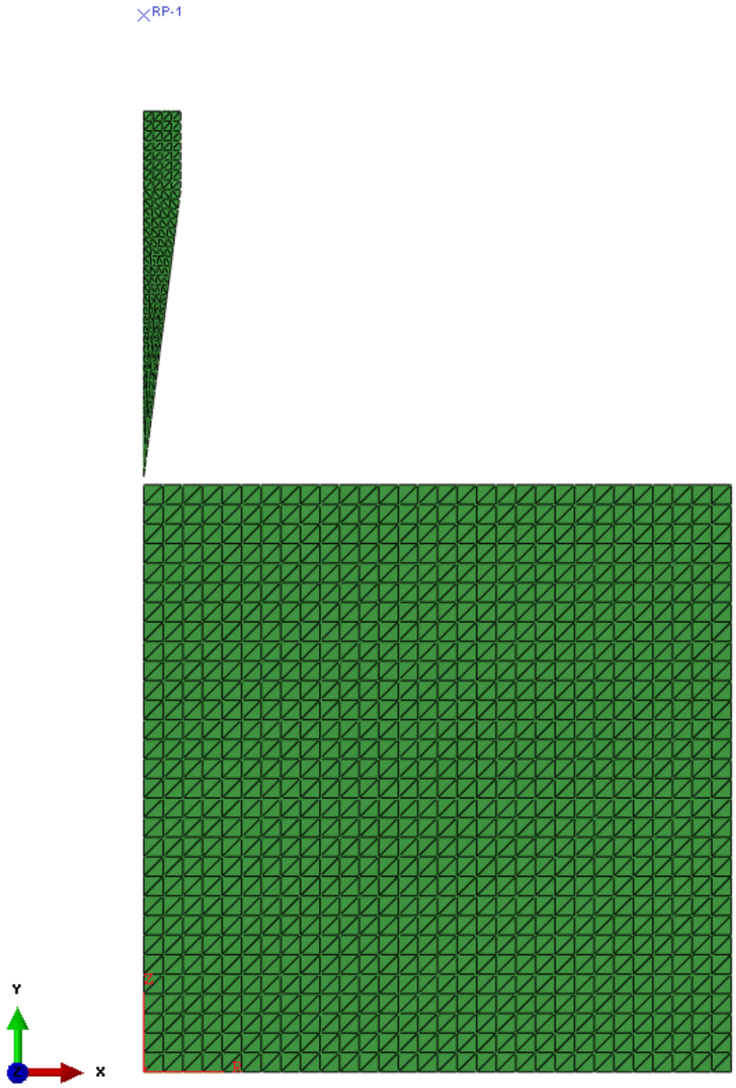

Fig. 70 Initial configuration, also showing mesh density and reference axes.

6.8.1 Assessment of the soil material model

Preliminary numerical experiments with a linear-Elastic model

In the preliminary simulations, a simple linear-elastic model was considered, with the aim of tuning relevant parameters so as to obtain convergence. In this case, we used a Young's Modulus for the soil of 10 MPa and 80 MPa, according to literature values for sandy soils.
Seed geometry used in this simulation is that one obtained by experimental measurements ($\theta = 7.32°$). The seed was forced to penetrate the soil for 7.34 mm, that is the whole height of the conical tip; reaction forces on the seed were obtained (nonrealistic values were expected, due to the assumed fictitious material behaviour, as remarked above).
Despite the lack of interest from a quantitative viewpoint in these preliminary numerical tests, useful information was obtained. In particular, it was proved that adopted geometry and mesh (together with boundary conditions) successfully manage to cope with the considered problem: simulation was stable advanced and no critical mesh distortions occurred.

Assessment of the porous-elastic model

Once discretization criteria for stability were matched as described above, more suitable material model was considered. More in detail, in order to improve the soil mechanics simulations, a porous-elastic behaviour was chosen. Soil properties values were obtained from literature as reported in Table 17.
In this simulation the seed penetration was forced, as in the above discussed numerical experiments.
The obtained force-displacement trend is shown in Fig. 71. The resulting penetration force is well below the one measured as described in Sec. 4.4, for many reasons: the friction coefficient used in the simulation could not be physically assigned (due to the high dispersion of the targeted soil values, as well as the lack of data), the seed geometry is ideally smooth; the force measured as mentioned above is maximized by the constraint on lateral deformation of the tail (so that it is reasonable that the seed penetrates by exploiting a sensibly lower force while unwinding). Some localized numerical issues can be noted in figure but it can be seen that the correct force-time behaviour is globally achieved. In Fig. 72 some plots of von Mises stresses during the numerical simulation are shown.

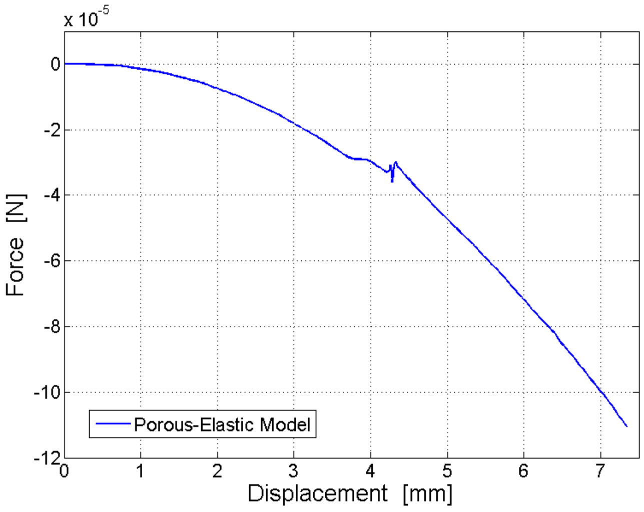

Fig. 71 Force-Displacement graph related to the Porous-Elastic material model.

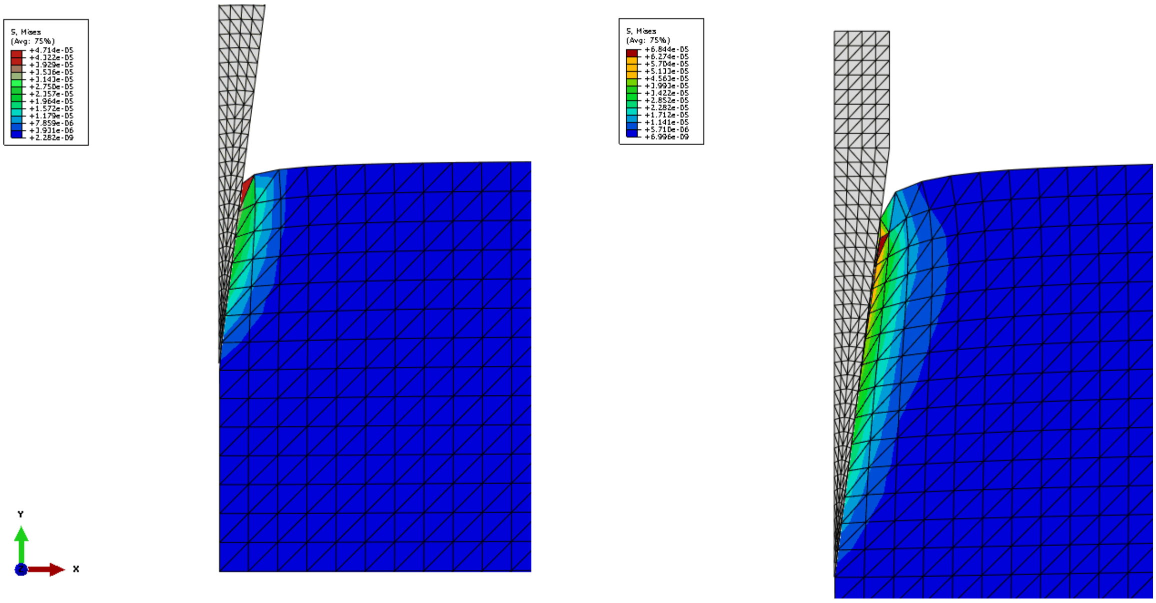

Fig. 72 Von Mises Stresses fields are shown. On the left half penetration is considered, it can be seen that the corner element is the most stressed and causes local numerical issues. On the right instead Von Mises Stresses at the end of the simulation are depicted.

6.8.2 Seed penetration by assigning the force

The core numerical investigation was carried out by assigning a penetration force equal to 10^{-4} *N*; consistently with the results discussed in Sec. 6.8.1 (we are aware of the ideality of the assumed value, which could be in principle scaled once determined the actual values of the parameters involved in the penetration task). In particular, penetration force was assumed to increase from zero to 10^{-4} *N*. Dynamics was credited to possibly play a role for such a simulation and therefore several conditions were considered (besides studying the effect of damping, as described below). In particular, two loading time-functions were used:

-A linear function: in which the force was linearly increased from zero to the maximum 1E-4 *N* during the first 30 seconds (after which it was kept constant);

-A smooth function, in which the force increased following a smoother time profile;

The considered time-functions are shown in Fig. 73.

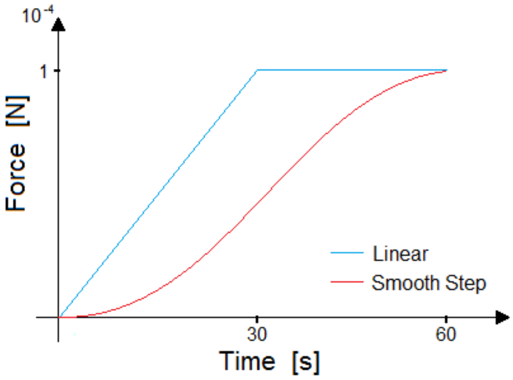

Fig. 73 Loading conditions.

Fig. 74 shows the obtained results, namely displacement-time plots for both linear and smooth step loading conditions. Some differences occur between the two loading settings. It is worth remarking how non-negligible dynamic effects occur for both loading conditions: travelling stress waves can be observed for example in the last time increments of the simulations, as the curves show. Indeed, the absence of damping terms in soil material model lead to maximum penetration displacement in a non-asymptotic way, since some sort of vibrations around the equilibrium persists for rather long time-intervals. In Fig. 75 some plots of von Mises stresses during the numerical simulation with different loading conditions are shown.

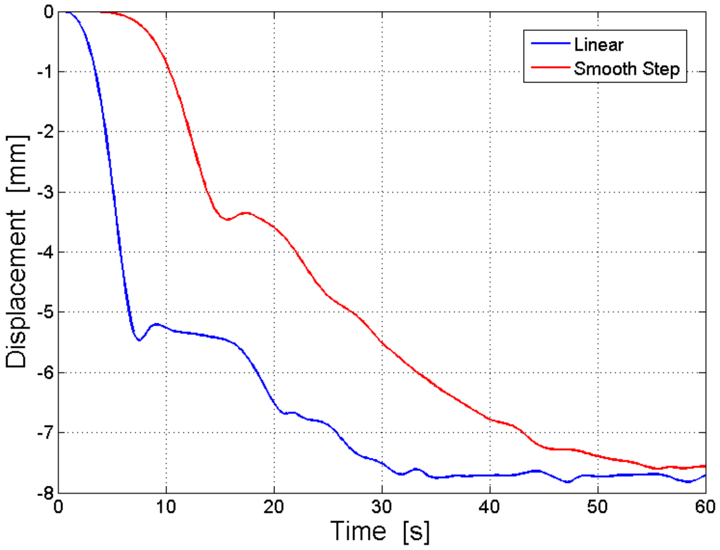

Fig. 74 Seed penetration versus time, for a given physically based force. Two loading conditions are considered.

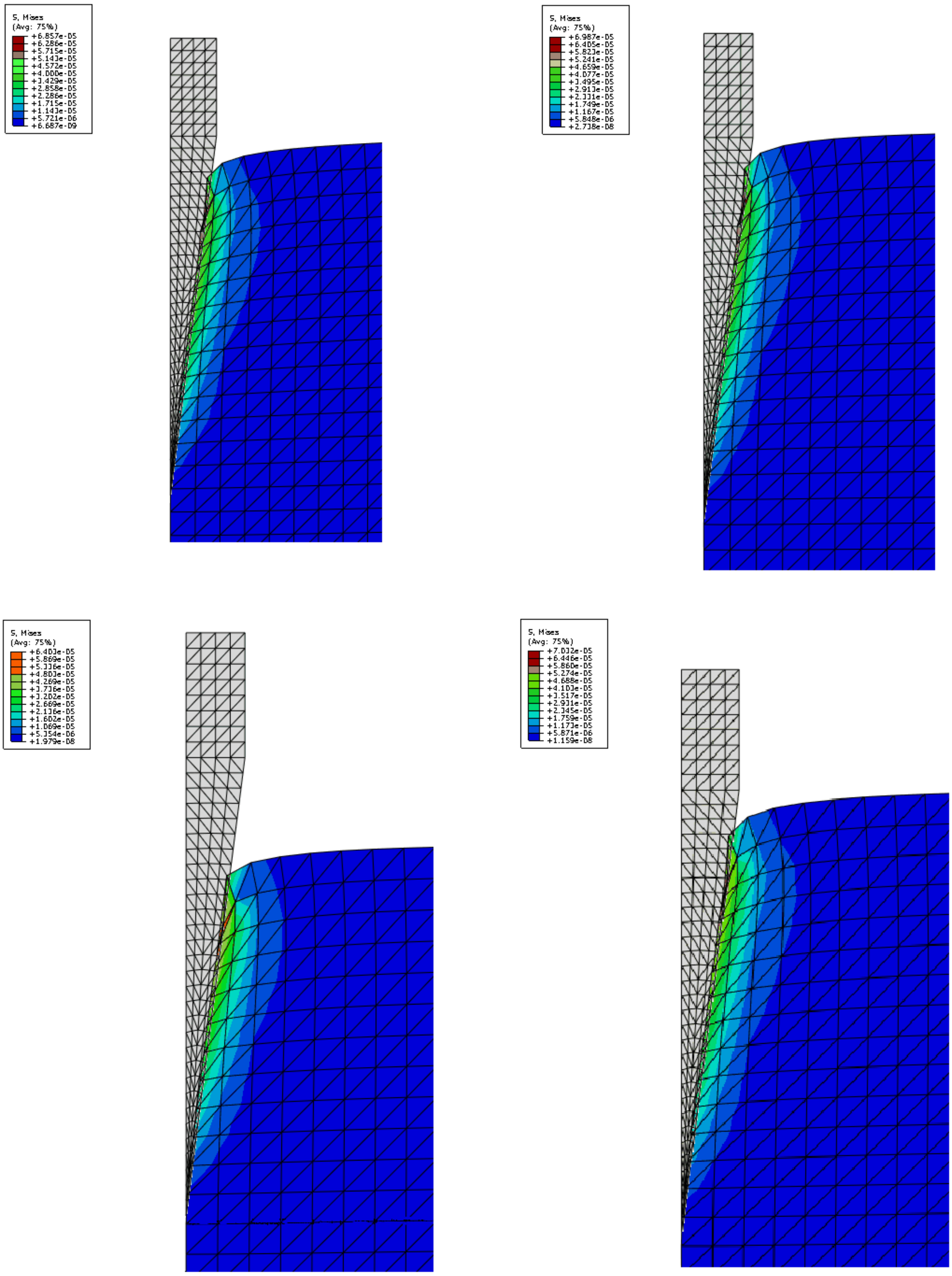

Figure 75 Von Mises Stress Fields are shown for both loading conditions. (a) Stresses after 30 seconds in the linear simulation and (b) at the end of it, (c) stresses after 30 seconds of the smooth step simulation and (d) at the end of it.

Moreover, dynamic effects appeared stronger in the initial stage (especially for the linear loading condition), consistently with the fact that during the final stage soil bounding over the seed surface plays a major role. The sensitivity of the simulation to the initial conditions is responsible for the discrepancies between the two curves in Fig. 74. Indeed, by starting the simulation with the seed (steady and) in contact with the soil part, closer results would have been achieved. However, it is very challenging to implement such an initial condition, due to numerical issue impinging on convergence. More numerical experiments were nonetheless justified prior to enriching the material model with some damping effects, in order to make it more realistic (see below). Nevertheless, the smooth load profile was expected to more closely (yet still qualitatively) match the real penetration dynamics of the seed.

6.8.3 Soil Damping

To better describe soil material properties it is necessary to also account for damping (such an enhancement does not bring major computational burdens on the developed model.). A mass-related damping term $\beta = 0.5$ was chosen, in order to magnify the effects of damping on soil dynamics.

In Fig. 76 the differences between the two material models are underlined. It is clear that the introduction of damping does not affect model results in an appreciable way. Moreover, it results that the penetration time is comparable with that of the real penetration task (which must be counted over the elongation cycles). Obtained results support the suitability of the developed numerical model for studying the seed penetration problem, especially by exploiting physically measured values of the involved parameters (further investigations are needed on regard).

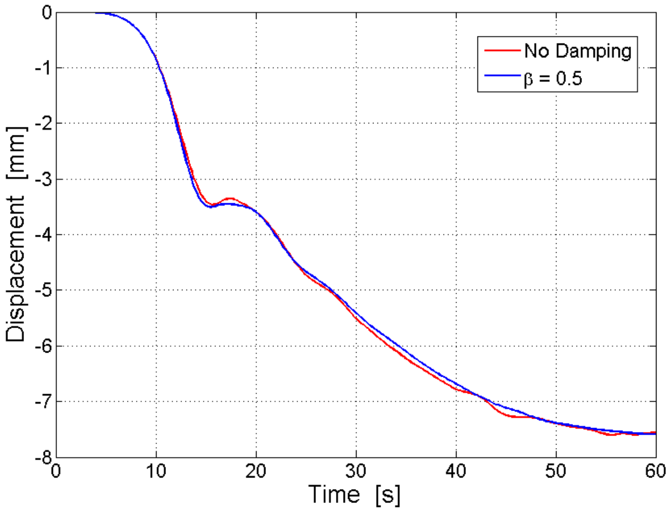

Figure 76 Seed penetration versus time, for a given physically based force. Force was applied smoothly (see Fig. 75c,d; soil damping was also considered.

6.8.4 Effect of seed geometry

The numerical study described above was repeated by considering the following seed tip angles:

- $\theta = 7.32°$ (as from experimental measures);
- $\theta = 14.64°$ (twice the experimental value)
- $\theta = 3.66°$ (half of the experimental value)

In all the simulations, the seed was forced to penetrate the soil for 7.34 mm (i.e., it was assumed that the seed should burrow itself completely), and the reaction forces on the seed will be obtained as an output and compared with the experimental ones.

In Fig. 77 are reported results of the simulations, some numerical errors can be seen for the larger tip angle geometry, saying that the stability of the solution is hard to achieve due to the larger mesh distortion and probably contact problems. However it can be observed that as expected the maximum reaction force acting on the seed is proportional to the normal section area of the seed, thus highlighting the significant sensitivity of the penetration task to the geometry of the seed. In Fig. 78 some plots of von Mises stresses during the numerical simulation with different seed geometries are shown.

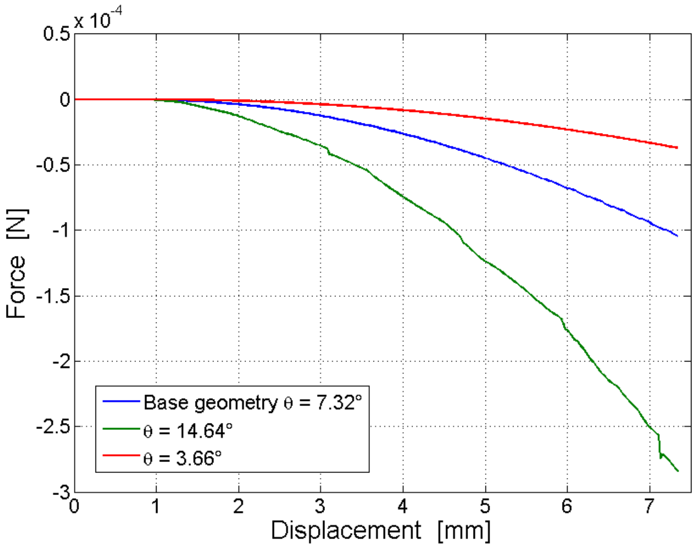

Fig. 77 Force-Displacement graphs for all the geometries considered

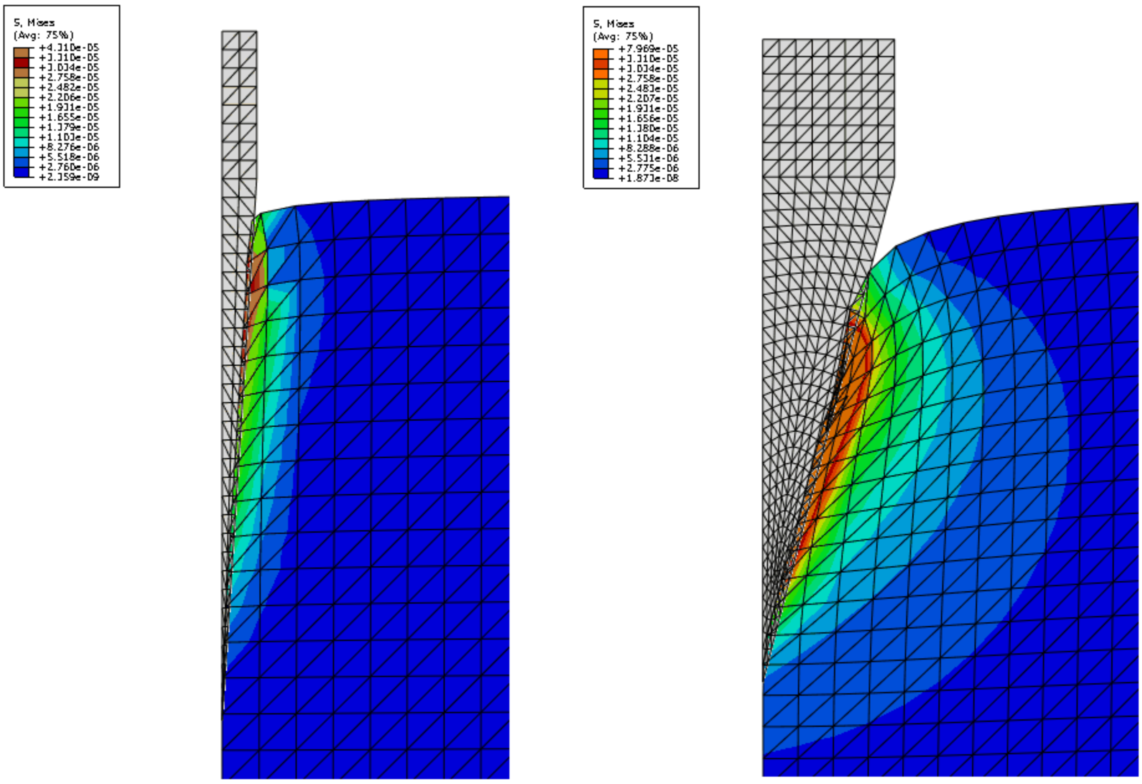

Fig. 78 Von Mises Stress fields for the alternative geometries considered.

6.9 Conclusions

A three-dimensional model for the simulation of seed penetration into soil has been developed.

It exploits a state-of-art numerical solver, by assuming a porous elastic material to simulate soil mechanics. Obtained trend for the penetration is consistent with the assumed parameters (underestimating soil resistance) and permit to highlight the effects of the considered parameters (soil damping, seed geometry) More experimental data are necessary to fully calibrate the model (primarily friction coefficients). Nonetheless, further developments can be expected by adding more complex material models (such as models taking in consideration the plasticity of the soil as well as different stress-strain behaviors) or by performing the oblique penetration (i.e., with certain angle with respect to the plumb line). Further investigations are needed to assess such developmental lines.

6.10 Effects of seed rotation

The discussed model of the seed penetration into soil does not take into account the rotation of seed. However, it was found that the rotation may decrease the resistance to the penetration of the cone probes (Bengough et al. 1997). Hereafter we perform some theoretical considerations on the contribution of seed rotation to soil penetration based on the cone penetration mathematical model of Bengough and Mullins (1997).

The penetration resistance of a soil is the force per unit cross-sectional area of the penetrating probe, or in our case of the seed. The penetrating probe must overcome both the physical resistance of the soil to deformation and the frictional resistance at the probe-soil interface.

The mathematical model of Bengough and Mullins (1997) predicts effects of rotation period on resistance of conical probe. They considered theoretically the effect of rotation on penetration resistance in terms of the rotation period, T, the penetration rate, v, the stress normal to the surface of the probe, σ, the coefficient of soil-probe friction, μ, the soil-probe adhesion, c_a, and the probe radius, R. In their model they assumed a uniform distribution of the load over the surface of the cone not affected by rotation, homogeneity of the soil mechanical properties. Moreover, they assumed that the soil, when compressed, slides alongside the cone in continuous contact with it. The penetration resistance of the rotating probe, Q_{pRot}, is less than the penetration resistance of non rotating probe, Q_p , because the rotation reduces axial frictional component. The theoretical relation between Q_{pRot}/ Q_p and period of rotation is shown in Fig. 79 for a 0.58 coefficient of probe-soil friction.

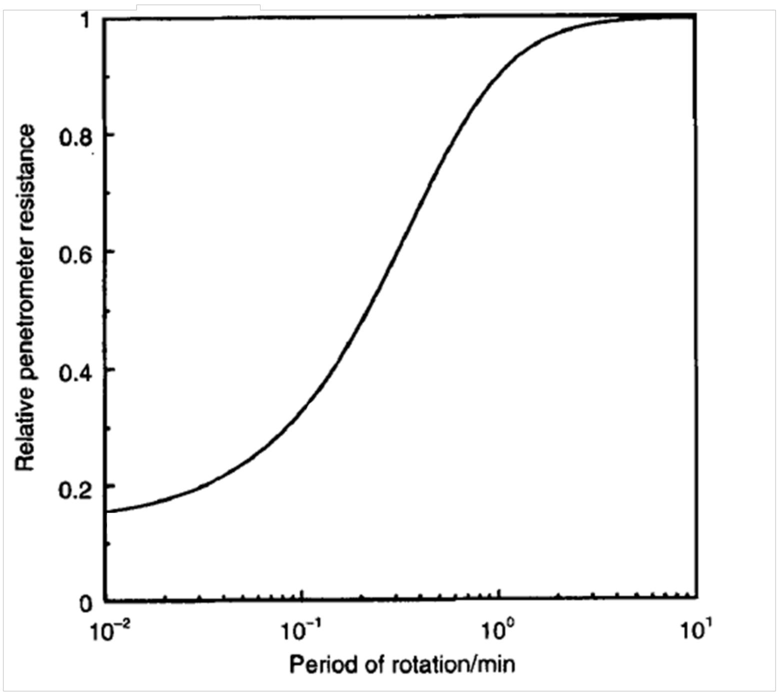

Fig. 79 Predicted relation between penetrometer resistance and period of rotation for a soil-cone friction of 0.58. Adopted from Bengough and Mullins (1997).

The prediction of the reduction of penetration resistance force to *Erodium* seed penetrated vertically was calculated by using the mathematical model of Bengough and Mullins (1997):

$$F_p = \pi R^2 (\sigma(1 + \mu \cdot cot(\alpha)) + c_a \cot(\alpha)) , \tag{5}$$

$$F_{pRot} = \sigma \pi R^2 \sin(\alpha) + \frac{(\mu\sigma + c_a) T^2 v_p{}^2}{2\pi \cdot \sin \cdot (\alpha)} \times \left[\left(\frac{1}{\cos)(\alpha)} + \frac{4\pi^2 R^2}{T^2 v_p{}^2} \right)^{1/2} - \frac{1}{\cos)(\alpha)} \right], \tag{6}$$

where F_p is the magnitude of penetration resistance force to the non-rotating conical probe,
F_{pRot} is the magnitude of penetration resistance force to the rotated conical probe,
R is the radius of conical probe,

α is the cone semiangle of probe,
σ is the stress normal to the metal surface,
c_a is the probe-soil adhesion,
c_a is the probe-soil friction coefficient,
v_p is the speed of penetration,
T is the period of rotation.

The real geometrical parameters of the seed were used for the prediction, R = 0.943 mm and α = 7.32° the same as in previous section. The prediction was performed for two kind of soils: hard soil (σ of 0.1 MPa and c_a of 40 kPa , Bengough et al.1997)) and soft soil (σ of 1 MPa and c_a is negligible, (Bengough et al.1997)). As in the previous case the probe-soil friction coefficient was set to 0.1. Furthermore, v_p and T for the seed were estimated to be 1 mm/min and 2 min. The results showed that the rotation makes the penetration more efficient especially for the soft soil, where the force of penetration resistance was decreased more than two times for rotating seed than for non-rotating seed (Table 18).

Table 18. Magnitude of penetration resistance force of rotated and non-rotated seed with respect to the soil hardness.

	F_p (N)	**F_{pRot} (N)**	**F_{pRot}/F_p**
Hard soil	4.97	3.85	0.77
Soft soil	1.37	0.53	0.39

7 CONCLUDING REMARKS

The *Erodium cicutarium* seed exhibits a very interesting behaviour: it can passively penetrate the substrate thanks to its hygroscopic tail, namely the awn. Understanding its kinematic behaviour on the ground and while it penetrates the soil are important to design and develop innovative robotic solutions for similarly passive soil probing. As initial steps of such a long-term objective, this work studied selected aspects of *Erodium* structure and function, as well as modelling techniques able to describe relevant aspects of the real model (like soil penetration).

In the presented work, main aspects regarding *Erodium* actuation principle, functional importance of the accessory structures, and seed penetration into soil were addressed. The study was mainly performed by video analysis observations, by means of computational modelling and literature search. Some physical models were also built in order to elucidate the characteristics of the awn movement, as dictated by fibre arrangements along the structure, and awn hair compliant movement. In particular, the actuation principle of oblique-strain was described and implemented through FE modelling. Further work should be performed to model the complex winding and unwinding movement of the awn.

The seed leverage was identified as a key feature describing the configuration of seed, right before soil penetration. This configuration was studied taking into account awn tail and awn hair anchorage, awn tail shape, gravity conditions, and body dimensions. It was found that the structure anchored by awn tail is quite stable for all the considered configurations, whereas the anchorage by awn hair can be functional only for the small dimensions comparable with the *Erodium* ones. Furthermore, the results were found to be almost the same for the structures anchored by the tip of straight and curved awn tails. Different gravity conditions were modelled (i.e., Earth, Moon, Mars, and Jupiter). Only for the large length scale structure in Jupiter gravity conditions the seed leverage angle was appreciably affected.

A finite element model of seed penetration was developed, which was able to qualitatively describe the considered penetration task (further experimental data are needed to fully calibrate this modelling approach). The model takes into account the vertical penetration, the seed geometry, and the main soil characteristics. It also elucidated the influence of seed shape on the penetration force. Finally, some theoretical considerations were drawn, regarding the decrease of soil resistance to penetration for rotating seed.

These achievements represent a first step towards a more comprehensive understanding of the *Erodium* model.

For instance, from the present study it emerges that the seed shape (and accessory structures), ground position and unwinding mechanism are important for the penetration. An artificial probe inspired by the *Erodium* could exploit such insight e.g., by adjusting its mass distribution so as to get to the optimal initial pose for penetration. Bioinspiration can then come into play for many aspects, e.g. during soil penetration.

Erodium inspired space probes could represent a new generation of planetary robotic driller to explore different kind of soils, possibly covering large surfaces. Robotic, plant-inspired systems could send fundamental information on the history of the planets/asteroids (while also searching for traces of extra-terrestrial life). The present study takes a preliminary yet effective step along this direction.

REFERENCES

Abaqus, Inc. (2008)."Dassault Systemes. Abaqus Theory Manual".

Abraham, Y., et al. (2012). "Tilted cellulose arrangement as a novel mechanism for hygroscopic coiling in the stork's bill awn," Journal of The Royal Society Interface, vol. 9, pp. 640-647.

Aharoni, H., et al., (2012). "Emergence of Spontaneous Twist and Curvature in Non-Euclidean Rods: Application to Erodium Plant Cells," Physical Review Letters, vol. 108, p. 238106.

Baltodano, G. R., and W. J. Likos, (2006). "Tensile Strength, shear strength and effective stress for unsateurated sand.," PhD thesis 2006.

Baluška F., S. Mancuso, D. Volkmann (2006), Communication in Plants – Springer Verlag Berlin Heidelberg, issue 1.1.

Bengough, A., et al., (1997)."Estimating soil frictional resistance to metal probes and its relevance to the penetration of soil by roots," European journal of soil science, vol. 48, pp. 603-612.

Binder, A. B., R. E. Arvidson, E. A. Guinness, K. L. Jones, E. C. Morris, T. A. Mutch, D. C. Pieri, and C. Sagan, (1977) The geology of the Viking Lander 1 site, J. Geophys. Res., 82, 4439–4451.

Blitz, C., Mimoun, D., Lognonn, P., Komatitsch, D., Tizien, P.G (2006). Tomography of an Asteroid Using a Network of Small Seismometers and an Artificial Impactor. Workshop on Spacecraft Reconnaissance of Asteroid and Comet Interiors. Santa Cruz, CA.

Bombardelli,C. , Michael Broschart, Carlo Menon. (2007). Bio-Inspired Landing and Attachment System for Miniaturised Surface Modules. ARIADNA project IAC-07-A2.8.01. Advanced Concepts Team, European Space Agency, ESTEC, The Netherlands.

Britt et al (2003): Asteroid Density, Porosity, and Structure. Jet Propulsion Laboratory, National Aeronautics and Space Administration. Online source http://hdl.handle.net/2014/38610

Busch S., R. Seidel, O. Speck and T. Speck (2010) Morphological aspects of self-repair of lesions caused by internal growth stresses in stems of Aristolochia macrophylla and Aristolochia ringens. Proc. R. Soc. B 277, 2113–2120 doi:10.1098/rspb.2010.0075.

Cain (2000) M. L. et all. Long-distance seed dispersal in plant population American Journal of Botany 87(9): 1217–1227.

Certini G., R. Scalenghe (2010), “Do soils exist outside Earth?”. Planetary and Space Science 58, 1767–1770.

Chapman C. R. (1978) Asteroid collisions, craters, regolith, and lifetimes. In Asteroids: An Exploration Assessment (D. Morrison and W. C. Wells, eds.), pp. 145–160. NASA Conf. Publ. 2053.

Clark, L.J., Ferraris, S., Price, A.H., Whalley, W.R. (2008), A gradual rather than abrupt increase in soil strength gives better root penetration of strong layers. Plant Soil 307, 235-242.

Eadie L. and Tushar K. Ghosh (2011) Biomimicry in textiles: past, present and potential. An overview - J. R. Soc. Interface (2011) 8, 761–77.

Eberle, A. et al. (2009). "Free Coiling in Tendril-Bearing Plants," Proceedings of Sixth Plant Biomechanics Conference, pp. 67-74.

Elbaum R. et al. (2007) The Role of Wheat Awns in the Seed Dispersal Unit. Science 316, 884.

Evangelista D, Hotton S, Dumais J. (2011), The mechanics of explosive dispersal and self-burial in the seeds of the filaree, Erodium cicutarium (Geraniaceae) The Journal of Experimental Biology 214, 521-529.

Gauss and C. F., (1931)."Untersuchungen über die Eigenschaften der positiven ternären quadratischen Formen von Ludwig August Seber".

Gerbode, S. J., et al. (2012). "How the Cucumber Tendril Coils and Overwinds," Science, vol. 337, pp. 1087-1091.

Gross, K. L. & Werner, P. A. (1982). Colonizing abilities of 'biennial' plant species in relation to ground cover: implications for their distributions in a successional sere. Ecology, 63, 921-931.

Henke, S., H. Hügel, (2007). Räumliche Analysen zur quasi-statischen und dynamischen Penetration von Bauteilen in den Untergrund “," Tagungsband zur, vol. 19, p. 2.13.

Huang W., D. Sheng, S.W. Sloan, H.S. Yu (2004), Finite element analysis of cone penetration in cohesionless soil. Computers and Geotechnics, 31, 517–528.

Janice L. Bishop, Scott L. Murchie, Carle M. Pieters, and Aaron P. Zent (2002) A model for formation of dust, soil, and rock coatings on Mars: Physical and chemical processes on the Martian surface. Journal of Geophysical Research, Vol. 107, No. E11, 5097.

Kiousis, P. D., et al.(2005). "A large strain theory and its application in the analysis of the cone penetration mechanism," International Journal for Numerical and Analytical Methods in Geomechanics, vol. 12, pp. 45-60.

Kirby J. M. and A. G. Bengough (2002), Influence of soil strength on root growth: experiments and analysis using a critical-state model. European Journal of Soil Science, 53, 119–128.

Kleinhans et al.. (2012) Static and dynamic angles of repose in loose granular materials under reduced gravity. J. Geophys. Res., 116, E11004, doi:10.1029/2011JE003865.

Knauth, J.P., Burt, D.M., Wohletz, K.H., 2005. Impact origin of sediments at the Opportunity landing site on Mars. Nature 438, 1123–1128.

Lee, Mark C. (2000) Microgravity Fundamental Physics Program for the New Millennium. Journal of Low Temperature Physics, Vol. 119, Nos. 3/4.

Lienhard J., S Schleiche, S Poppinga, T Masselter, M Milwich, T Speck and J Knippers (2011), Flectofin: a hingeless flapping mechanism inspired by nature. *Bioinspir. Biomim.* **6** 045001 doi:10.1088/1748-3182/6/4/045001.

Lucas JR (1982) The biophysics of pit construction by antlion larvae (Myrmeleon, Neuroptera). Animal Behavior 30:651-664.

M. Oldfield, et al. (2012). "Detailed finite element modelling of deep needle insertions into a soft tissue phantom using a cohesive approach," Computer Methods in Biomechanics and Biomedical Engineering, pp. 1-14.

M. Stolarz (2009) Circumnutation as a visible plant action and reaction. Plant Signaling & Behavior 4:5, 380-387.

Mahutka, K. P., et al. (2006). "Numerical modeling of pile jacking, driving and vibro driving," Proceedings of International Conference on Numerical Simulations of Construction Processes in Geotechnical engineering for Urban Environment pp. 235-246.

Menon, C., Tobias Seidl and Michael Broschart (2007) Biomimetic Approach To Advanced Space Missions. From "Missions to the outer solar system and beyond" the 5th IAA Symposium on Realistic Near-Term Advanced Space Missions.

Mensing S., R. Byrne (1998) Pre-mission invasion of *Erodium cicutarium* in California. Journal of Biogeography Vol. No.v. 25(4) p. 757-762.

Misra, S., et al. (2008). "Needle-tissue interaction forces for bevel-tip steerable needles," in Biomedical Robotics and Biomechatronics,. BioRob 2008. 2nd IEEE RAS & EMBS International Conference on, 2008, pp. 224-231.

Murchie, S., L. Kirkland, S. Erard, J. Mustard, and M. Robinson (2000) Nearinfrared spectral variations of Martian surface materials from ISM imaging spectrometer data. Icarus, 147, 444–471.

Nancy E. S. and Jeffrey R. Lucas (1983). Ecological correlates of explosive seed dispersal. Oecologia, Vol. 59, No. 2/3, pp. 272-278.

Pandolfi, Camilla, Dario Izzo (*not published*) Biomimetics on seed dispersal: survey and insights for space exploration.

S. Mancuso, S. Mugnai, P. Dario, C. Laschi, B. Mazzolai et. Al .(2008) Bio-inspiration from Plants' Roots. Ariadna final project ID: 06/6301. Available on the ACT website.

Sawa, Y., et al. (2011). "Shape selection of twist-nematic-elastomer ribbons," Proceedings of the National Academy of Sciences, vol. 108, pp. 6364-6368,.

Schmitt, O. 1969 Some interesting and useful biomimetic transforms. Proc. 3rd Int. Biophysics Congress, Boston, MA, 1969, p. 297. Paris, France: IUPAB.

Seiferlin, K., Pascale Ehrenfreund, James Garry, Kurt Gunderson, E. Hutter, Gunter Kargl, Alessandro Maturilli, Jonathan Peter Merrison (2008) Simulating Martian regolith in the laboratory. Planetary and Space Science 56, 2009–2025.

Sheeres, D.J. (2003). Asteroid Surface Science with Pods. In Proceedings of the XXXIV Lunar and Planetary Science Conference March 2003, Houston, Texas.

Southard, L., Hoeg, T., Palmer, D., Antol, J., Kolacinski, R., Quinn, R. (2007). Exploring mars using a group of tumbleweed rovers. In: 2007 IEEE International Conference on Robotics and Automation, pp. 775–780.

Squyres S. W., et al. (2004), The Spirit Rover's Athena Science Investigation at Gusev Crater,Mars Science 305, 794.

Stamp N. E., (1989) Seed dispersal of four sympatric grassland annual species of Erodium. Journal of Ecology, Vol. 77, No. 4.

Stamp. N. E (1984), Self-burial behaviour of erodium cicutarium seeds. Journal of Ecology 72, 611-620.

Swaine MD, Dakubu T, Beer T (1979) On the theory of explosively dispersed seeds: a correction. New Phytol 82:777-781.

Tekeste M. Z., R. L. Raper, E. W. Tollner, T. R. Way (2007), Finite Element Analysis of cone penetration in soil for prediction of hardpan location. American Society of Agricultural and Biological Engineers, 50(1), 23−31.

Teresi, L. and V. Varano (2012)., "Ribbon Formation in Twist Nematic Elastomers." Excerpt from the Proceedings of the 2012 COMSOL Conference in Milan.

Van Den Berg P., De Borst R., Huètink H. (1996), An Eulearean Finite Element Model for penetration in layered soil. International Journal for Numerical and Analytical Methods in Geomechanics. 20, 865-886.

Van den Berg, P., et al. (1996). "An Eulerean finite element model for penetration in layered soil," International Journal for Numerical and Analytical Methods in Geomechanics, vol. 20, pp. 865-886.

Vesic, A. S. (1972). "Expansion of cavities in infinite soil mass," Journal of Soil Mechanics & Foundations Div, vol. 98,.

Vincent J. F. V., Bogatyreva, O. A., Bogatyrev, N. R.,Bowyer, A. & Pahl, A. K. (2006) Biomimetics: its practice and theory. J. R. Soc. Interface 3, 471–482. (doi:10.1098/rsif.2006.0127).

Ylikorpi T., A. Halme, P. Jakubik, J. Suomela, M. Vainio (2004) Bio-inspiration from Plants' Roots. In Proceedings of the 8th ESA Workshop on Advanced Space Technologies for Robotics and Automation.

Ylikorpi, Tomi (1994) Preliminary Design of an Automated Lunar Soil Sampler, Master's Thesis, Helsinki University of Technology.

Zeide (1976). Dispersal patterns in Erodium hirtum Willd. Israel Journal of Botany, 25, 221-224.

Sitoghraphy

Randy Korotev, Washington Univ.
http://blogs.airspacemag.com/moon/2012/10/once-in-a-blue-moon/
Dr. Ron Schott, Intro to Geology. Geology Fort Hays State University - Geosciences Dept.:
http://hays.outcrop.org/images/mass_wasting/press4e/figure-12-01a.jpg
J. Rodrigez, http://es.treknature.com/gallery/Europe/Spain/photo53405.htm